

ABSTRACT

Enhanced Geothermal Systems (EGS) are potential clean and reliable energy sources for the future. EGS can be operated constantly and is globally abundant. EGS involves mining heat from hot basement rock in the Earth's crust by circulating water through a hot hydraulically stimulated fractured reservoir. With the geothermal industry growing rapidly in Australia, the author developed an analytical model for EGS in the period December 2007 to February 2008 on behalf of the Petroleum and Geothermal Group of Primary Industries and Resources South Australia (PIRSA). This study presents a continuation of that development. Fracture flow was considered as flow between parallel planes and flow geometry was approximated by assuming areas of radial and linear flow in series. The model eliminated discontinuities which were inherent in the original version of the model and also incorporated inertial effects into the radial flow equation. Effective permeability and skin factors were derived to make the model analogous to petroleum literature. A two-phase well model was implemented to estimate temperature and pressure changes during flow. The model was used to analyse data from the Hijiori EGS long-term circulation test (LTCT), which involved a two layered reservoir consisting of four wells: HDR-1, SKG-2, HDR-2 and HDR-3. The analysis was performed using Microsoft Excel®. The model produced well profiles in temperature, pressure and steam quality. Pressure was found to change linearly except where density changes occurred whilst temperature gradients were parabolic. The model predicted the presence of two-phase flow regimes in the upper sections of the production wells with steam quality values ranging from 0 to 14%. Wellhead pressures determined within a set tolerance of 0.5MPa and differed from literature values by between 0.17 and 43.75%. Wellhead temperatures determined by the model showed large discrepancies from literature values in the range of 20.08 and 83.33%. These discrepancies were due to an invalid assumption which did not account for thermal breakthrough that occurred at Hijiori. Model determined values of reservoir permeability also showed large differences to literature. However the comparison was not direct and the assumption of evenly distributed flow within the reservoir was not valid. Reservoir characteristics of flow impedance and permeability that were estimated by the model were in agreement with literature in that they predicted the easiest flow path in the reservoir to be between HDR-1 and HDR-2. Skin factors determined by the model were not relevant for comparative purposes but were useful in understanding the impact of inertial effects in radial flow. The overall performance of the model was seen as encouraging but further development is required. It was recommended the model be implemented into a more powerful code such as MATLAB® and that an alternative method be used in applying it.

Table of Contents

ABSTRACT.....	i
List of Figures	iii
1 INTRODUCTION.....	1
1.1 PROJECT AIMS.....	1
1.2 PROJECT BACKGROUND.....	1
2 MODEL DESCRIPTION.....	5
2.1 RESERVOIR FLOW.....	5
2.2 WELL FLOW.....	13
3 CASE STUDY – HIJIORI, JAPAN: LONG TERM CIRCULATION TEST 2000 – 2002.....	24
3.1 HISTORY	24
3.2 RELEVANT INFORMATION.....	24
3.3 MODEL ANALYSIS.....	28
4 RESULTS	30
4.1 WELL PROFILES	30
4.2 COMPARISON TO LITERATURE.....	39
4.3 RESERVOIR CHARACTERISTICS	42
5 DISCUSSION.....	44
5.1 WELL PROFILES	44
5.2 COMPARISON TO LITERATURE.....	46
5.3 RESERVOIR CHARACTERISTICS.....	48
5.4 OVERALL PERFORMANCE OF THE MODEL AND RECOMMENDATIONS.....	49
6 CONCLUSIONS.....	51
7 NOMENCLATURE.....	52
8 REFERENCES.....	54
9 APPENDICES	56
9.1 DATA FROM HIJIORI LTCT (TENMA ET AL 2008)	56
9.2 CASING PROFILES	58
9.3 RESERVOIR MODEL DATA FOR LTCT	62
9.4 MODEL DETERMINED WELL PROFILE DATA.....	72
9.5 SAMPLE CALCULATION	78

List of Figures

Figure 1 Schematic of a three well EGS.	2
Figure 2 Micro-seismic even locations during hydraulic stimulation of the Fenton Hill EGS reservoir (Tester et al 2006).	3
Figure 3 Schematic of original model geometry (Cibich et al 2008).	4
Figure 4 Side view of a fracture showing the relationship between aperture and roughness.	5
Figure 5 Dimensionless pressure difference relative to the edge of the plate versus dimensionless radius (Jackson and Symmons 1965).	7
Figure 6 Flow regime described by Darcy's law.	8
Figure 7 Idealised fracture geometry with streamlines for source/sink flow.	10
Figure 8 Approximation of flow geometry with rectangles and circle wedges.	11
Figure 9 Approximation of flow geometry for a quadrant of a five-spot well arrangement.	12
Figure 10 Two-phase flow regimes depicted pictorially (Orkiszewski 1967).	15
Figure 11 Well and formation temperature profile.	22
Figure 12 Illustration of the Hijiori EGS (Tenma et al 2008).	25
Figure 13 Temperature gradient of the formation at Hijiori (Morita et al 2005).	26
Figure 14 Block flow diagram of procedure used to analyse data from the Hijiori LTCT.	29
Figure 15 Model determined pressure and temperature profiles for HDR-1 during run segment 1 of the Hijiori LTCT.	30
Figure 16 Model determined pressure and temperature profiles for HDR-2 during run segment 1 of the Hijiori LTCT.	30
Figure 17 Model determined steam quality profile for HDR-2 during run segment 1 of the Hijiori LTCT.	31
Figure 18 Model determined pressure and temperature profiles for HDR-3 during run segment 1 of the Hijiori LTCT.	31
Figure 19 Model determined steam quality profile for HDR-3 during run segment 1 of the Hijiori LTCT.	32
Figure 20 Model determined pressure and temperature profiles for HDR-1 during run segment 5 of the Hijiori LTCT.	33
Figure 21 Model determined pressure and temperature profiles for SKG-2 during run segment 5 of the Hijiori LTCT.	33
Figure 22 Model determined pressure and temperature profiles for HDR-2 during run segment 5 of the Hijiori LTCT.	34
Figure 23 Model determined steam quality profile for HDR-2 during run segment 5 of the Hijiori LTCT.	34
Figure 24 Model determined pressure and temperature profiles for HDR-3 during run segment 5 of the Hijiori LTCT.	35
Figure 25 Model determined steam quality profile for HDR-3 during run segment 5 of the Hijiori LTCT.	35
Figure 26 Model determined pressure and temperature profiles for HDR-1 during run segment 7 of the Hijiori LTCT.	36
Figure 27 Model determined pressure and temperature profiles for SKG-2 during run segment 7 of the Hijiori LTCT.	36
Figure 28 Model determined pressure and temperature profiles for HDR-2 during run segment 7 of the Hijiori LTCT.	37
Figure 29 Model determined steam quality profile for HDR-2 during run segment 7 of the Hijiori LTCT.	37

Figure 30 Model determined pressure and temperature profiles for HDR-3 during run segment 7 of the Hijiori LTCT.....	38
Figure 31 Model determined steam quality profile for HDR-3 during run segment 7 of the Hijiori LTCT.	38
Figure 32 Comparison of model predicted and literature values of wellhead pressure for HDR-2.	39
Figure 33 Comparison of model predicted and literature values of wellhead pressure for HDR-3.	39
Figure 34 Comparison of model predicted and literature values of wellhead temperature for HDR-2.	40
Figure 35 Comparison of model predicted and literature values of wellhead temperature for HDR-3.	40
Figure 36 Comparison of model predicted and literature values of average permeability for the different reservoir sections.....	41
Figure 37 Model determined flow impedance values for the Hijiori LTCT.....	42
Figure 38 Model determined fracture permeability values for the Hijiori LTCT.	42
Figure 39 Model determined absolute skin factor values for the Hijiori LTCT.....	43
Figure 40 Mass flow rate data for each well during the Hijiori LTCT (Tenma et al 2008).	56
Figure 41 Average wellhead pressure data for each well during the Hijiori LTCT (Tenma et al 2008).	56
Figure 42 Average wellhead temperature data for each well during the Hijiori LTCT (Tenma et al 2008).....	57
Figure 43 Schematic used to describe the reservoir model developed by Tenma et al (2008) for their Hijiori model FEHM.	57
Figure 44 Casing profile for HDR-1 provided by Norio Tenma.	58
Figure 45 Casing profile for SKG-2 provided by Norio Tenma.	59
Figure 46 Casing profile for HDR-2a provided by Norio Tenma.	60
Figure 47 Casing profile for HDR-3 provided by Norio Tenma.	61
Figure 48 Assumed fracture dimensions.	78

1 INTRODUCTION

1.1 PROJECT AIMS

The aims of this research project were:

1. To continue work previously undertaken by the author during December 2007 – February 2008 with Primary Industries and Resources South Australia (PIRSA) on the development of an analytical model for Enhanced Geothermal Systems (EGS). The purposes of developing the model were:
 - a. To provide a basic understanding of pressure and temperature modelling in EGS; and
 - b. To gauge reservoir characteristics of EGS.
2. To apply the model by analysing the Hijiori EGS long-term circulation test (LTCT) and to produce:
 - a. Well profiles in temperature, pressure and steam quality;
 - b. Estimations of production wellhead temperature and pressure; and
 - c. Estimations of reservoir flow impedance, permeability and skin factors.
3. To compare the results of the analysis with Hijiori field data from literature.

1.2 PROJECT BACKGROUND

With issues of climate change and limited fossil fuel resources affecting global and local energy markets, Enhanced Geothermal Systems (EGS) present a reliable and zero emissions energy alternative for the future. Unlike other sources of environmentally conscious energy such as solar and wind, EGS can be operated 24/7 and has minimal environmental footprint. Research and development of EGS is proceeding rapidly, particularly in Australia with the first industry driven Australian Geothermal Energy Conference being held in August 2008. Expenditure on EGS projects in Australia is forecasted to reach in excess of AUD\$800 million by the year 2013 and the number of Geothermal Licences issued had reached fifty by the year 2007 (Goldstein et al 2008). The potential for EGS worldwide is enormous with 100million EJ (1×10^{27} J) of stored thermal energy in the Earth's crust at accessible depths of 6 – 10km anywhere in the world (Tester 2008).

EGS, formally referred to as Hot Dry Rocks or HDR, works by circulating water through a hot fractured reservoir (or fracture zone) between injection and production wells, thus acting as an underground heat exchanger as shown in figure 1. The high temperature water produced can be used to generate electricity either by directly passing it through a turbine, or by putting it through a heat exchanger as part of a binary system. After the heat is extracted the water is reinjected into the fractured reservoir by pumping back down the injection well. EGS

reservoirs need to be created by hydraulic stimulation of hot impermeable granite rocks usually around 3 – 10km below the surface. Hydraulic stimulation is the process of causing micro-seismic events by injection of extremely high pressure fluid into the bed rock causing natural fractures to prop open, thus increasing the permeability and productivity of the reservoir. The practice is frequently used by the petroleum industry in enhancing oil recovery. An image of the micro-seismic events that occurred at the original EGS project at Fenton Hill, New Mexico in the United States is shown in figure 2.

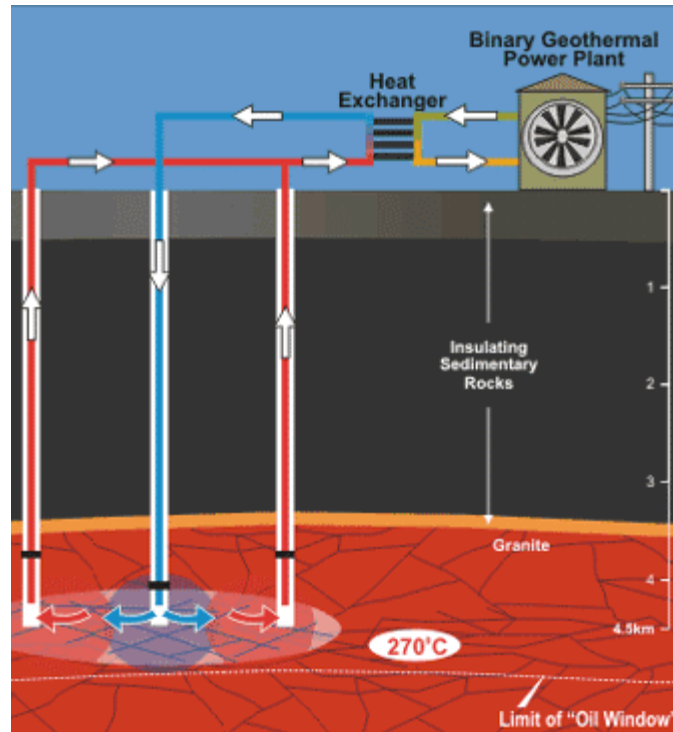


Figure 1 Schematic of a three well EGS.

An industrial scale EGS power plant is yet to be commissioned and the technology has not been fully developed. However constant improvements to EGS development have put the industry in good stead. Currently Australia's leading geothermal energy company Geodynamics Ltd is in the process of commissioning a 1MW pilot power plant at the Cooper Basin in North East South Australia, and plans to extend power production to 50MW by 2012 (Grove-White 2008).

With the geothermal energy industry in its embryonic stage the author, on behalf of state regulators the Petroleum and Geothermal Group of PIRSA, developed an analytical EGS steady-state pressure flow model during the period December 2007 to 2008. Whilst many numerical simulators were available at the time, it was desired that the model be developed in-house and that it be analytical so that the fundamental mathematics of

EGS modelling could be easily understood. During the three month development period the model was put through a sensitivity analysis. The analysis was to determine the effect of certain model parameters on reservoir pressure drop and wellhead pressures. The results of the analysis showed that due to thermal syphoning or buoyancy effects, an EGS with sufficient reservoir permeability could be run as a naturally convective system, that is, the EGS would self pump. It also found that fracture aperture is perhaps the most important factor of an EGS reservoir. This result was logical as fracture aperture determines the extent of reservoir permeability (Cibich et al 2008). PIRSA has since used the model as a tool to provide pressure estimates in its evaluation of the technical feasibility of EGS in South Australia.

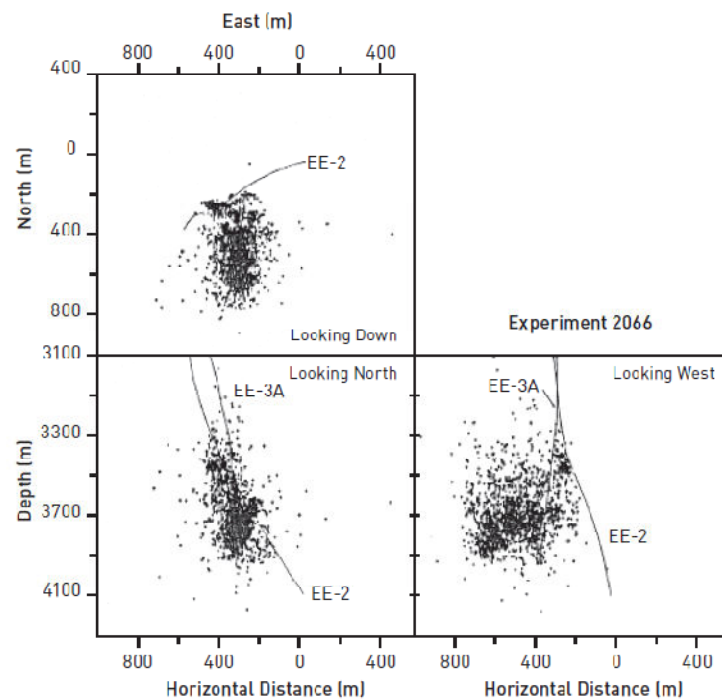


Figure 2 Micro-seismic event locations during hydraulic stimulation of the Fenton Hill EGS reservoir (Tester et al 2006).

The original version of the model, based predominately on literature, was simplistic but a good basis for further sophistication and refinement. The current study, as stated in the project aims, sought to continue in the development of the analytical model. The model, as a result of this study, has been improved by correcting issues associated with the original and by incorporating new features. Table I below summarises the changes and additions to the original model. This study has been based on the same premise as the original and like the original its purpose was to describe water flow in EGS from injection wellhead to production wellhead (figure 3). A full description of the current version of the model is given in section 2.

Table I Changes to the original model now part of the current version.

Issues with original model	Corrections/additional features of current model
Undefined flow regions meant discontinuities existed in the fracture model.	Area correction factor has been incorporated to compensate for undefined flow areas.
Well flow was assumed isothermal which was not valid.	The well flow model now accounts for two phase flow as well as temperature and pressure changes along the well.
Radial flow equation did not account for inertial effects around the wellbore.	The model now accounts for inertial effects into the radial flow equation and incorporates it as a skin factor, making it analogous to petroleum literature.
	Model now has an effective permeability term for fracture flow and is able to calculate total reservoir permeability.
	Model can now be used to analyse and be compared to field data.

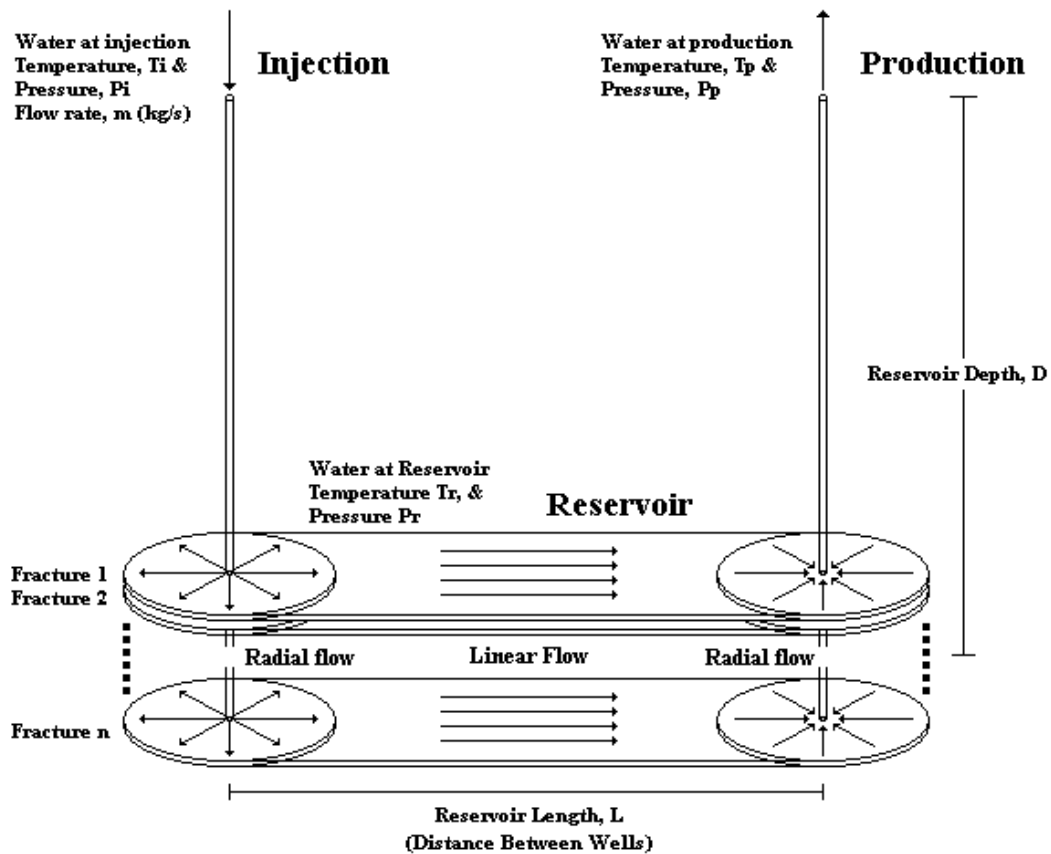


Figure 3 Schematic of original model geometry (Cibich et al 2008). The current version has been developed for based on the same ideal EGS flow.

The remainder of the report is as follows. Section 3 gives an account of the Hijiori EGS project which was analysed using the model. Section 4 presents the results of the Hijiori analysis. These results are evaluated and discussed in section 5 and final conclusions are presented in section 6.

2 MODEL DESCRIPTION

2.1 RESERVOIR FLOW

Linear Pressure Drop in a Fracture

The model attempts to represent flow through hydraulically fractured non-porous rock. That is, flow is only through fractures and not through the medium itself. Fracture flow is usually described as steady laminar flow between parallel plates (Jones, Wooten and Kaluza 1988). Linear flow pressure drop between smooth parallel plates is modelled by the cubic law equation

$$\Delta P = \frac{12\mu Lq}{h^3 w}$$

Equation 1 Cubic law equation

Where ΔP is pressure drop, μ is fluid dynamic viscosity, L is length of flow, q is volumetric flow rate, h is aperture and w is width. However fractures are not smooth and experiments of fracture flow show deviation from the cubic law due to roughness creating friction (Jones et al 1988). Fracture roughness is shown in figure 4.

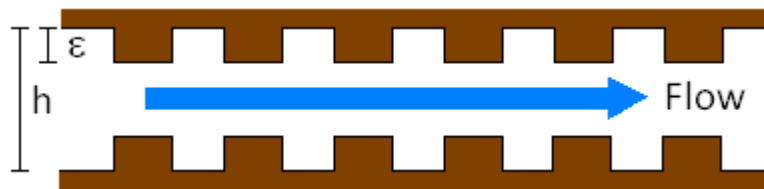


Figure 4 Side view of a fracture showing the relationship between aperture and roughness.

Louis (1969) developed an empirical relationship to quantify friction. It has been modified in this study to the form of

$$f_l = 1 + 3.1 \left(\frac{\varepsilon}{h} \right)^{1.5}$$

Equation 2 Modified Louis (1969) friction factor

Thus equation 1 becomes

$$\Delta P_{lin} = f_l \frac{12\mu Lq}{h^3 w}$$

Equation 3 Pressure drop in linear flow

The model assumes that flow within a fracture is laminar. The Reynolds number criteria for linear flow is given as

$$Re_{lin} = \frac{2h\rho u_{lin}}{\mu} \leq 2300$$

Equation 4 Reynolds number criteria for linear flow

Hence the model will not be able to provide solutions if equation 4 is not true, that is, turbulent flow would be expected.

Radial Pressure drop in a Fracture

The model uses a similar equation to describe radially converging laminar flow occurring around wellbores of an EGS reservoir. Murphy, Coxon and McEligot (1979) compared analytical models of radial flow and found that the expression derived by Livesey (1960) correlated best to numerical solutions of the governing equations with a maximum error of 20% at small radii. Livesey's expression assumes a parabolic velocity profile at all radii and has been modified for this model to incorporate the Louis friction factor

$$\Delta P_{rad,p} = f_l \frac{12\mu q \ln(r_{ep}/r_w)}{h^3 \theta} + \frac{3q^2 \rho}{5\theta^2 h^2} \left[\frac{1}{r_w^2} - \frac{1}{r_{ep}^2} \right]$$

Equation 5 Pressure drop for inward radial flow

The first term of equation 5 gives pressure drop due to viscous effects and thus takes similar form as equation 3 whilst the second term is pressure drop due to inertia effects as a result of acceleration in the radial direction. Equation 5 is a combination of the limiting solutions to the governing Navier-Stokes equations (Murphy et al 1979).

For radially diverging laminar flow Livesey showed that the sign of the inertial pressure drop term is negative and that at moderate velocities, inertia effects may be more significant than viscous effects. Thus it is possible for negative pressure drop to occur in the divergent radial flow region; that is, pressure can rise in the direction of flow. This phenomenon known as suction generating attraction or the Bernoulli Effect has been confirmed in other studies including Jackson and Symmons (1965) and Paivanas and Hassan (1981). In the study by Jackson and Symmons they showed experimentally that for laminar incompressible air flow, pressure at small radii increased due to dominant inertia effects. This is shown in figure 5 below which demonstrates that dimensionless pressure increased and then reached a maximum. This maximum is where viscous effects and

inertia effects were equal; the decline in pressure after the maximum is where viscous effects began to dominate.

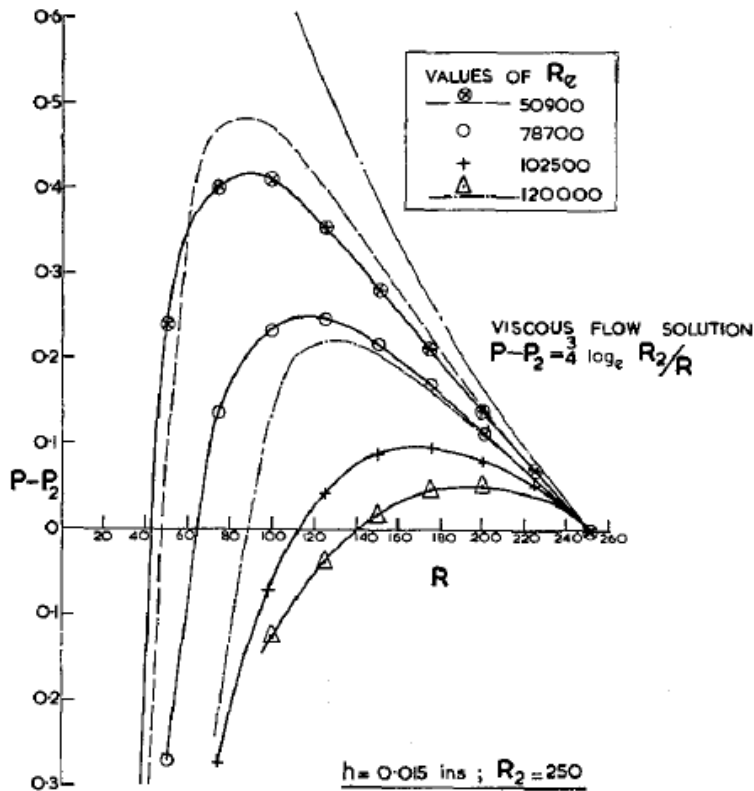


Figure 5 Dimensionless pressure difference relative to the edge of the plate versus dimensionless radius (Jackson and Symmons 1965).

Diverging radial flow is therefore modelled by equation 6

$$\Delta P_{rad,i} = f_l \frac{12\mu q \ln(r_{ei}/r_w)}{h^3 \theta} - \frac{3q^2 \rho}{5\theta^2 h^2} \left[\frac{1}{r_w^2} - \frac{1}{r_{ei}^2} \right]$$

Equation 6 Pressure drop for outward radial flow

The Reynolds criteria for radial flow is given by the Overall Reynolds number as given in (Murphy et al 1979)

$$Re_o = \frac{q\rho}{\theta h\mu} \leq 1.0 \times 10^8$$

Equation 7 Overall Reynolds number criteria for radial flow

That is, radial flow is assumed laminar when overall Reynolds is less than or equal to 1.0×10^8 . The overall Reynolds number is based on an acceleration parameter which determines if an accelerated turbulent boundary layer will revert to laminar. Thus if the criteria given by equation 7 above holds then flow will be expected to

remain laminar despite local Reynolds numbers being large. Again the model will only provide a solution if flow is laminar.

Effective Permeability and Skin Factor

The model incorporates an effective permeability term k_e for a fractured reservoir. Permeability is a term applying usually to sedimentary reservoirs where fluid flows through porous rock. However it may also be applied to fractures by an effective permeability term that can be derived by comparing the fracture flow equations to Darcy's law for flow through porous medium. The linear flow scenario for Darcy's law (equation 8) is shown in figure 6

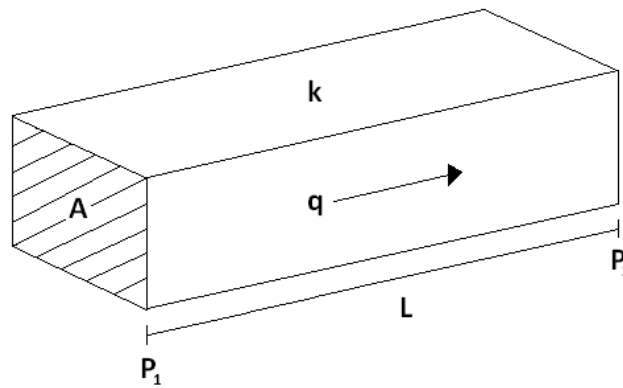


Figure 6 Flow regime described by Darcy's law.

$$\Delta P_{lin} = \frac{qL\mu}{kA}$$

Equation 8 Darcy's law for linear flow through porous medium

Now equating equation 3 for a single fracture and Darcy's law

$$f_l \frac{12\mu Lq}{h^3 w} = \frac{qL\mu}{kA}$$

Cancelling terms, substituting $A = wh$, which is the cross-sectional area of a fracture, then rearranging for k yields

$$k_e = \frac{h^2}{12f_l}$$

Equation 9 Effective permeability for a single fracture

Therefore linear pressure drop for a single fracture can be expressed as

$$\Delta P_{lin} = \frac{qL\mu}{k_e h w}$$

Equation 10 Linear flow pressure drop with effective permeability term

Radial flow equations in petroleum literature incorporate a skin factor S , which accounts for pressure drop caused by damaged or enhanced permeability around the wellbore (Slider 1983)

$$\Delta P_{rad} = \frac{\mu q [\ln(r_e/r_w) + S]}{k 2\pi h}$$

Equation 11 Darcy's radial flow equation with skin factor

Therefore equation 5 must be rearranged to the form of equation 11. This can be done in a few steps

$$\Delta P_{rad,p} = f_l \frac{12\mu q \ln(r_{ep}/r_w)}{h^3 \theta} + \frac{3q^2 \rho}{5\theta^2 h^2} \left[\frac{1}{r_w^2} - \frac{1}{r_{ep}^2} \right]$$

$$\Delta P_{rad,p} = f_l \frac{12\mu q}{h^3 \theta} \left(\ln(r_{ep}/r_{wp}) + \frac{q\phi h}{20f_l \mu \theta} \left[\frac{1}{r_{wp}^2} - \frac{1}{r_{ep}^2} \right] \right)$$

$$\Delta P_{rad,p} = f_l \frac{12\mu q [\ln(r_{ep}/r_{wp}) + S]}{h^3 \theta}$$

Where for converging radial flow

$$S = \frac{q\phi h}{20f_l \mu \theta} \left[\frac{1}{r_{wp}^2} - \frac{1}{r_{ep}^2} \right] = \frac{\Delta P_{inertia}}{(12f_l q \mu / h^3 \theta)}$$

And for diverging radial flow

$$S = -\frac{q\phi h}{20f_l \mu \theta} \left[\frac{1}{r_{wi}^2} - \frac{1}{r_{ei}^2} \right] = \frac{\Delta P_{inertia}}{(12f_l q \mu / h^3 \theta)}$$

Now equating the rearranged radial flow equation and equation 11, cancelling terms and solving for k

$$f_l \frac{12\mu q [\ln(r_e/r_w) + S]}{h^3 \theta} = \frac{\mu q [\ln(r_e/r_w) + S]}{k \theta h}$$

$$k_e = \frac{h^2}{12f_l}$$

Therefore permeability in the radial section is the same as in the linear section and radial pressure drop can be given by

$$\Delta P_{rad} = \frac{\mu q [\ln(r_e/r_w) + S]}{k_e \theta h}$$

Equation 12 Radial flow pressure drop with effective permeability term

Once pressure drop is determined the total permeability of the reservoir can be approximated by Darcy's law. Consider a fracture zone of width w and vertical length H . The cross section area of that flow area is therefore $A = wH$. Rearrangement of Darcy's law yields

$$k_{etotal} = \frac{qL\mu}{\Delta PwH}$$

Equation 13 Total reservoir permeability.

Approximating Fracture Flow Geometry

Using the defined equations for linear and radial pressure drop, the model approximates reservoir geometry by combining circles and rectangles; that is, areas of radial and linear flow in series. Consider the situation in figure 7. It shows a plan view of idealised fracture geometry with injection and production wells and typical flow streamlines for source/sink flow.

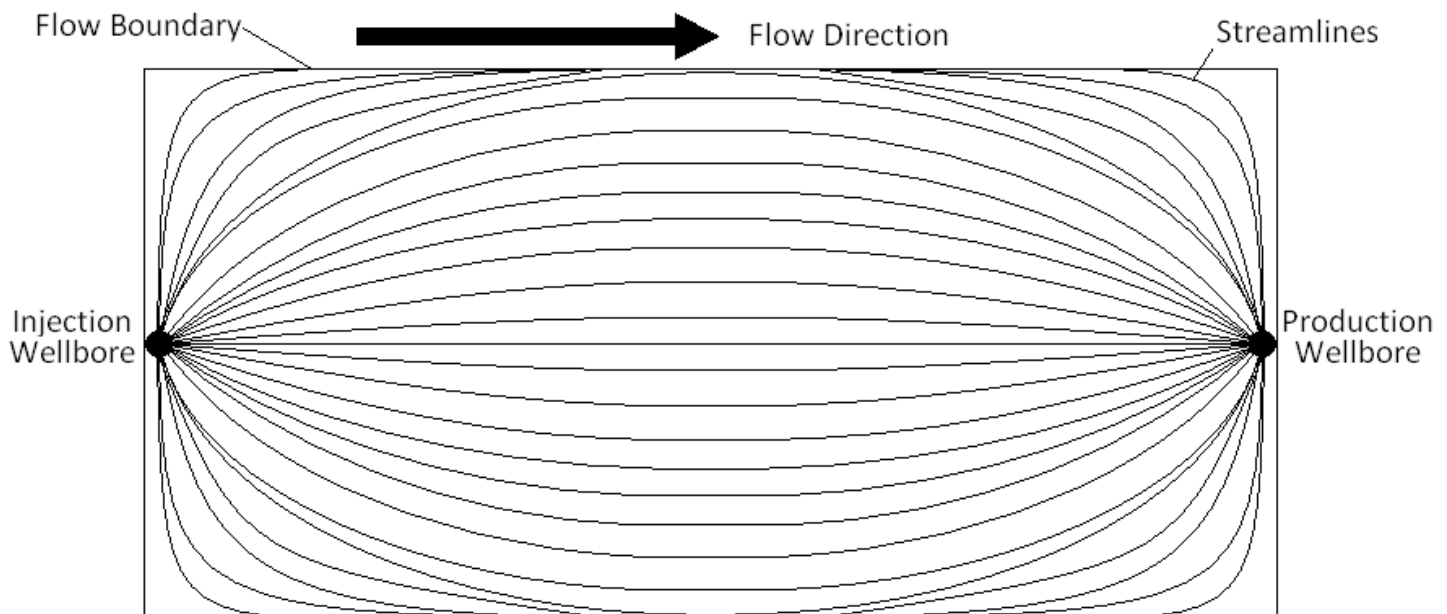


Figure 7 Idealised fracture geometry with streamlines for source/sink flow.

This fracture geometry can be approximated by combining a rectangle with two circle wedges in series as shown in figure 8. In the pink areas flow is undefined as discontinuities exist between the radial and linear regimes. This issue can be overcome by defining correction length δL that creates a pseudo linear flow length to compensate for the area of undefined flow (Slider 1983). In this case

$$\delta L = \frac{1}{2} \left(D - L - \frac{1}{2} \pi r_e \right)$$

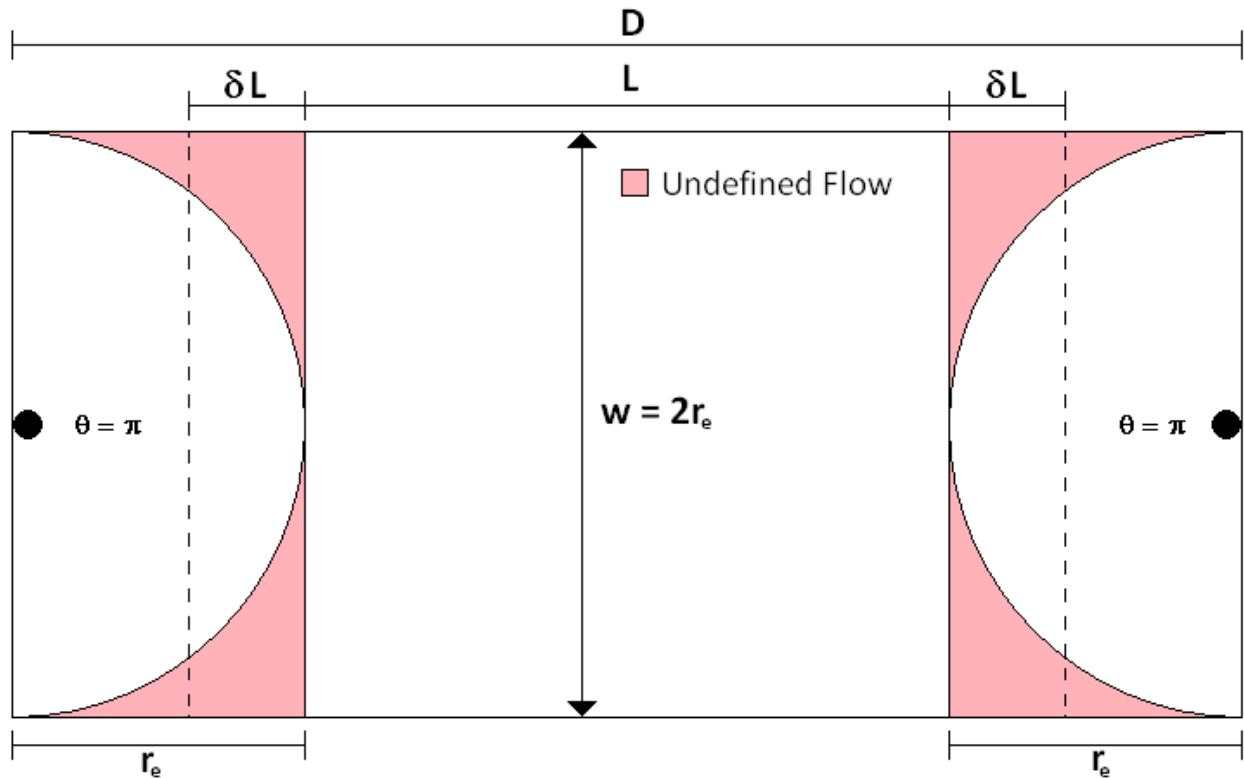


Figure 8 Approximation of flow geometry with rectangles and circle wedges.

This method allows the model to estimate the entire pressure drop of the fracture simply by summing the pressure drops in each section. In this case there is a radial flow section of half a circle at each wellbore and a linear flow section rectangle in between. The total pressure drop is therefore

$$\Delta P_{total} = \frac{\mu q}{k_e h} \left[\frac{2 \ln(r_e/r_w)}{\theta} + \frac{(2\delta L + L)}{w} \right]$$

Where θ is the angle of radial flow, which in this case is equal to π radians. It can be seen that the above expression does not contain any inertia or skin terms which were described for equation 12. This is due to the

symmetry of the idealised fracture geometry where r_{ep} equals r_{ei} resulting in cancellation of the skin terms. For real fracture flow, geometry is likely to be more complicated and therefore those terms are likely to be present.

Another example of flow geometry approximation is the quadrant of a five-spot well arrangement shown in figure 9. Two-overlapping quarter circles can be used to approximate flow.

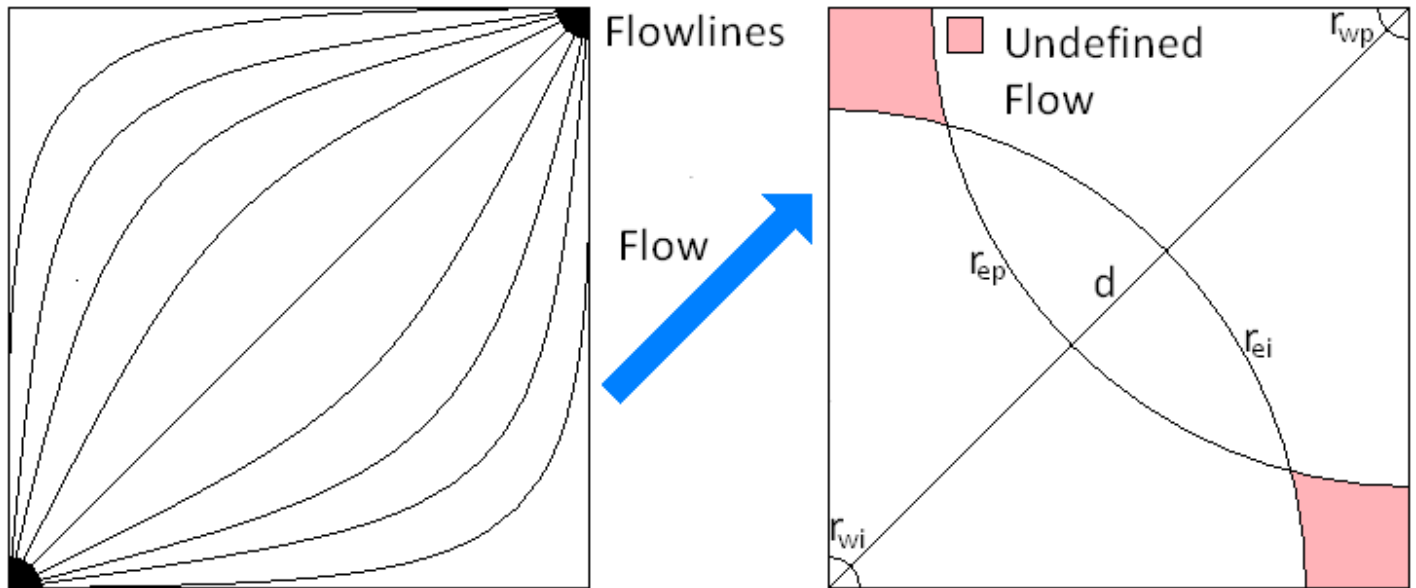


Figure 9 Approximation of flow geometry for a quadrant of a five-spot well arrangement.

Here the area of each radial system should be equal to half the area of the quadrant (Slider 1983). That is

$$1/4 \pi r_{ep}^2 = 1/4 \pi r_{ei}^2 = d^2/4$$

$$r_{ep} = r_{ei} = 0.564d$$

Therefore with θ equal to $\pi/2$ and assuming that r_{wp} equals r_{wi} summation of pressure drop is

$$\Delta P_{total} = \frac{4\mu q \ln(0.564d/r_w)}{k_e h \pi}$$

Again due to symmetry the skin terms of the radial flow equation cancel out and pressure drop is given only by viscous terms.

It should be noted that flow temperature is assumed to be at the same temperature as the reservoir. Therefore fluid properties of density ρ and viscosity μ are determined at reservoir temperature and pressure.

2.2 WELL FLOW

A thorough review of petroleum literature has revealed an appropriate method for determining pressure drop and temperature change in geothermal wells. The model can account for both single and two-phase flow as well as the four regimes of two-phase flow. The model uses flow pressure and temperature to determine certain parameters. However values of temperature and pressure change with flow length. So well flow thus requires discreet modelling by using increments of a certain length depending on the total length of the well. The temperature and pressure values used to determine the parameters of the model are taken from the beginning of the increment.

Pressure Drop Determination

Farouq (1981) devised equations 14 and 15 to determine pressure drop in upward and downward geothermal well flow

$$\Delta P = \left(\frac{\rho_m g - \tau_f}{1 - \gamma_a} \right) \Delta Z$$

Equation 14 Pressure drop for downward flow

$$\Delta P = \left(\frac{\rho_m g + \tau_f}{1 - \gamma_a} \right) \Delta Z$$

Equation 15 Pressure drop for upward flow

Where ρ_m is density of the flow, τ_f is the friction gradient, ΔZ is the length of the increment and γ_a is the acceleration gradient given by

$$\gamma_a = \frac{mq_G}{A^2 P}$$

Equation 16 Acceleration gradient

Mixture density is perhaps the most important parameter as it determines the amount of hydrostatic head in the well, which is the biggest contributor to pressure drop. Values of ρ_m and τ_f are determined differently for each flow regime.

Flow Regime Detection Criteria

There are two types of water flow in geothermal wells: single phase and two-phase. Single phase flow is likely to be liquid phase given the high pressures associated with EGS. Single or liquid phase flow is assumed to occur when the enthalpy of liquid water at flow pressure is greater than the enthalpy of liquid water at flow temperature (Chadha, Malin and Palacio-Perez 1993). That is

$$h_L > h$$

Equation 17 Single phase flow criteria

Liquid enthalpy at temperature (h) and liquid water enthalpy at pressure (h_L) are given by steam tables. If $h_L < h$ then two-phase flow is assumed to occur, where flow is a mixture of liquid and vapour. There are four classes of two-phase flow that can occur in geothermal wells: bubble, slug, transition and mist. These regimes are depicted pictorially in figure 10. The criteria used to determine which two-phase flow regime occurs is given by Duns and Ros (1961) and is as follows

$$L_{b/s} > v_{SG}/v_{ST}$$

Equation 18 Bubble flow criteria

$$L_{b/s} < v_{SG}/v \text{ and } L_{S/t} > N_{GV}$$

Equation 19 Slug flow Criteria

$$L_{S/t} < N_{GV} < L_{t/m}$$

Equation 20 Transition flow criteria

$$L_{t/m} < N_{GV}$$

Equation 21 Mist flow criteria

The bubble/slug, slug/transition and transition/mist boundary terms are given by equations 22, 23 and 24 respectively where d_w is well diameter and v_{SG} and v_{SL} are the superficial velocities of the vapour and liquid phases determined by equations 25 and 26 respectively.

$$L_{b/s} = 1.071 - 0.2218 \frac{v_{ST}^2}{d_w} \geq 0.13$$

Equation 22 Bubble/slug boundary term

$$L_{S/t} = 50 + 36N_{LV}$$

Equation 23 Slug/transition boundary term

$$L_{t/m} = 75 + 84(N_{LV})^{0.75}$$

Equation 24 Transition/mist boundary term

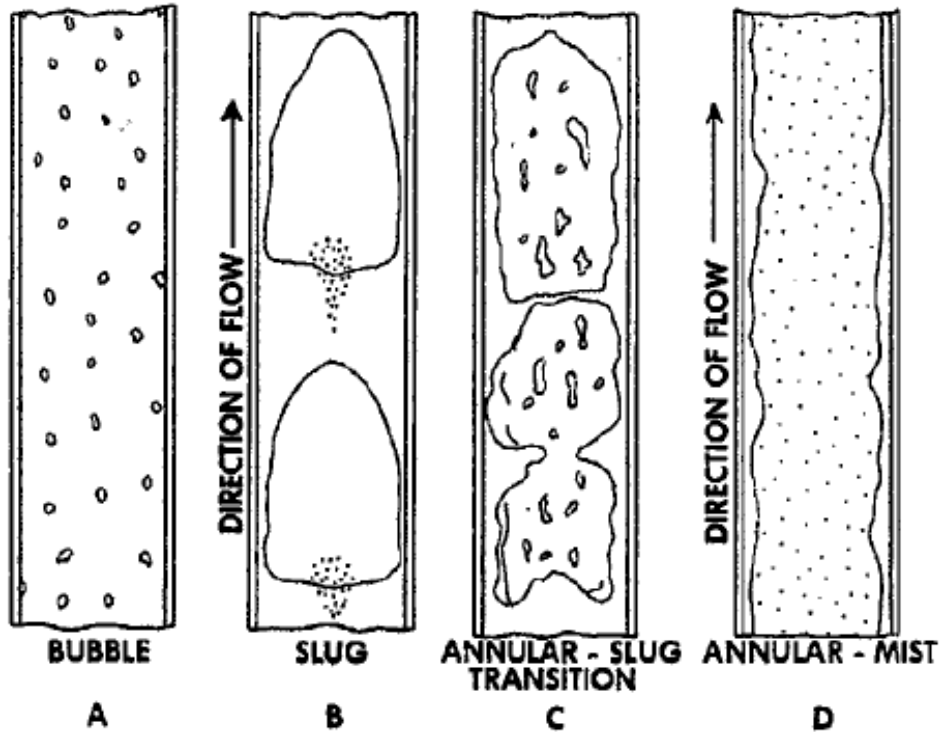


Figure 10 Two-phase flow regimes depicted pictorially (Orkiszewski 1967).

$$v_{SG} = \frac{q_G}{A}$$

Equation 25 Superficial velocity of vapour phase

$$v_{SL} = \frac{q_L}{A}$$

Equation 26 Superficial velocity of liquid phase

Where A is the cross sectional area of the well and the vapour and liquid volumetric flow rates are calculated by equations 27 and 28 respectively

$$q_G = \frac{mx}{\rho_G}$$

Equation 27 Volumetric flow rate of vapour phase

$$q_L = \frac{m(1-x)}{\rho_L}$$

Equation 28 Volumetric flow rate of liquid phase

Where m is mass flow rate and ρ is density. Steam quality or vapour mass fraction is given by

$$x = \frac{h - h_L}{h_G - h_L}$$

Equation 29 Steam quality or vapour mass fraction

And enthalpy of water vapour at pressure is given by steam tables. Total superficial velocity and total volumetric flow rate are given by equations 30 and 31 respectively

$$v_{ST} = v_{SL} + v_{SG}$$

Equation 30 Total superficial velocity

$$q_T = q_L + q_G$$

Equation 31 Total volumetric flow rate

The vapour and liquid velocity numbers in the Duns and Ros criteria are determined by equations 32 and 33 respectively

$$N_{GV} = v_{SG} \left(\frac{\rho_L}{g\omega} \right)^{0.25}$$

Equation 32 Vapour velocity number

$$N_{LV} = v_{SL} \left(\frac{\rho_L}{g\omega} \right)^{0.25}$$

Equation 33 Liquid velocity number

Where g is gravitational acceleration and ω is the surface tension of water which is given by (Spang 1997)

$$\omega = 235.8 \left(1 - \frac{T}{T_c}\right)^{1.256} \left[1 - 0.625 \left(1 - \frac{T}{T_c}\right)\right]$$

Equation 34 Surface tension

Where $T_c = 647.096\text{K}$ is the critical temperature of water.

Single or Liquid Phase Flow

In single phase or liquid only flow, the mixture density is simply given by the density of liquid of water at flow temperature and pressure. The friction gradient for liquid only or single phase flow is determined by

$$\tau_f = \frac{f \rho_L v_{ST}^2}{2d_w}$$

Equation 35 Friction gradient

Where f is the Moody friction factor given by the iterative Colebrook equation which is performed until convergence is achieved (Munson et al 2006)

$$f_{n+1} = \frac{0.25}{\left\{\log_{10}\left[\frac{\varepsilon/d_w}{3.7} + 2.51\left(\frac{Re\sqrt{f_n}}{2300}\right)\right]\right\}^2}$$

Equation 36 Colebrook equation

Bubble Flow

As in the study by Farouq (1981) this study uses the method provided by Gould et al (1974) for determining mixture density for bubble flow

$$\rho_m = \rho_L(1 - \eta_G) + \rho_G \eta_G$$

Equation 37 Mixture density equation for bubble flow

Where η_g is the vapour volume fraction determined by (Chadha, 1993)Griffith and Wallis 1961)

$$\eta_G = 0.5 \left[\left(1 + \frac{v_{ST}}{v_{slip}}\right) - \left\{ \left(1 + \frac{v_{ST}}{v_{slip}}\right)^2 - 4 \frac{v_{SG}}{v_{slip}} \right\}^{1/2} \right]$$

Equation 38 Vapour volume fraction for bubble flow

Where $v_{\text{slip}} = 0.2439\text{m}\cdot\text{s}^{-1}$ is the slip velocity approximated by Orkiszewski (1967) and vapour density is given by (Chadha et al 1993)

$$\rho_G = 0.5809P^{0.9588}$$

Equation 39 Vapour density for bubble flow

Again using the method provided by Gould et al, this model determines friction gradient by

$$\tau_f = \frac{f\rho_m v_{ST}^2}{2d_w}$$

Equation 40 Friction gradient for bubble flow

Slug Flow

Slug flow requires two formulae for determining mixture density; one for the start of the regime when the liquid content is high and observed pressure drop is also higher, and another for later on in the regime when vapor content is in the order of $x > 0.1$ and observed pressure drop is lower (Chadha et al 1993). Chadha et al (1993) present criteria for using the appropriate mixture density formula originally developed by Palacio (1990). Firstly introducing the dimensionless parameter that defines the criteria

$$N_p = \frac{(N_{LV} + N_{GV})}{\eta_G}$$

Equation 41 Dimensionless parameter for slug flow stage determination

Where

$$\eta_G = \frac{q_G}{q_T + Av_b}$$

Equation 42 Vapour volume fraction for slug flow

And v_b the bubble rise velocity developed by Nicklin is given by:

$$v_b = 1.2v_{ST} + 0.35(gd_w)^{0.5}$$

Equation 43 Nicklin bubble rise velocity correlation

The onset stage or first stage of slug flow will occur for $N_p < 50$ and $x < 0.03$ and the mixture density is calculated by:

$$\rho_m = \rho_L(1 - \eta_G) + \rho_G\eta_G$$

Equation 44 Mixture density for first stage slug flow

where densities of liquid and vapour water are determined the same way as in bubble flow. The second stage of slug flow occurs for $N_p \geq 50$ and $x \geq 0.03$ and involves a more complicated calculation procedure. Mixture density is given by

$$\rho_m = \frac{m + \rho_L u_b A}{q_T + u_b A} + \Gamma \rho_L$$

Equation 45 Mixture density for second stage slug flow

where liquid density is calculated in the same manner as in bubble flow and u_b is bubble rise velocity. Bubble rise velocity here is determined in a different manner to before. First the prevailing bubble Reynolds number needs to be determined

$$Re_b = \frac{\rho_L v_b d_w}{\mu_L}$$

Equation 46 Bubble Reynolds number

Where liquid viscosity is determined by the following relation with temperature in degrees Celsius

$$\mu_L = \frac{2.185 \times 10^{-3}}{(0.28921 + 0.07281T + 1.67 \times 10^{-5}T^2)}$$

Equation 47 Water liquid phase viscosity

Then the appropriate u_b calculation needs to be used in order to calculate bubble rise velocity. The criteria for bubble rise velocity calculation is as follows

For $Re_b \leq 3000$

$$u_b = (0.546 + 8.74 \times 10^{-6} Re)(gd_w)^{0.5}$$

Equation 48 Bubble rise velocity for $Re_b \leq 3000$

For $3000 < Re_b < 8000$

$$u_b = 0.5u_{bi} + \left(u_{bi}^2 + \frac{1.11656 \times 10^4 \mu_L}{\rho_L \sqrt{d_w}} \right)^{0.5}$$

Equation 49 Bubble rise velocity for $3000 < Re_b < 8000$

Where $u_{bi} = (0.251 + 8.74 \times 10^{-6} Re)(gd_w)^{0.5}$

For $Re_b \geq 8000$

$$u_b = (0.35 + 8.74 \times 10^{-6} Re)(gd_w)^{0.5}$$

Equation 50 Bubble rise velocity for $Re \geq 8000$

It should be noted that the Reynolds number in equations 48 to 50 are not in fact the bubble Reynolds number given above, rather Re is given by

$$Re = \frac{\rho_L v_{ST} d_w}{\mu_L}$$

Equation 51 Reynolds number used in equations 48 to 50

The other parameter which requires calculation is the liquid distribution coefficient Γ which is also determined by criteria set out by Orkiszewski. For $v_{ST} < 3.048 \text{ m/s}$

$$\Gamma = -0.2132546 v_{ST} - 0.1$$

Equation 52 Liquid distribution coefficient for $v_{ST} < 3.048 \text{ m.s}^{-1}$

And for $v_{ST} \geq 3.048 \text{ m/s}$

$$\Gamma = \frac{(1.7421568 \times 10^{-2} \log_{10}(10^3 \mu_L))}{d_w^{0.799}} - 0.709 - 0.162 \log_{10} v_{ST} - 0.888 \log_{10} d_w - 0.541784$$

Equation 53 Liquid distribution coefficient for $v_{ST} \geq 3.048 \text{ m.s}^{-1}$

The friction gradient for slug flow is taken from Chierici et al (1974) and is

$$\tau_f = (1 - \eta_G) f \rho_L \frac{v_{ST}^2}{2d_w}$$

Equation 54 Friction gradient for both stages of slug flow

Transition Flow

Transition flow is a combination of slug and mist flow. Duns and Ros (1963) developed equations 55 and 56 which incorporate values of mixture density and friction gradient from the slug and mist regimes in order to approximate these parameters for transition flow

$$\rho_m = (\rho_m)_s \frac{L_{t/m} - N_{GV}}{L_{t/m} - L_{S/t}} + (\rho_m)_m \frac{N_{GV} - L_{S/t}}{\frac{L_{t/m}}{m} - \frac{L_{S/t}}{t}}$$

Equation 55 Mixture density for transition flow

$$\tau_f = (\tau_f)_s \frac{L_{t/m} - N_{GV}}{L_{t/m} - L_{S/t}} + (\tau_f)_m \frac{N_{GV} - L_{S/t}}{L_{t/m} - L_{S/t}}$$

Equation 56 Friction gradient for transition flow

Where the subscripts s and m denote slug and mist respectively

Mist Flow

Mist flow mixture density and friction gradient are again provided by Duns and Ros (1963) are given below as equations 57 and 58 respectively.

$$\rho_m = \rho_L \frac{v_{SL}}{v_{ST}} + \rho_G \frac{v_{SG}}{v_{ST}}$$

Equation 57 Mixture density for mist flow

$$\tau_f = \frac{f \rho_G v_{SG}^2}{2d_w}$$

Equation 58 Friction gradient for mist flow

Heat Transfer Calculations

The model needs to account for temperature change in well flow as it has significant effects on water properties and hence on pressure drop. During production or upward flow, well flow temperature is expected to decrease as it loses heat to the formation, whereas during injection or downward flow, well flow temperature would be expected to increase as it gains heat from the formation. Shown below in figure 11 is a vertical section view of a water flowing well with a typical temperature profile from flow temperature at the well axis to the formation

temperature. The heat transfer mechanisms acting during well flow are convection between the flow axis and inner casing wall and conduction in the casing and cement sheath. This model adopts the method used by Willhite (1967) to determine an overall heat transfer coefficient based on the inside casing surface and the temperature difference between the fluid and cement/formation interface. The model can then determine heat flow from a well and hence the temperature difference over a flow increment.

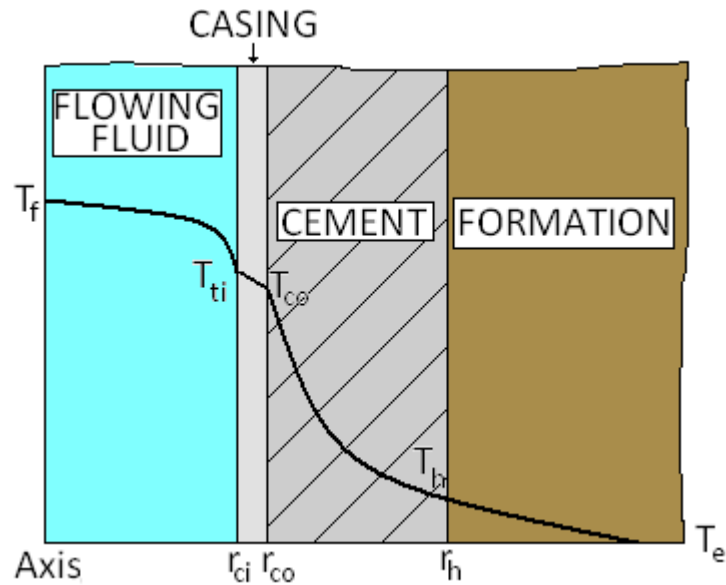


Figure 11 Well and formation temperature profile.

The calculation procedure is as follows. First the transient heat conduction is determined by equation 59

$$f(t) = \ln \frac{2\sqrt{\alpha t}}{r_h} - 0.29$$

Equation 59

Where α is the thermal diffusivity of the earth and t is time of flow. Second the overall heat transfer coefficient is determined

$$U_{ci} = \left(\frac{r_{ci} \ln \left(\frac{r_{co}}{r_{ci}} \right)}{\lambda_{cas}} + \frac{r_{ci} \ln \left(\frac{r_h}{r_{co}} \right)}{\lambda_{cem}} \right)^{-1}$$

Equation 60

Where λ_{cas} and λ_{cem} are the thermal conductivities of the casing and cement respectively. Third, using equation 61 the cement formation interface temperature is determined

$$T_h = \frac{f(t)r_{ci}U_{ci}T + \lambda_e T_e}{f(t)r_{ci}U_{ci} + \lambda_e}$$

Equation 61

Where k_e is thermal conductivity of formation and T is the temperature of flow. Fourth, equation 62 is used to calculate heat flow between the well and the formation per metre flow.

$$\dot{Q} = 2\pi r_{ci}U_{ci}(T - T_h)$$

Equation 62

The temperature at the end of the well increment can then be determined by rearranging the equation for heat transfer in a pipe

$$\dot{Q}\Delta Z = mc_p(T_2 - T_1)$$

$$T_2 = T_1 - \frac{Q\Delta Z}{mc_p}$$

Equation 63

Where c_p is specific heat capacity of water at average flow temperature and pressure and Z is the length of the increment.

3 CASE STUDY – HIJIORI, JAPAN: LONG TERM CIRCULATION TEST 2000 – 2002

3.1 HISTORY

The Hijiori EGS project was initiated by the Japanese Government and conducted by the New Energy and Industrial Technology Development Organization (NEDO) from 1984 until 2002. Four wells were drilled at the site: HDR-1 to 2200m and HDR-2, HDR-3 and SKG-2 to 1800m. From 1985 to 1991 a fractured reservoir was created at a depth of 1800m and a 90-day circulation test was performed. In 1992 further hydraulic fracturing created a second reservoir at 2200m and consequently HDR-2 and HDR-3 were deepened to 2300m (the extended section of HDR-2 was then renamed HDR-2a and shall be referred to by that title hence forth). After two short-term circulation tests in 1995 and 1996 the EGS site was prepared for the commencement of the long-term circulation test (LTCT) to begin in 2000 (Tenma et al 2008).

3.2 RELEVANT INFORMATION

The Hijiori EGS is shown below in figure 12 (Tenma et al 2008). It can be seen that the system consists of a two layered reservoir with all four wells drilled into the shallow layer at a depth of 1800m and where the temperature is 250°C. HDR-1, HDR-2a and HDR-3, extend to the deeper layer at 2200m where granite temperatures are 270°C. The black sections represent regions where the wells are cased whilst the white sections symbolise regions of open wellbore. A detailed description of casing profiles for each well is given in the appendix of this report. The diagram shows that SKG-2, HDR-2a and HDR-3 are open to the upper layer whilst HDR-1 is cased off. HDR-1 is open to the deeper layer as are HDR-2a and HDR-3. The diagram also provides the relative distances of the wells from one another at the different fracture zone depths. The temperature gradient of the formation at Hijiori is given in figure 13.

The LTCT was run in seven segments from late November 2000 to the end of August 2002 and was to determine the long-term production characteristics of the deep reservoir. In performing the LTCT, NEDO adopted SKG-2 as injector for the shallow fracture zone and HDR-1 as injector for the deep fracture zone with HDR-2a and HDR-3 acting as producers for both layers. The starting and finishing dates of the LTCT segments are shown in table II (Tenma et al 2008). Average mass flow rates, wellhead pressures and wellhead temperatures for each well during the different segments are displayed in tables III, IV and V respectively. The averaged data was taken from history plots given by Tenma et al (2008) which have been modified for this study to display the data in more noticeable manner. The modified plots are given in the appendices of this report.

It can be seen from the data that HDR-1 only was used as an injector during term 1. SKG-2 was shut in during this time and was used for shallow reservoir pressure observations. During term 2, run segment 5 both HDR-1

and SKG-2 were used as injectors at equal injection rates. In run segments 6 and 7 an injection ratio of 3:1 was used between HDR-1 and SKG-2. During all run segments water losses were significant as the total production rates did not equal the total injection rates. Injection pressures varied over the LTCT between 8 and 2MPa for HDR-1 and between 3 and 1MPa for SKG-2. This variation was due to the different injection flow rates throughout the LTCT. Production wellhead pressures were fairly consistent for HDR-2a varying between 1 and 2MPa. Wellhead pressure for HDR-3 remained around 1MPa throughout the LTCT. Wellhead temperatures were kept consistent for re-injection and remained between 25 and 35°C. HDR-2a production temperatures varied between 165 and 115°C. The lower temperatures measured at HDR-2a were attributed to scale build up on the sealing tube that covered the temperature sensor (Tenma et al 2008). Production temperature at HDR-3 remained in the vicinity of 160 to 180°C throughout the LTCT.

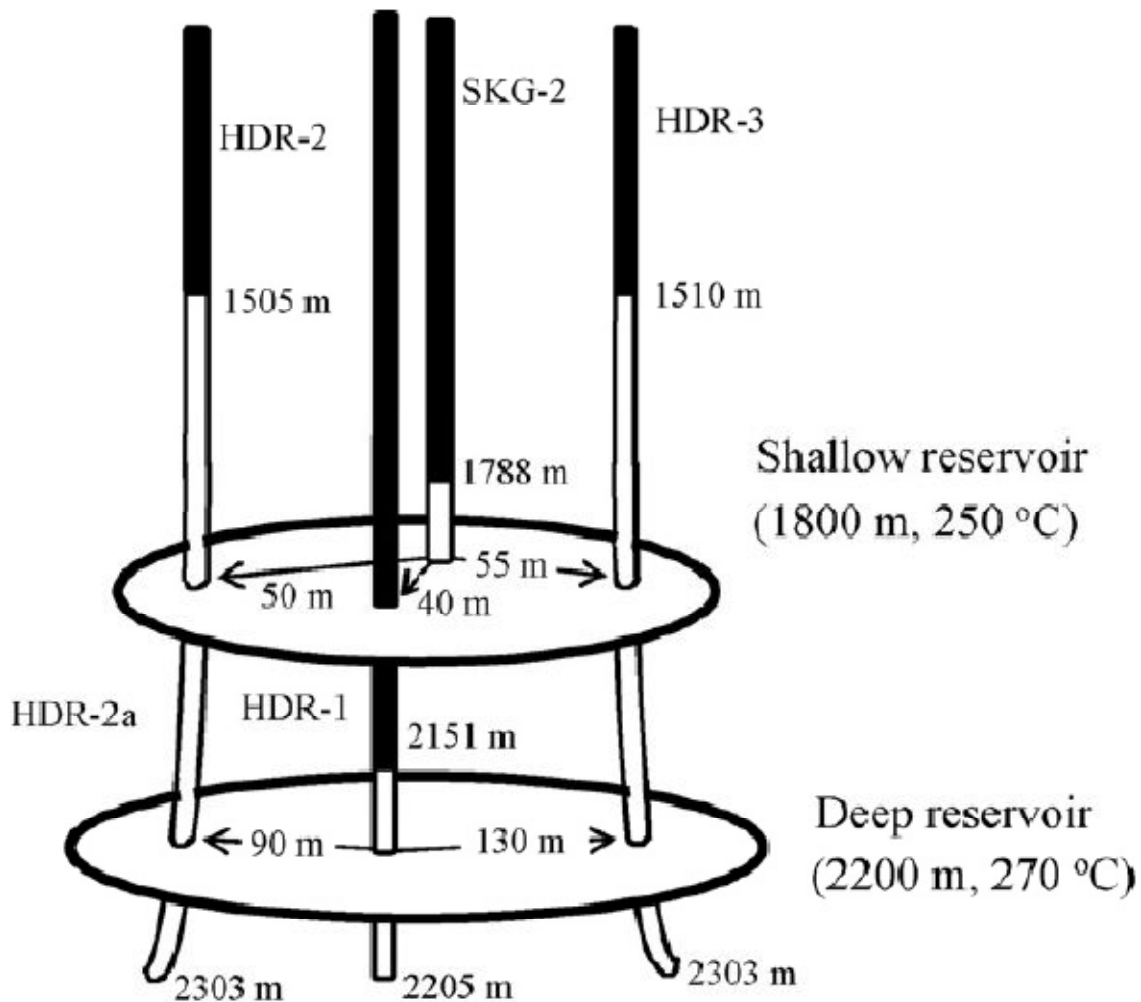


Figure 12 Illustration of the Hijiori EGS (Tenma et al 2008).

The shallow reservoir consisted of two main fractures whilst the deep reservoir consisted of four main fractures but whilst HDR-1 and HDR-3 communicated between all four fractures, HDR-1 and HDR-3 communicated only between three. In the study by Tenma et al (2008) it was assumed for the purposes of their model that these fractures were horizontal. The schematic of the mode from the Tenma et al study is shown in the appendices of this report.

Permeability data for the LTCT could not be found. However Yamaguchi et al (2000) provided that permeability based on the 1995 and 1996 short-term circulation tests is in the order of $1 \times 10^{-16} \text{ m}^2$ in the shallow reservoir. The study also stated that permeability between HDR-1 and HDR-2a was in the order of $7.5 \times 10^{-15} \text{ m}^2$ and between HDR-1 and HDR-3 permeability was $1 \times 10^{-15} \text{ m}^2$ (Yamaguchi et al 2000).

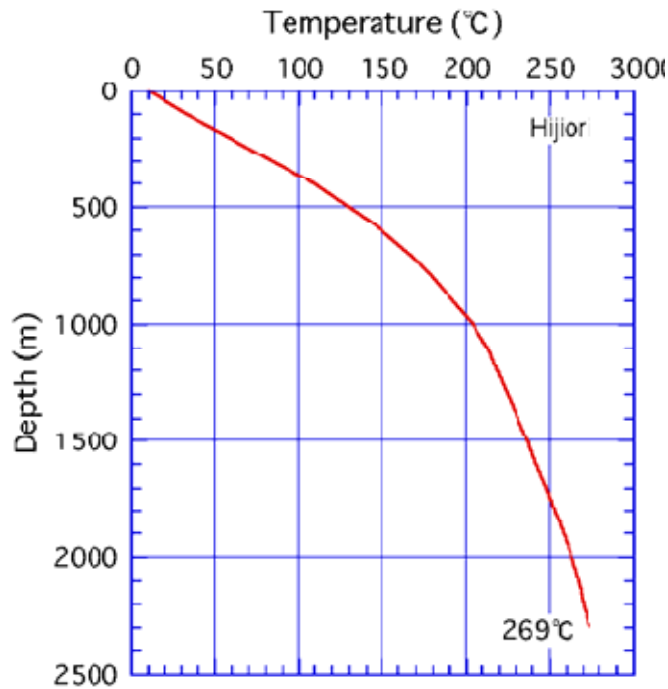


Figure 13 Temperature gradient of the formation at Hijiori (Morita et al 2005).

Table II Start and end dates for each run segment.

Term (Duration)	Run Segment (RS)	Start and end dates (day/month/year)
1 (333 days)	1	27/11/2000 – 21/04/2001
	2	21/04/2001 – 11/06/2001
	3	11/06/2001 – 25/09/2001
	4	25/09/2001 – 15/11/2001
2 (126 days)	5	23/12/2001 – 08/04/2002
	6	08/04/2002 – 28/04/2002
3 (92 days)	7	01/06/2002 – 31/08/2002

Table III Average injection and production mass flow rates for each well during each run segment.

Term	Run Segment	HDR-1 (Injection) kg/s	SKG-2 (Injection) kg/s	HDR-2a (Production) kg/s	HDR-3 (Production) kg/s
1	1	18.35	Shut In	5.00	4.50
	2	16.70	Shut In	5.00	4.50
	3	16.70	Shut In	2.80	2.20
	4	16.70	Shut In	4.50	2.20
2	5	8.35	8.35	7.00	2.50
	6	12.53	4.17	6.00	2.50
3	7	12.53	4.17	7.80	2.50

Table IV Average wellhead pressures for each well during each run segment.

Term	Run Segment	HDR-1 (Injection) MPa	SKG-2 (Injection) MPa	HDR-2a (Production) MPa	HDR-3 (Production) MPa
1	1	8	Shut In	1	1
	2	7	Shut In	1	1
	3	6.5	Shut In	1	1
	4	6	Shut In	1	1
2	5	2	3	2	1
	6	4	1	1	1
3	7	4	1	1	1

Table V Average wellhead temperatures for each well during each run segment.

Term	Run Segment	HDR-1 (Injection) °C	SKG-2 (Injection) °C	HDR-2a (Production) °C	HDR-3 (Production) °C
1	1	25	Shut In	165	180
	2	35	Shut In	165	180
	3	35	Shut In	120	180
	4	35	Shut In	115	160
2	5	25	25	130	170
	6	35	35	130	170
3	7	35	35	130	170

3.3 MODEL ANALYSIS

An analysis of the data from the Hijiori LTCT in run segments 1, 5 and 7 was performed using the model to test its validity. With the aid of Microsoft Excel® the model was to provide estimates of reservoir flow impedance, permeability and skin factors for the Hijiori EGS. The model was also to give predicted well profiles of temperature, pressure and steam quality. Values of wellhead temperature and pressure as well as reservoir permeability were to be compared with the data from the LTCT. The analysis was performed using the following method.

- 1) Using injection wellhead data (pressure, temperature and flow rate) and casing profiles as inputs, the well flow model determined:
 - Injection well profiles
 - Injection wellbore pressures.
- 2) Fracture flow geometries were calculated based on values of D and n as well as assumptions of w , H , m and θ .
- 3) Fracture aperture and roughness were estimated.
- 4) Reservoir pressure drop ΔP_{total} was determined along with k_{total} and S using fracture flow geometries from step 2 and fracture aperture and roughness from step 3 as inputs to the reservoir model.
- 5) Production wellbore pressure was determined by subtracting ΔP_{total} from injection wellbore pressure.
- 6) Using production wellbore data (pressure, temperature and flow rate) and well casing profiles as inputs, the well flow model determined:
 - Production well profiles
 - Production wellhead pressures.
- 7) If the value of production wellhead pressure was not within 0.5MPa of the average value from literature, the procedure returned to step 3, if it was within 0.5MPa then the output was accepted.

The method is best explained with the use of a block flow diagram as shown in figure 14. A sample calculation is also given in the appendices of this report

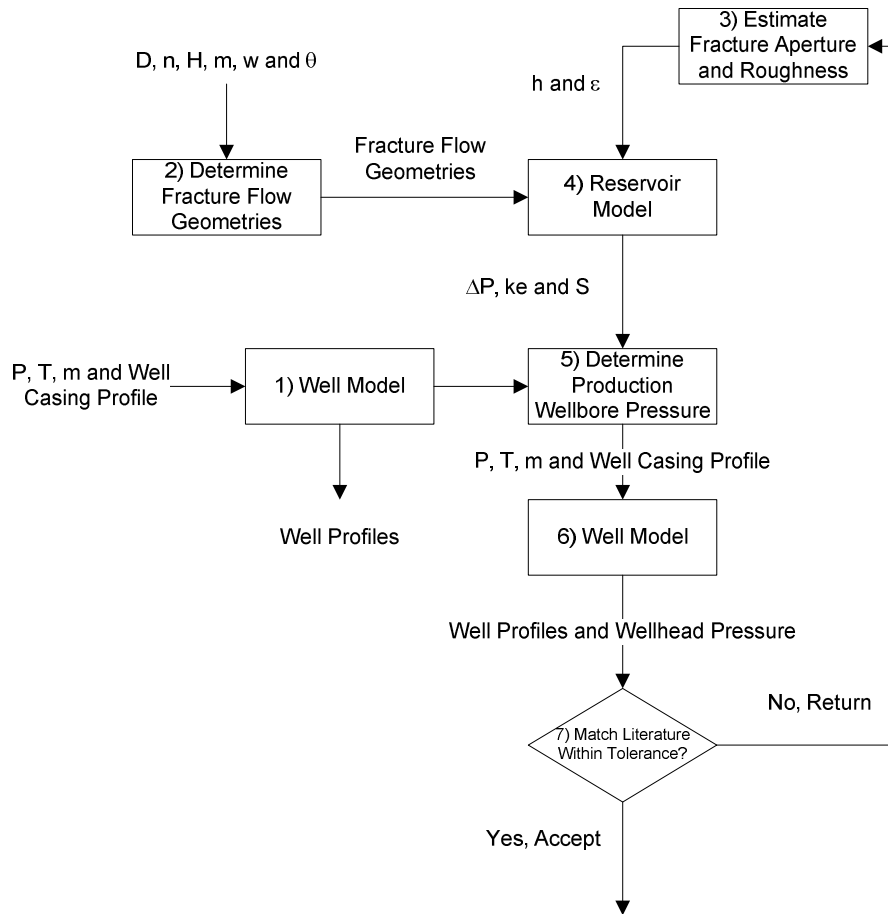


Figure 14 Block flow diagram of procedure used to analyse data from the Hijiori LTCT.

4 RESULTS

4.1 WELL PROFILES

Term 1 – Run Segment 1

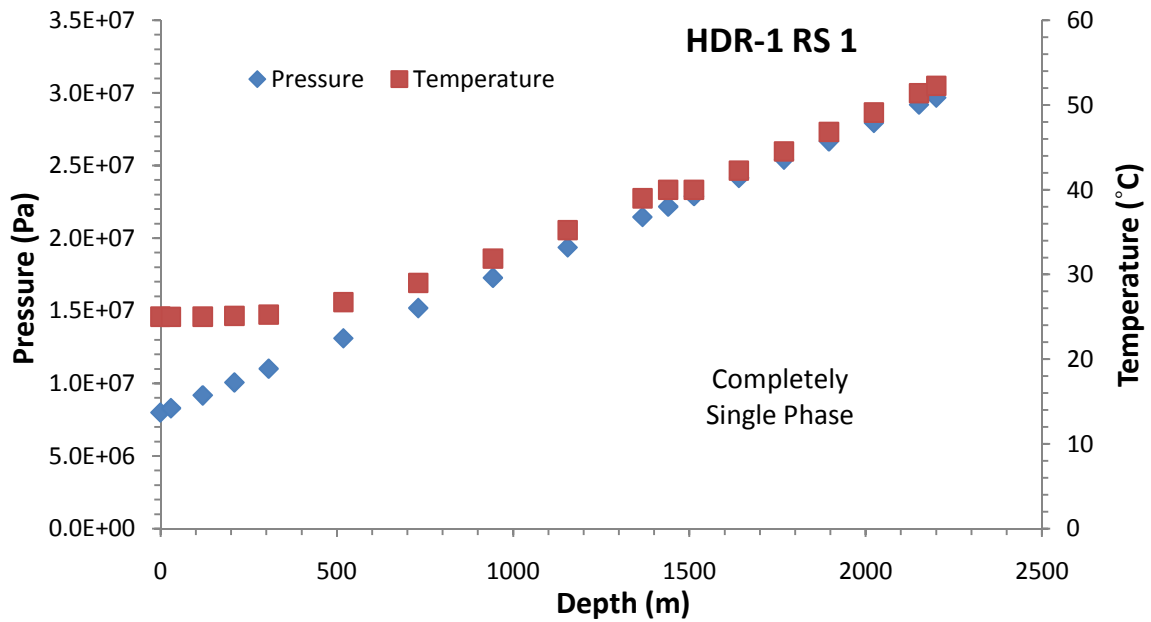


Figure 15 Model determined pressure and temperature profiles for HDR-1 during run segment 1 of the Hijiori LTCT.

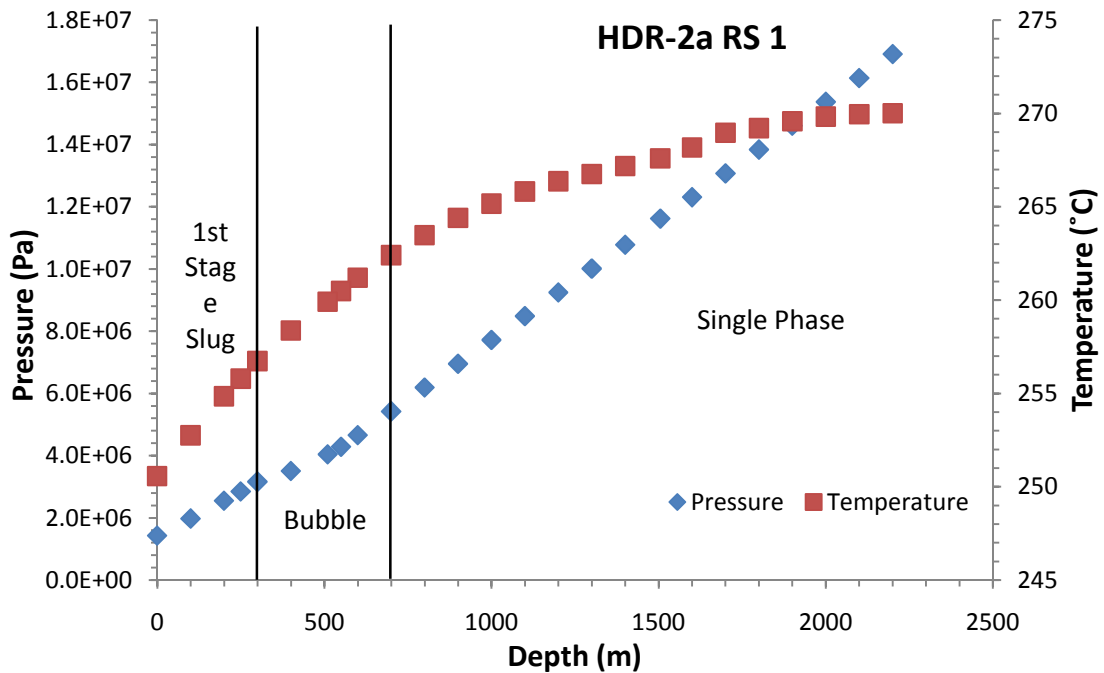


Figure 16 Model determined pressure and temperature profiles for HDR-2 during run segment 1 of the Hijiori LTCT.

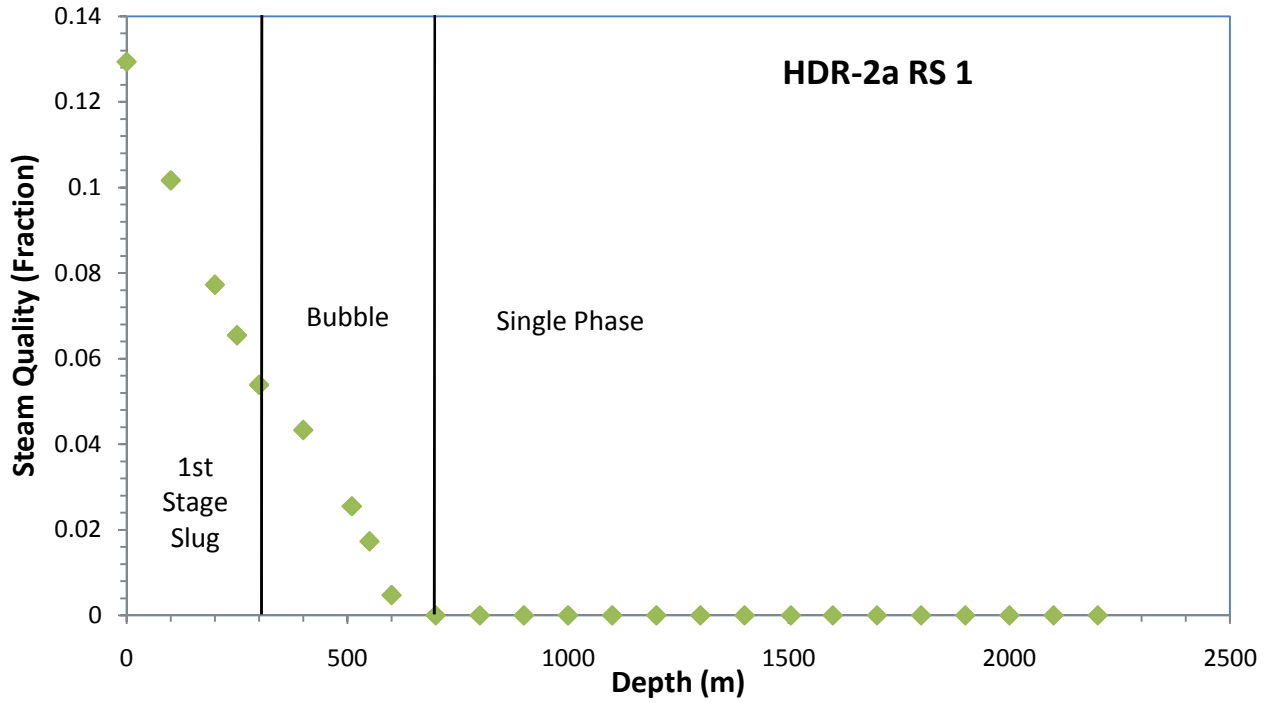


Figure 17 Model determined steam quality profile for HDR-2 during run segment 1 of the Hijiori LTCT.

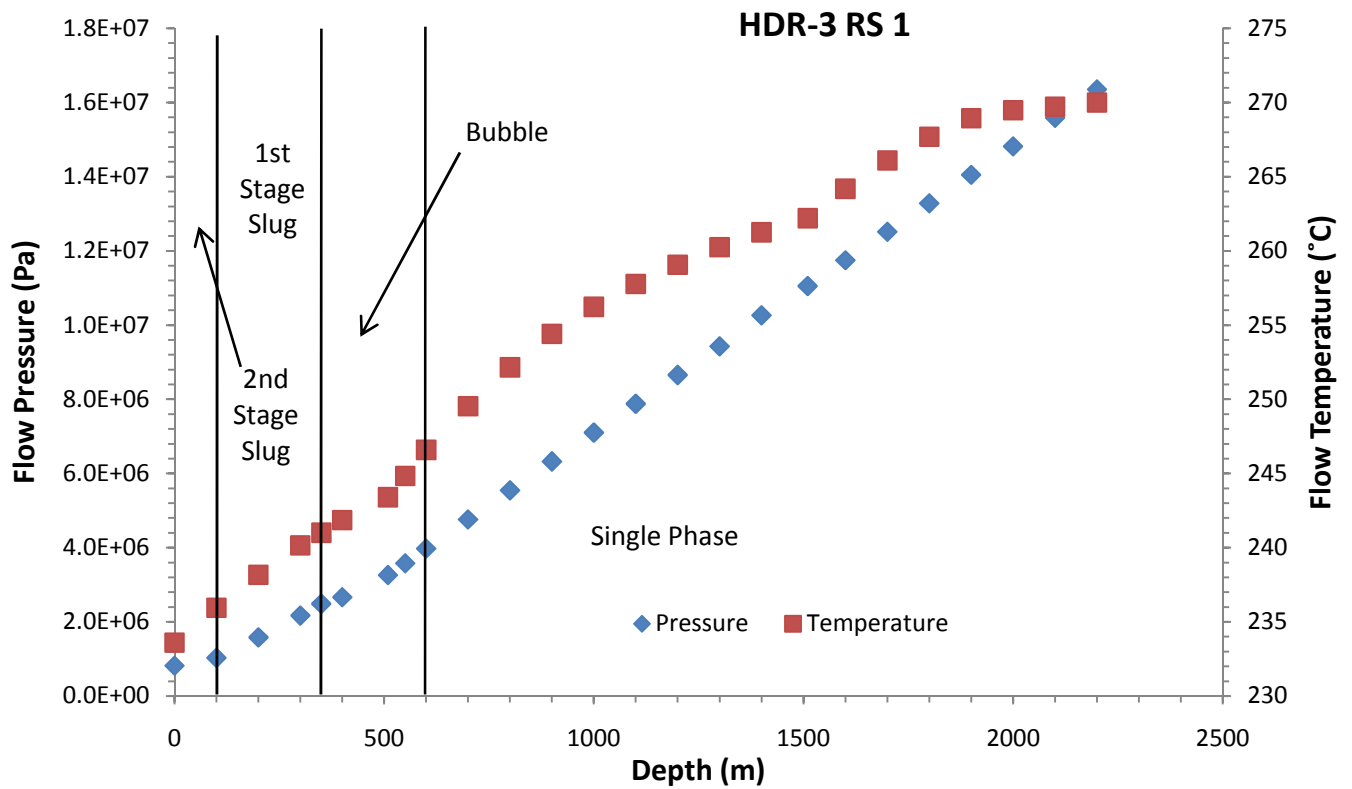


Figure 18 Model determined pressure and temperature profiles for HDR-3 during run segment 1 of the Hijiori LTCT.

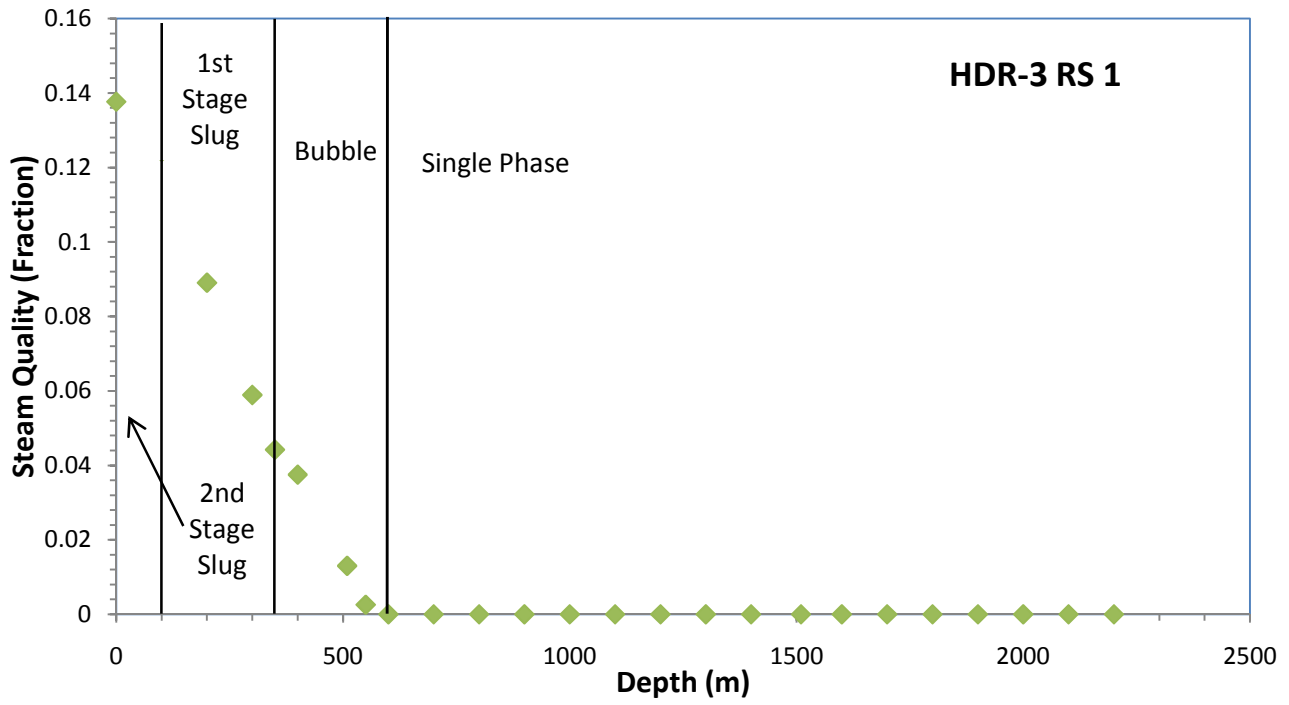


Figure 19 Model determined steam quality profile for HDR-3 during run segment 1 of the Hijori LTCT.

Term 2 – Run Segment 5

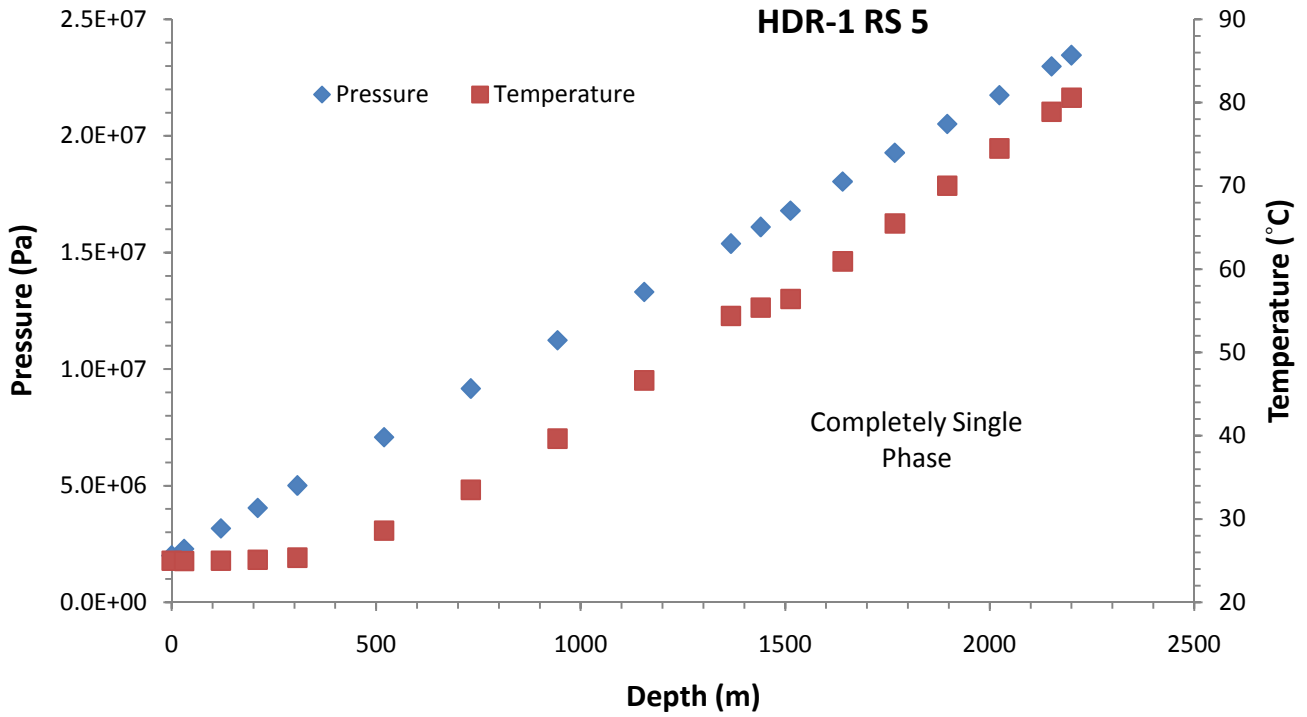


Figure 20 Model determined pressure and temperature profiles for HDR-1 during run segment 5 of the Hijiori LTCT.

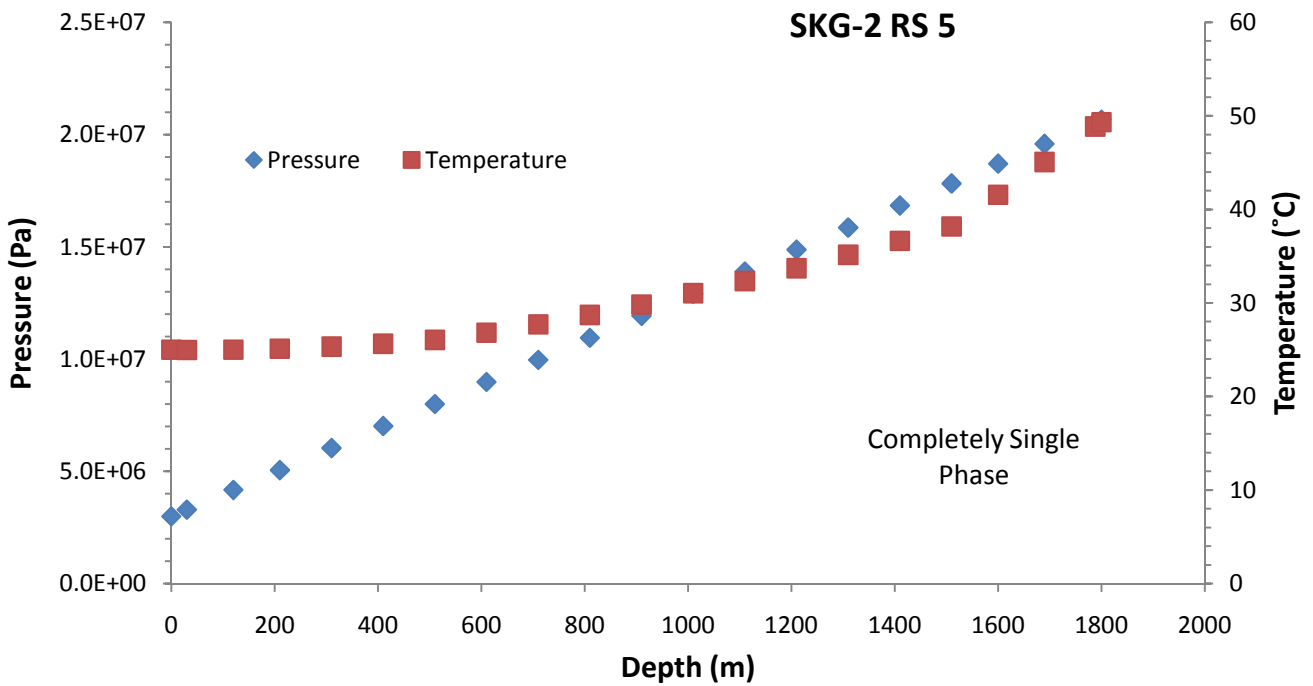


Figure 21 Model determined pressure and temperature profiles for SKG-2 during run segment 5 of the Hijiori LTCT.

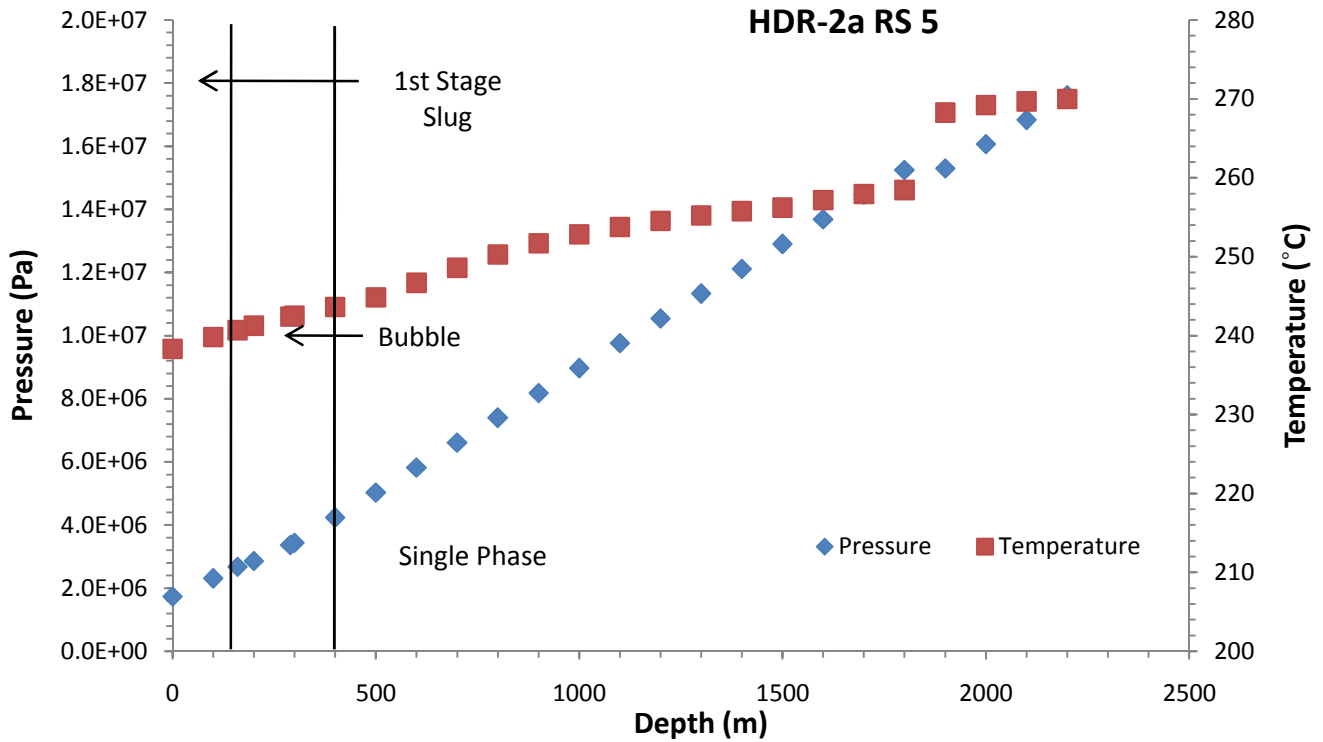


Figure 22 Model determined pressure and temperature profiles for HDR-2 during run segment 5 of the Hijiori LTCT.

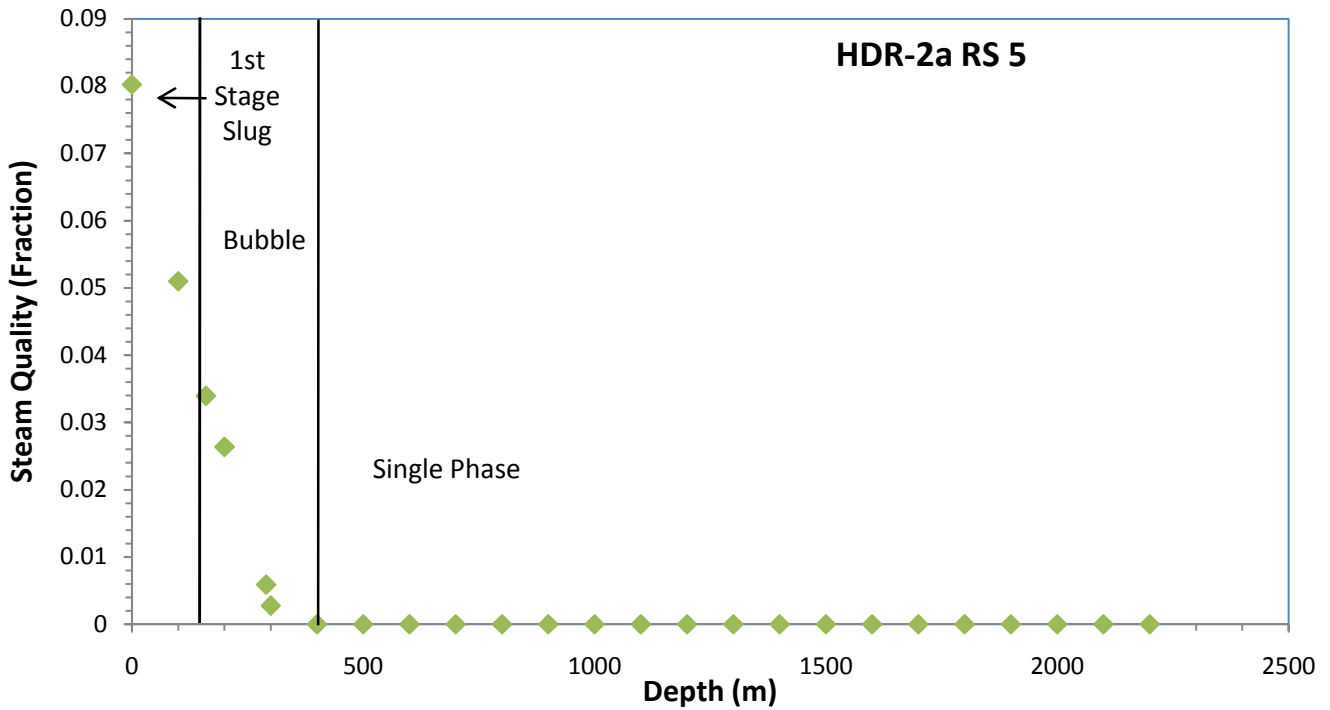


Figure 23 Model determined steam quality profile for HDR-2 during run segment 5 of the Hijiori LTCT.

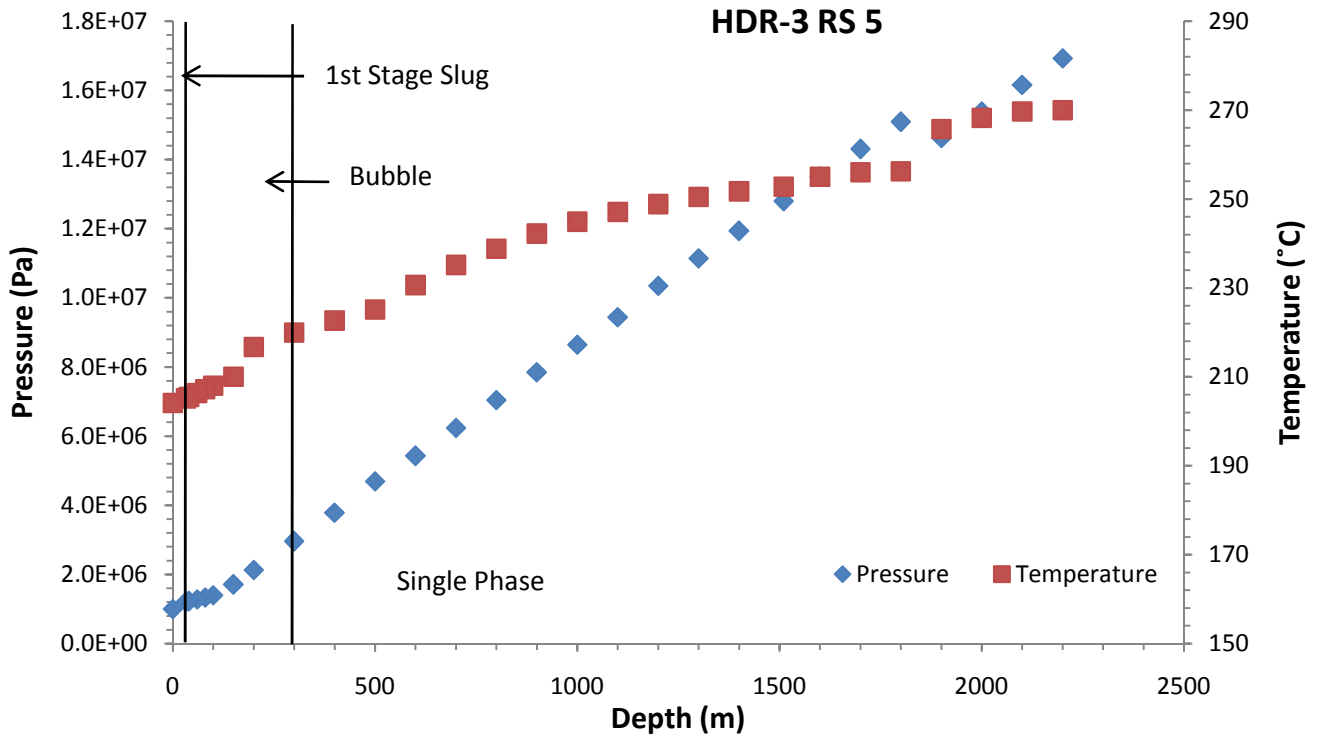


Figure 24 Model determined pressure and temperature profiles for HDR-3 during run segment 5 of the Hijori LTCT.

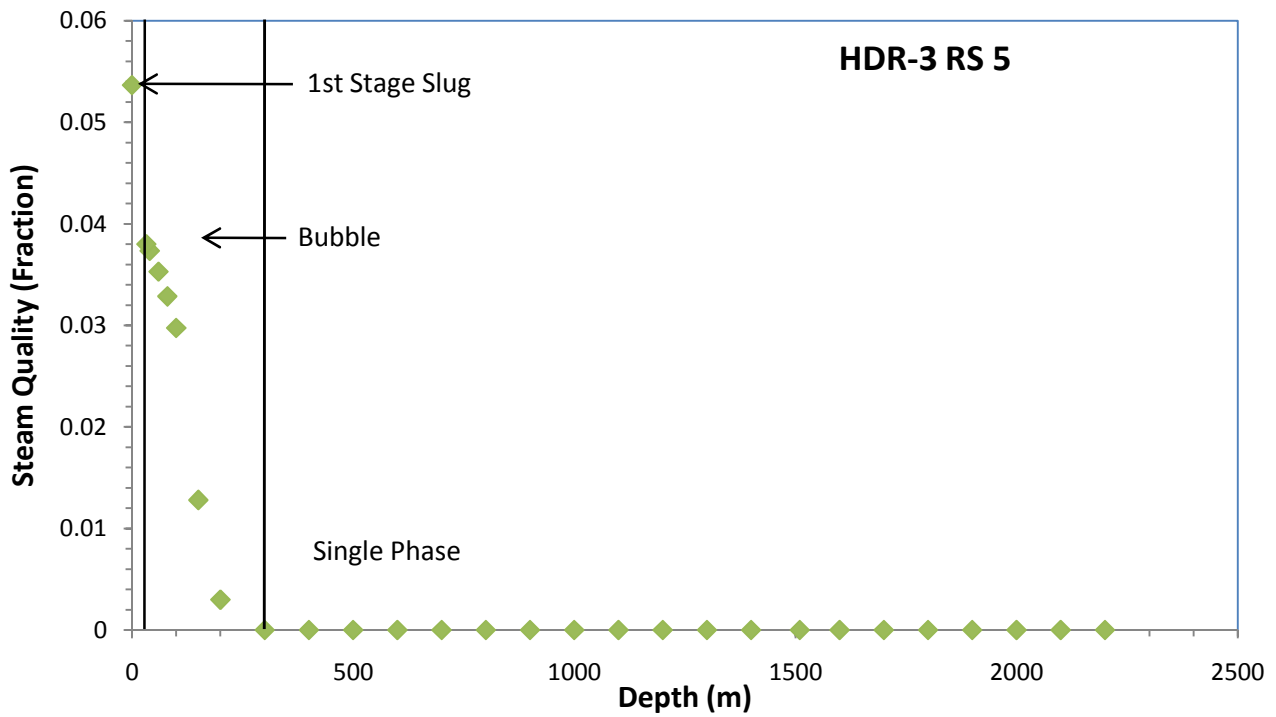


Figure 25 Model determined steam quality profile for HDR-3 during run segment 5 of the Hijori LTCT.

Term 3 – Run Segment 7

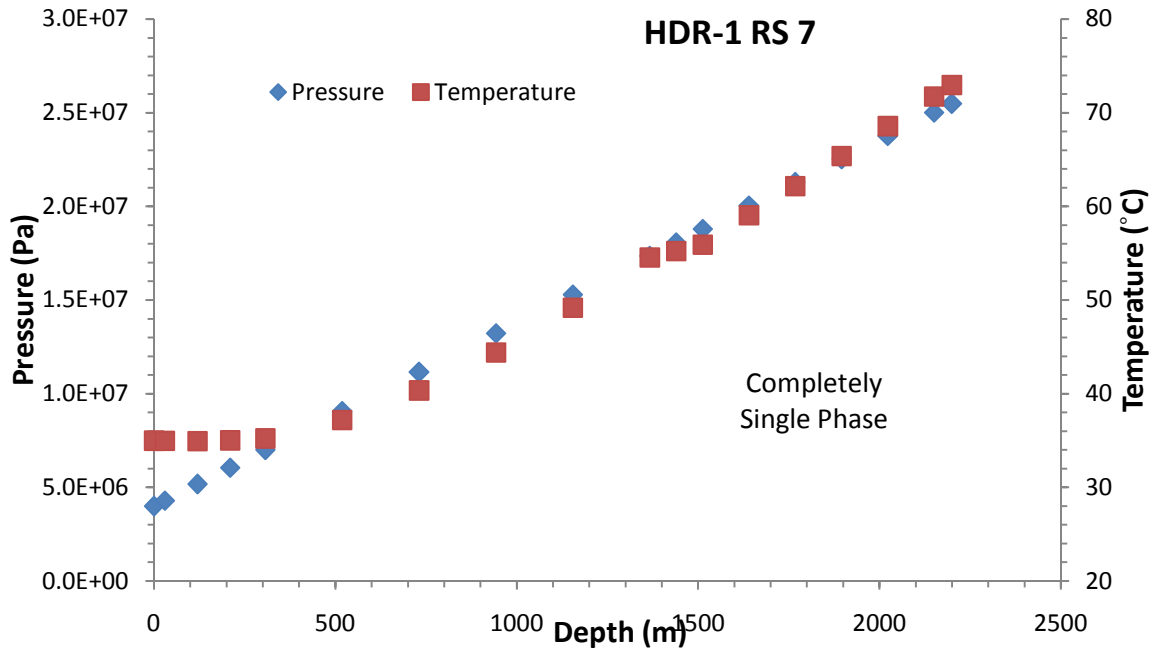


Figure 26 Model determined pressure and temperature profiles for HDR-1 during run segment 7 of the Hijiori LTCT.

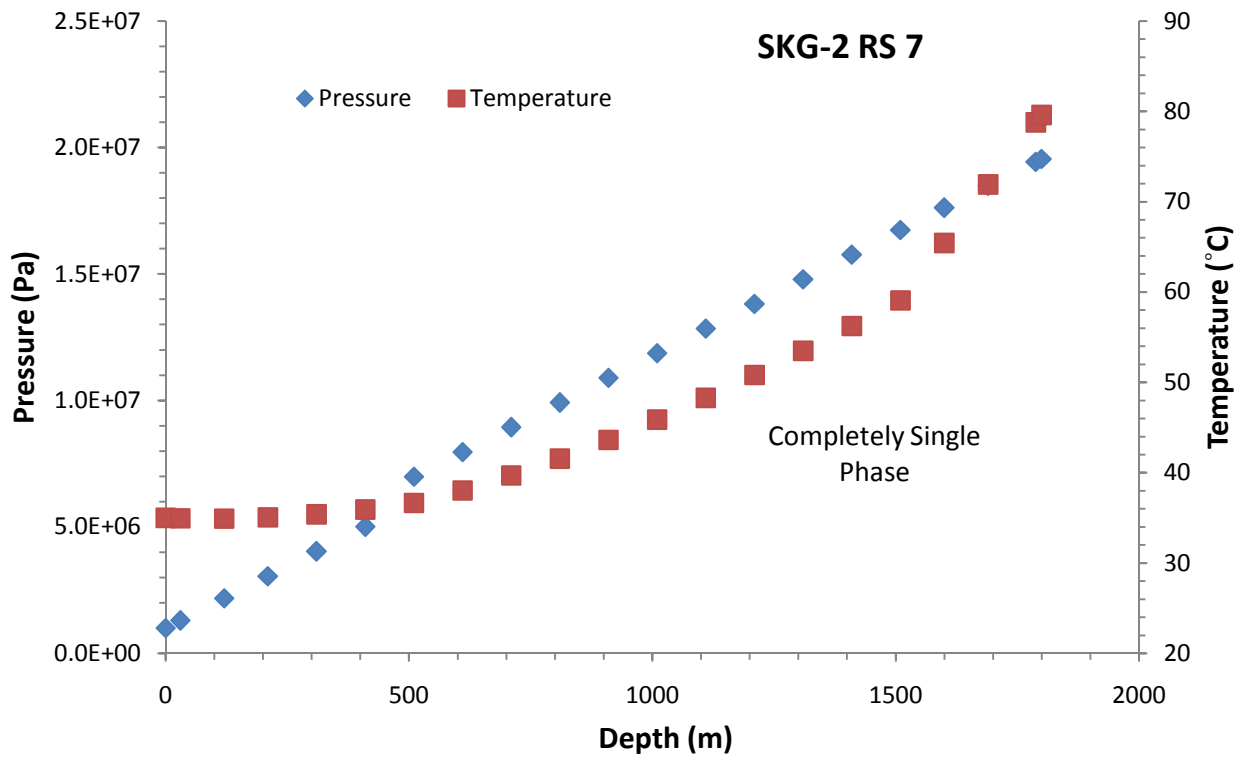


Figure 27 Model determined pressure and temperature profiles for SKG-2 during run segment 7 of the Hijiori LTCT.

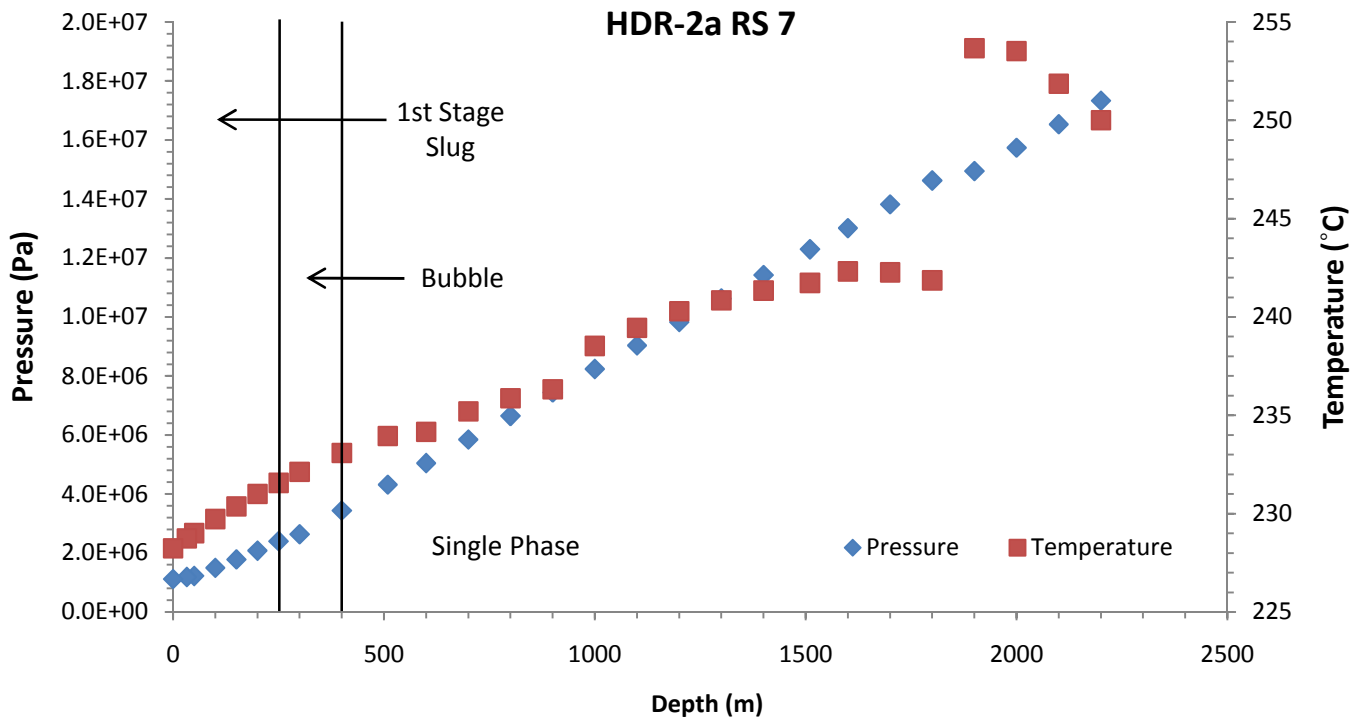


Figure 28 Model determined pressure and temperature profiles for HDR-2 during run segment 7 of the Hijiori LTCT.

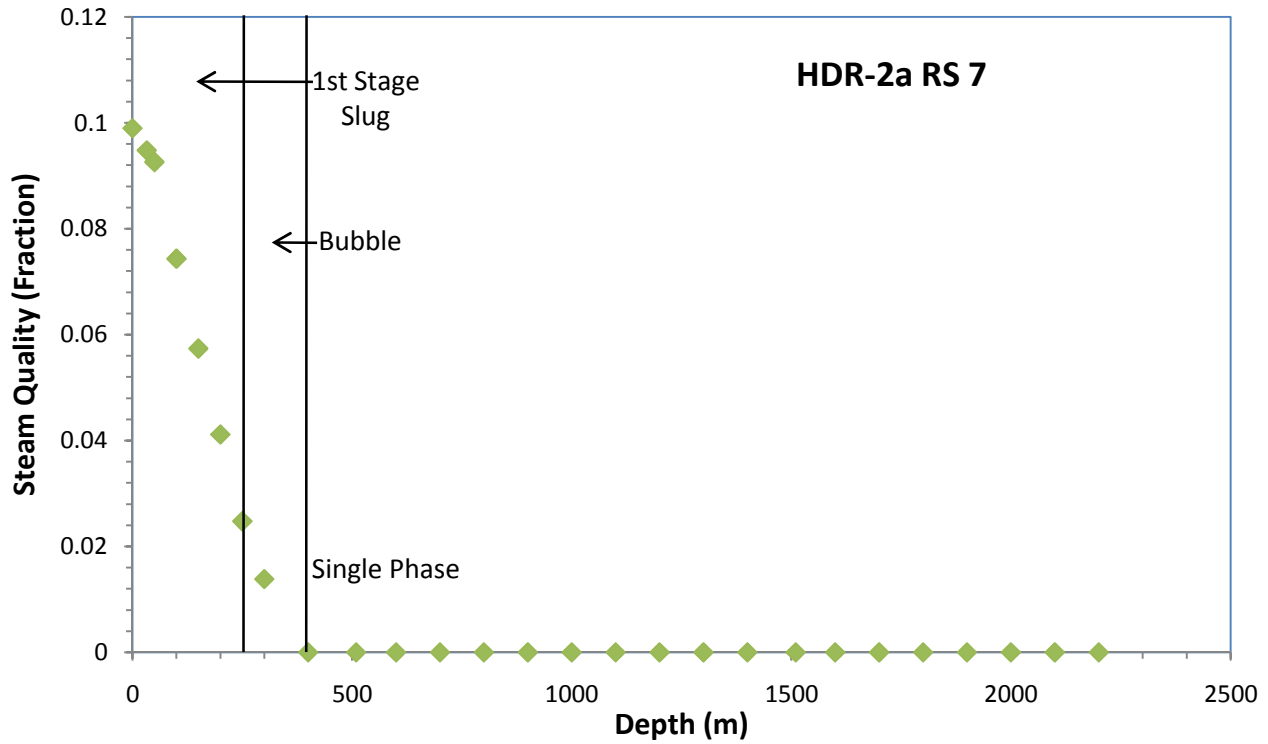


Figure 29 Model determined steam quality profile for HDR-2 during run segment 7 of the Hijiori LTCT.

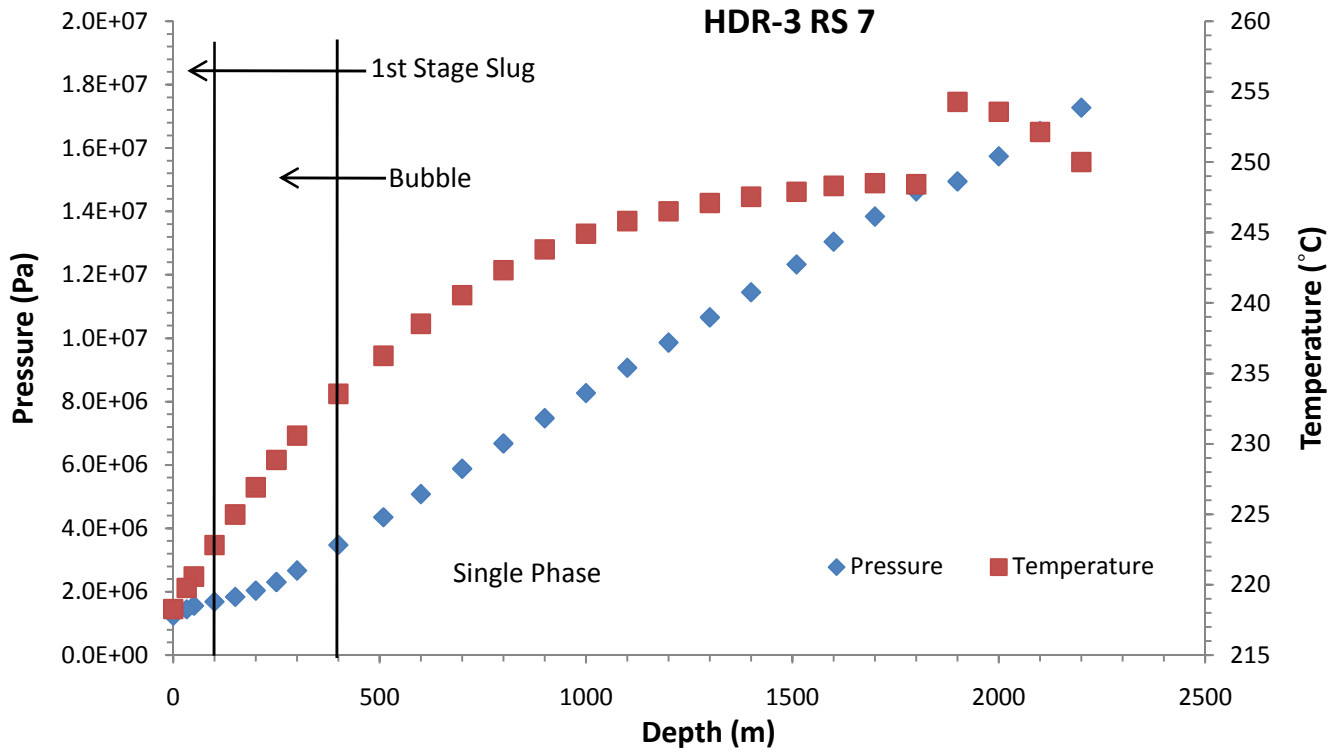


Figure 30 Model determined pressure and temperature profiles for HDR-3 during run segment 7 of the Hijori LTCT.

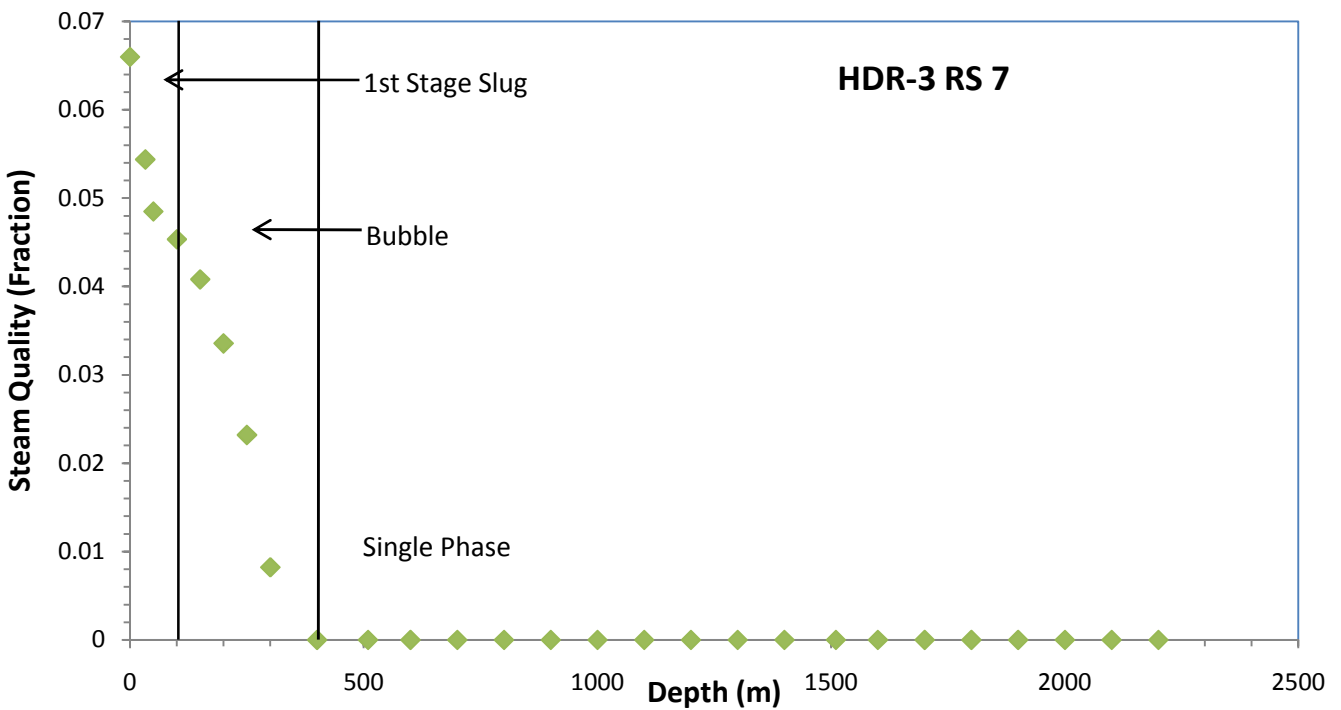


Figure 31 Model determined steam quality profile for HDR-3 during run segment 7 of the Hijori LTCT.

4.2 COMPARISON TO LITERATURE

Wellhead Pressure



Figure 32 Comparison of model predicted and literature values of wellhead pressure for HDR-2.

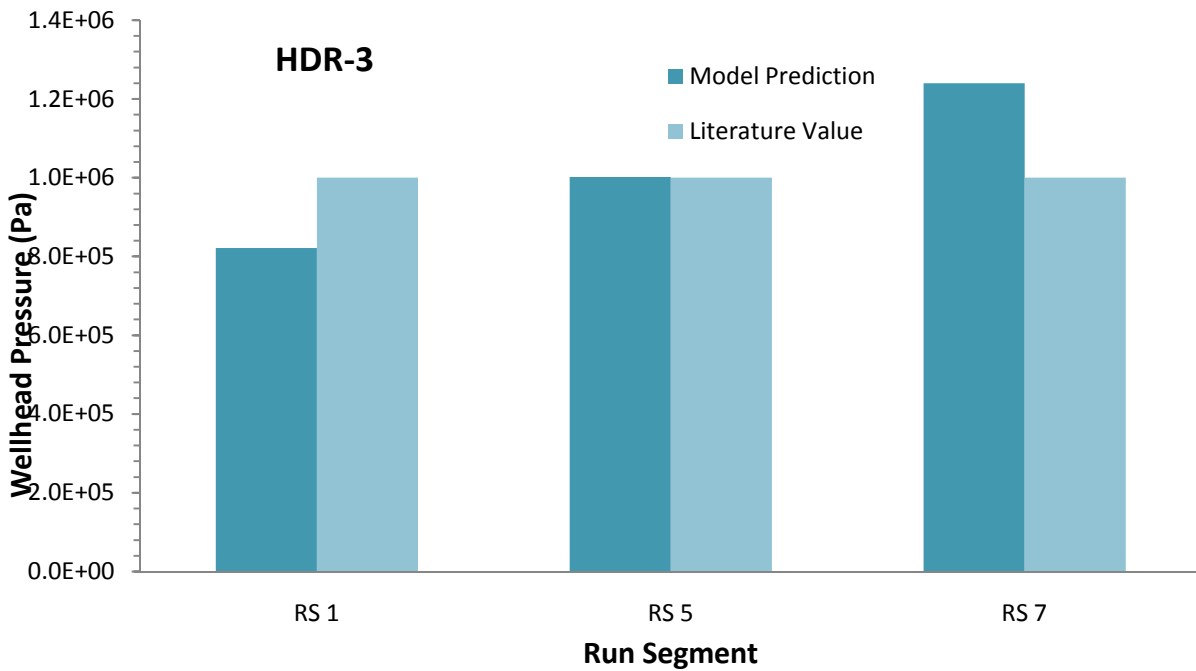


Figure 33 Comparison of model predicted and literature values of wellhead pressure for HDR-3.

Wellhead Temperature

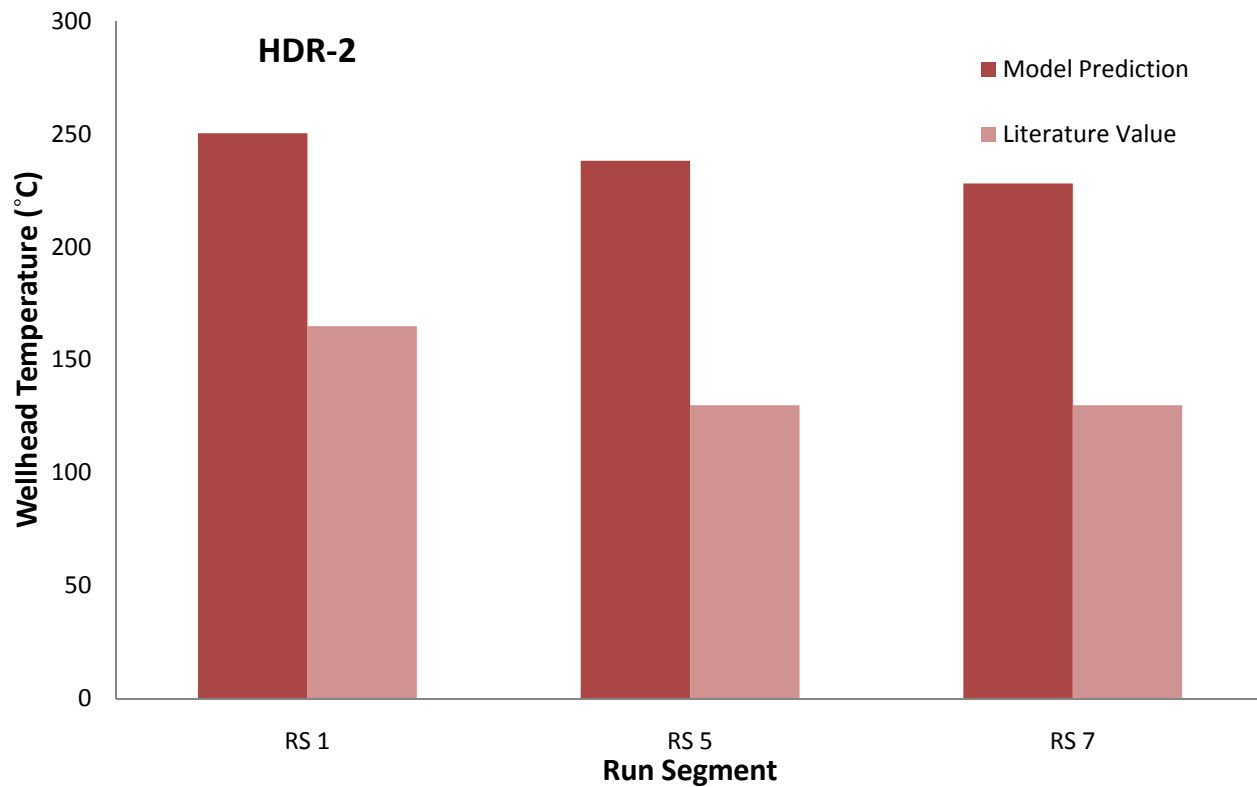


Figure 34 Comparison of model predicted and literature values of wellhead temperature for HDR-2.

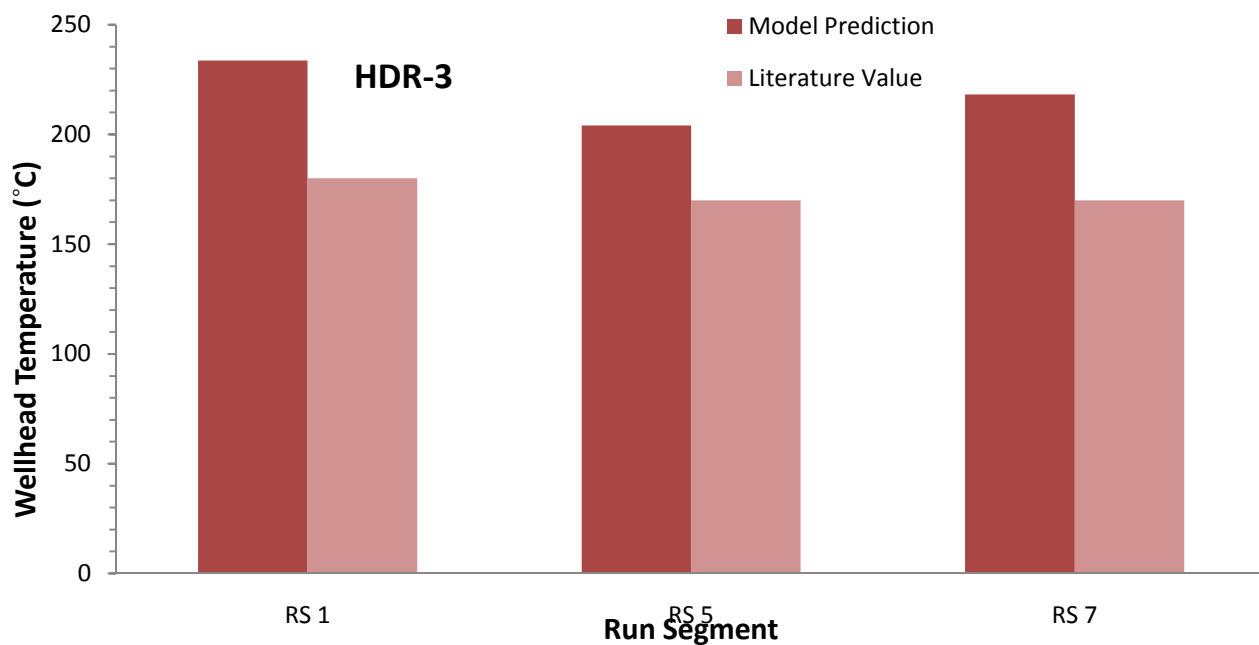


Figure 35 Comparison of model predicted and literature values of wellhead temperature for HDR-3.

Average Permeability

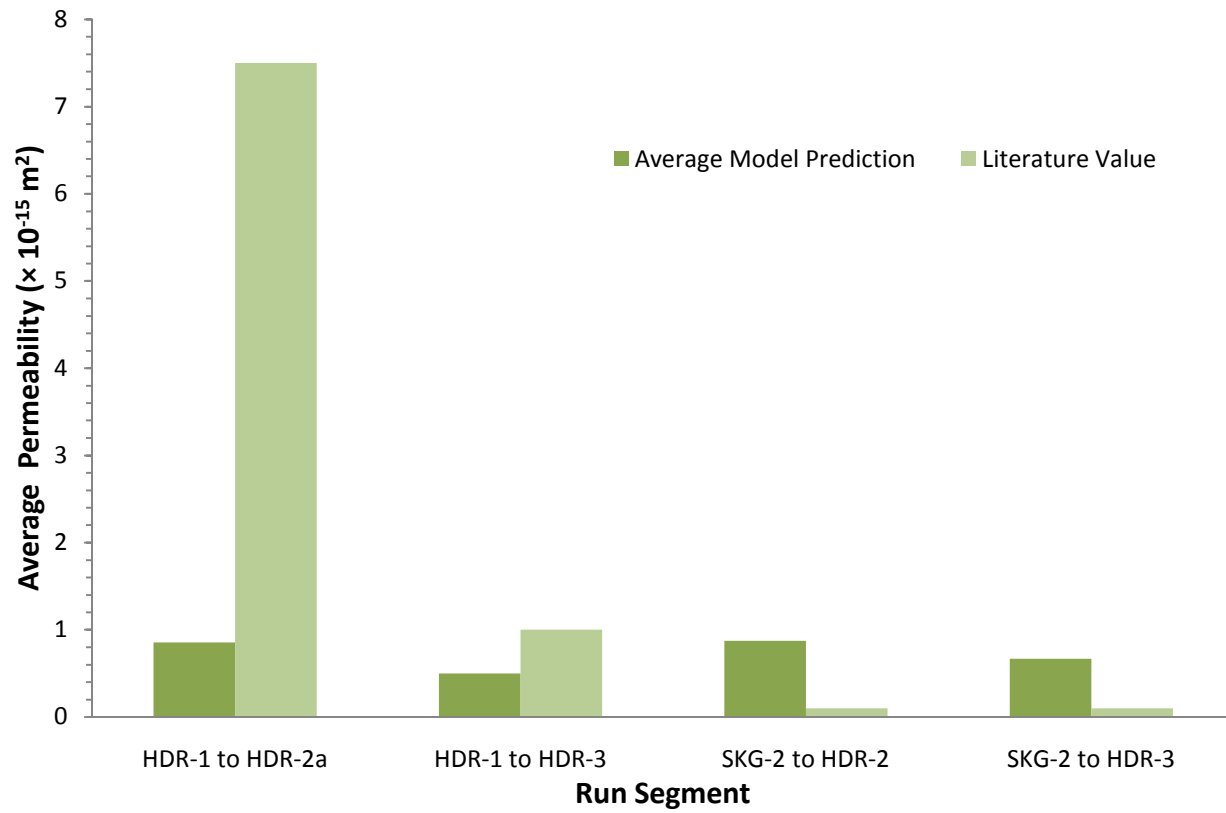


Figure 36 Comparison of model predicted and literature values of average permeability for the different reservoir sections.

4.3 RESERVOIR CHARACTERISTICS

Flow Impedance

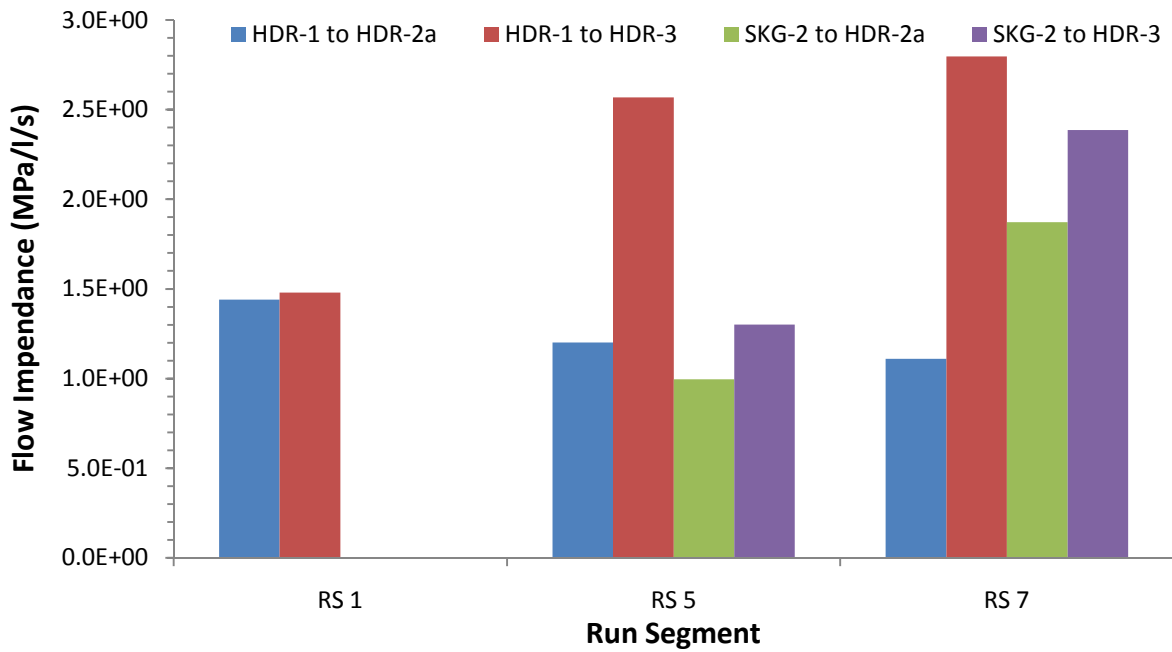


Figure 37 Model determined flow impedance values for the Hijiori LTCT.

Total Permeability

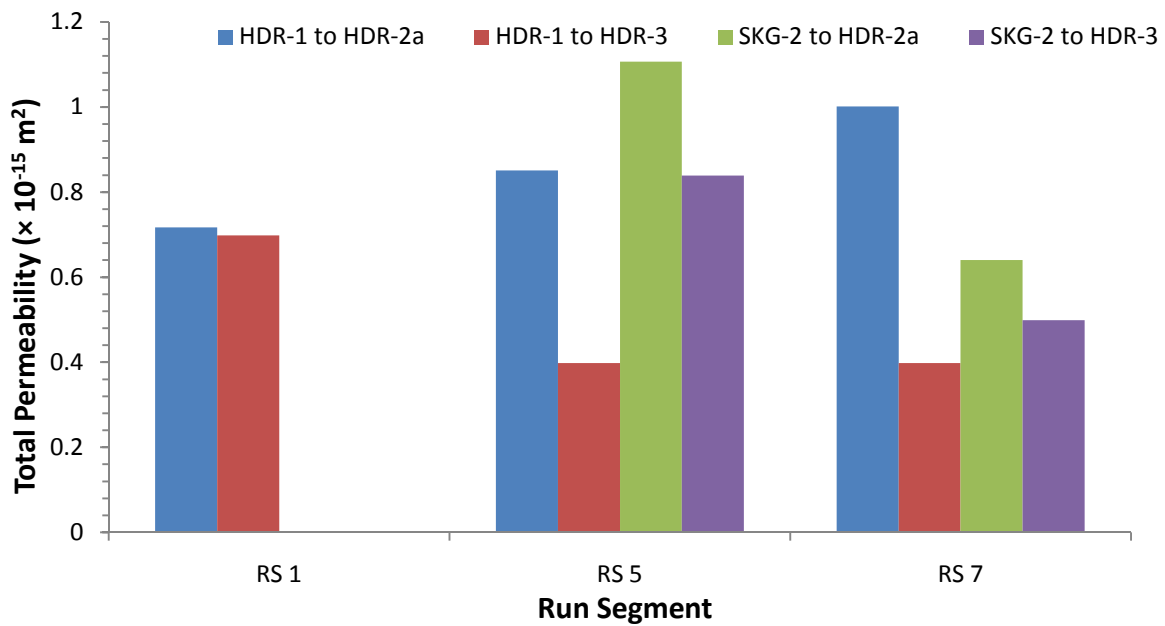


Figure 38 Model determined fracture permeability values for the Hijiori LTCT.

Absolute Skin Factor

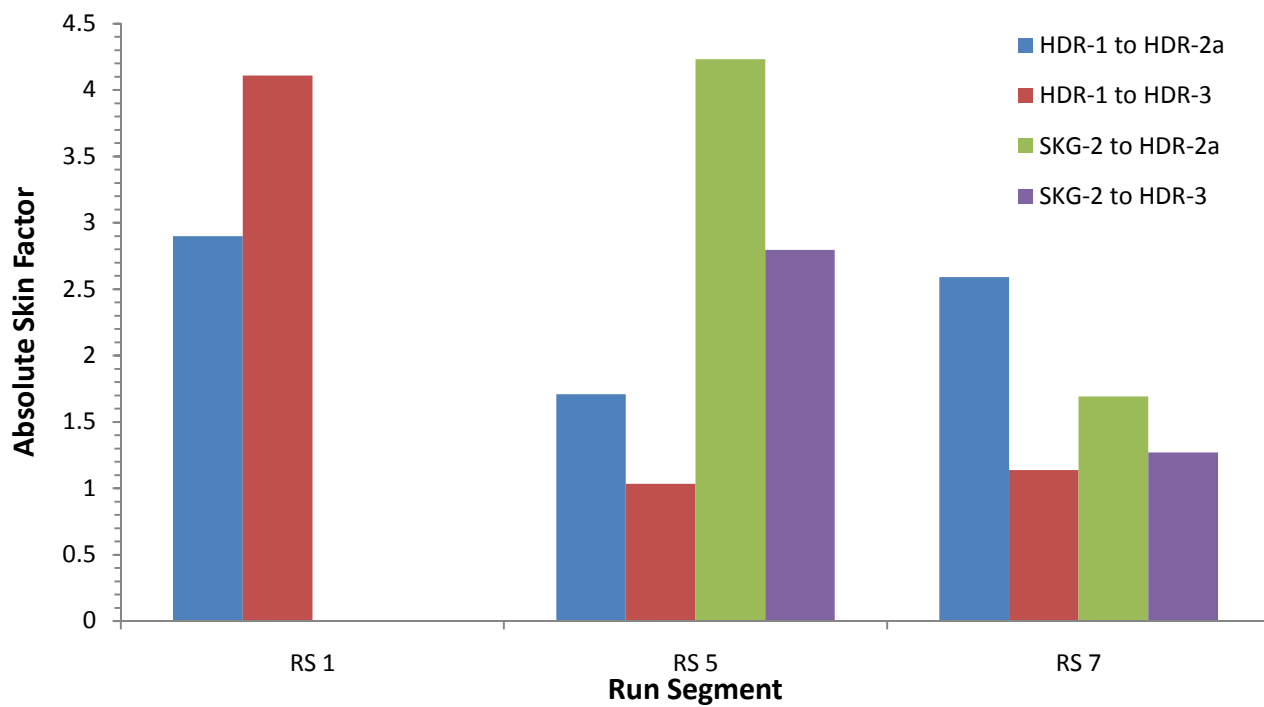


Figure 39 Model determined absolute skin factor values for the Hijiori LTCT.

5 DISCUSSION

5.1 WELL PROFILES

Injection wells

Figure 15 displays the temperature and pressure profiles of HDR-1 for run segment (RS) 1 where it was the only injector in use. The pressure profile shows a linear increase with depth implying that little density changes occurred during injection in RS 1. This result was intuitive as injection temperature was initially only 25°C and flow pressure was high enough to keep water in the single liquid phase. The pressure at the wellbore was estimated to reach nearly 30MPa. The temperature profile also increased with depth. Flow temperature remained steady for about the first 400 to 500m but then increased almost linearly until the final depth of 2200m where it reached 52.3°C. Temperature rise appears to stall temporarily in the section of the well between about 1350 and 1500m. This was due to the model accounting for extra cement insulation in that section of the well where two casing layers overlapped (see appendices for casing profile).

The injection well profiles for RS 5 are shown in figures 20 and 21. Again for HDR-1 pressure and temperature increased with depth. However wellbore pressure only reached approximately 24MPa and flow temperature reached 80°C. The difference in wellbore pressure from RS 1 is due injection pressure during RS 5 being only 2MPa as opposed to 8MPa in RS 1 hence giving a difference of 6MPa. The greater increase in flow temperature was due to a smaller mass flow rate during RS 5 into HDR-1 than in RS 1. Injection rates during RS 1 were over 18kg/s on average whilst in RS-5 mass flow was only 8kg/s. On inspection of equation 63 it is obvious that as mass flow rate decreases, temperature difference increases. The pressure and temperature profiles for SKG-2 are similar to those for HDR-1 during RS 5. Figure 21 shows a linear increase in pressure with depth but a smooth parabolic increase in temperature with depth. Wellbore pressure and temperature for SKG-2 reached just over 20MPa and 49°C respectively. These values are lower than those of HDR-1 for RS 5 due to SKG-2 being 400m shorter than HDR-1 thus lessening the hydrostatic head and heat transfer effects.

Results were similar for the injection well profiles in run segment 7 in figures 26 and 27. The model again predicted linear increases in pressure and parabolic increases in temperature with depth and completely single phase liquid flow. Wellbore pressures reached 25.5MPa and 19.5MPa for HDR-1 and SKG-2 respectively. The increase in injection pressure to 4MPa at HDR-1 resulted in a larger wellbore pressure than in RS-5 where the injection pressure was only 2MPa. The same was true with SKG-2 only a decrease in injection pressure to 1MPa from 3MPa in RS 5 resulted in a decrease in wellbore pressure. Wellbore temperatures reached 73°C and 80°C for HDR-1 and SKG-2 respectively. The effect of mass flow rate on the model's temperature profile estimations is

made most apparent by this result. Despite flowing for 400m less and thus having less flow length to absorb heat, the temperature of flow in the shallower injection wellbore was higher than in the deeper wellbore due to lower velocity. The injection ratio for RS 7 was HDR-1:SKG-2 equals 3:1 where as in RS-5 the ratio was 1:1.

Production Wells

The production well profiles for RS 1 are shown in figures 16 to 19. For the temperature profile of HDR-2a in figure 16 the model predicted a parabolic decrease as depth approached zero. The final wellhead temperature was calculated as 250.5°C after assuming a wellbore temperature of 270°C giving a temperature difference of $\Delta T = 19.5^\circ\text{C}$. The model also predicted the presence of three flow regimes. Flow is envisaged to begin and continue as single phase up until 700m where bubble flow then presides until 300m where first stage slug flow takes over. This result can be understood better upon examination of figure 17 which shows the steam quality profile for HDR-2a. The model calculated that steam quality would increase from 0% to around 13% from 700m upward as flow pressure decreases. The decrease in flow pressure up the length of the well was rapid compared to the decrease in flow temperature. This caused pressure determined liquid enthalpy to decrease at a rate much faster than temperature determined liquid enthalpy and eventually the latter became greater the former causing steam quality to increase to more than 0%. For the pressure profile of HDR-2a given in figure 16 the model indicated that pressure decreased linearly during single phase flow. The pressure gradient became less severe in the two-phase flow regimes due to decreases in density creating less hydrostatic head giving a final wellhead pressure of 1.4MPa which after a wellbore pressure of 16.9MPa gives $\Delta P = 15.5\text{MPa}$.

The model returned similar well profiles for HDR-3 in figures 17 and 19 except a slightly lower flow pressure toward the top of the well resulted in second stage slug presiding as the flow regime at depth 0m. Again profiles of temperature and pressure were predicted as decreasing in parabolic and linear manners respectively but the estimated wellhead temperature of 233.6°C ($\Delta T = 36.3^\circ\text{C}$) differed to that of HDR-2a. As was the case for the injection wells, the difference in mass flow rate is responsible for this result. Its effect on the model is more apparent in this case as mass flow rate in HR-3 was 4.5kg/s and 5kg/s in HDR-2a. Thus a 0.5kg/s difference produced a 16.9°C difference at the wellhead. The pressure difference across the well was similar to that of HDR-2a being in the order of 15.5MPa to give a wellhead pressure of 0.8MPa. The steam quality profile produced by the model (figure 19) for HDR-3 was much like the one produced for HDR-2a only that steam quality increased to nearly 14% and at a faster rate.

The model gave different temperature and pressure profiles for HDR-2a and HDR-3 in RS 5 and 7 compared with those from RS-1. In RS-1 only HDR-1 was used for injection into and therefore all water produced was assumed

to enter the production wells from the deep fracture zone. However in RS-5 and 7, water was being injected into the shallow fracture zone by SKG-2 as well being injected to the deep zone by HDR-1. Therefore it was assumed that half the produced fluid entered the wells from at 2200m and the other half entered from 1800m. In order to accommodate this assumption the model was altered for RS-5 and 7 by using it to determine pressure and temperature loss from 2200 to 1800m for half the production flow rate. This gave the pressure and temperature of flow from the deep reservoir at 1800m. These values were then averaged with the wellbore pressure and temperature outputs from the reservoir model which was used to analyse the upper reservoir for that run segment. This averaging technique caused the discontinuities in the well temperature and pressure profiles at 1800m depth for HDR-2a and HDR-3 for RS 5 and 7.

From figures 22 and 24 temperature differences for RS 5 were 31.7°C and 65.8°C for HDR-2a and HDR-3 respectively whilst pressure drop across the wells was in the order of 15.9MPa for both. Wellhead pressures and temperatures in RS 5 were thus predicted to be 1.7MPa and 238.3°C for HDR-2a and 1MPa and 204.2°C for HDR-3. Again the temperature difference between the two wellheads is due to mass flow rate with HDR-2a producing 7kg/s compared with HDR-3 which only produced 2.5kg/s. The model was altered slightly during the analysis of RS 7. The wellbore temperatures were assumed to be 20°C cooler than in the previous RS to account for reservoir cooling of as a result of cold water injection. Therefore there is an initial temperature rise in the lower sections of the wells as the water continues to pick up heat from the formation. From figures 28 and 30 Temperature differences for RS 7 were 21.8°C and 31.7°C for HDR-2a and HDR-3 respectively whilst pressure drop across the wells was in the order of 16MPa for both. Wellhead pressures and temperatures in RS 7 calculated as 1.1MPa and 228.2°C for HDR-2a and 1.2MPa and 218.3°C for HDR-3. The model predicted flow to reach the first stage slug regime in both wells during RS 5 and 7. Steam quality reached 8% and 10% for HDR-2a in RS 5 (figure 23) and RS 7 (figure 29) respectively whilst steam quality was calculated as 5.4% and 6.6% for HDR-3 in RS 5 (figure 25) and 7 (figure 30) respectively.

5.2 COMPARISON TO LITERATURE

Wellhead Pressure

Figure 32 shows the comparison of model predicted wellhead pressures with values from literature for HDR-2a during RS 1, 5 and 7. The tolerance for solution acceptance was ± 0.5 MPa from literature values and the solutions presented were within that tolerance with the largest discrepancy being 0.44MPa for RS 1. In RS 1, 5 and 7 average wellhead pressures for HDR-2a were 1MPa, 2MPa and 1MPa respectively. The model predicted

1.44MPa, 1.73MPa and 1.12MPa for RS 1, 5 and 7 respectively. The relative differences of the accepted solutions to the literature values were 43.75%, 13.59% and 11.73% for RS 1, 5 and 7 respectively. Figure 33 shows the wellhead pressure comparison for HDR-3 during each of the run segments analysed. Again each solution was within the tolerance level with the largest discrepancy being 0.24MPa and the smallest being 0.0017MPa. In RS 1, 5 and 7 average wellhead pressures for HDR-3 were all 1MPa. The model predicted 0.82MPa, 1.001MPa and 1.24MPa for RS 1, 5 and 7 respectively. The relative differences of the accepted solutions to the literature values were 17.86%, 0.17% and 23.97% for RS 1, 5 and 7 respectively.

Wellhead Temperature

Figure 34 displays the comparison of model predicted and literature values of wellhead temperature for HDR-2a throughout the run segments analysed. No tolerance was set for temperature solution acceptance and hence the difference between the model's values and the literature values is reasonably large. In RS 1,5 and 7 average wellhead temperatures for HDR-2a were 165°C, 130°C and 130°C respectively. The model predicted 250.6°C, 238.3°C and 228.3°C for RS 1, 5 and 7 respectively. The relative differences for RS 1, 5 and 7 were 51.86%, 83.33% and 75.57% respectively. The results were similar for HDR-3 although the discrepancies were not as severe as shown in figure 35. In RS 1, 5 and 7 average wellhead temperatures for HDR-2a were 180°C, 170°C and 170°C respectively. The model predicted 233.6°C, 204.1°C and 218.3°C for RS 1, 5 and 7 respectively. The relative differences for RS 1, 5 and 7 were 29.78%, 20.08% and 28.41% respectively.

The model estimated wellhead temperatures much larger than those given in literature. A possible reason for the discrepancies is that the temperature sensors at Hijiori were at times covered with scale and therefore their readings were incorrect (Tenma et al 2008). The more likely explanation for the discrepancies is that the model's assumption that wellbore temperature was the same as reservoir temperature was invalid. It was established by Cibich et al (2008) through heat transfer calculations that water requires only short flow lengths in order to heat up to reservoir temperature. However this is based on steady-state conditions. The assumption therefore fails to account for an important transient factor of geothermal reservoirs: "short circuiting" of reinjected fluid which leads to thermal breakthrough. "Short circuiting" can occur as a result of continuous reinjection. Fluid bypasses effective heat transfer area and proceeds straight to the production well thus reducing the overall temperature of the production fluid. When this occurs in an EGS it is known as thermal breakthrough. According to Tenma et al (2008) short circuiting did occur between HDR-1 and HDR-2a during the LTCT which then resulted in thermal breakthrough of that section of the reservoir (Yanagisawa et al 2008). The fact that the model failed to account for thermal breakthrough by making the wellbore temperature assumption caused the discrepancies between the predicted and literature wellhead temperature values.

Reservoir Permeability

Figure 36 shows the comparisons of model determined permeability values to values given by literature for each section of the reservoir. Like the comparisons of wellhead temperature relatively large discrepancies are apparent between the model determined values and the literature values. For the reservoir section HDR-1 to HDR-2a the model predicted an average value of $8.56 \times 10^{-16} \text{ m}^2$ whilst literature suggested $7.7 \times 10^{-15} \text{ m}^2$ which is almost ten times larger. For between HDR-1 and HDR-3 literature provided a value of $1.0 \times 10^{-15} \text{ m}^2$ whilst the model predicted an average value of $4.98 \times 10^{-16} \text{ m}^2$ which is less than half the literature permeability. Whilst the deep reservoir permeability predictions were under estimated the shallow reservoir permeability predictions were over estimated. For between SKG-2 and HDR-2a the model returned an average value of $8.73 \times 10^{-16} \text{ m}^2$ whereas literature gave a value of $1.0 \times 10^{-16} \text{ m}^2$; one eighth of the predicted value. For between SKG-2 and HDR-3 literature again provided a value of $1.0 \times 10^{-16} \text{ m}^2$ whereas the model predicted $6.69 \times 10^{-16} \text{ m}^2$; nearly seven times larger than the value from literature. There are some plausible justifications for these massive discrepancies. As mentioned in section 3 the literature data were taken from a study based on the 1995 and 1996 short-term circulation tests making the comparison indirect. Additionally the model assumed that reservoir flow was split evenly between the deep and shallow reservoirs. According to Tenma et al (2008), most of the reservoir flow was in the deep reservoir, particularly in the section between HDR-1 and HDR-2a, which fits in with the thermal breakthrough that occurred in that section. Had the correct flow rates been used as inputs for the model then the discrepancies may not have been so large.

5.3 RESERVOIR CHARACTERISTICS

Flow Impedance

Figure 37 shows the flow impedance values for the four reservoir sections for each run segment as determined by the model in units of MPa/l/s. According to the model every reservoir section experienced an increase in flow impedance over the LTCT except for the section between HDR-1 and HDR-2 which experienced a decrease in flow impedance. This result is in agreement with the literature as it suggests that the fracture zone between HDR-1 and HDR-2a was able to handle more flow for less pressure drop toward the end of the LTCT compared with the other reservoir sections.

Total Reservoir Permeability

The values of total permeability for each reservoir section during RS 1, 5 and 7 are displayed in figure 38. Again according to the model the permeability of every reservoir section besides the section between HDR-1 and

HDR2a decreased over the LTCT. The permeability of the fracture zone between HDR-1 and HDR-2a actually increased over the time of the LTCT according to the results of the analysis. This again implies that flow dominated that particular section of the reservoir during the latter part of the LTCT, which is in line with the literature.

Absolute Skin Factor

The values of absolute skin factor for each reservoir section during RS 1, 5 and 7 are shown in figure 39. The fractures in the analysis were assumed symmetrical so skin factors cancelled out and had no effect in terms of total pressure drop. The results for skin factor have no comparative value in terms literature but were presented for the purposes of demonstrating the impact that inertial effects have on pressure drop at injection and production wellbores. For example at the HDR-1 production wellbore during RS 1 with a skin factor of 2.9, pressure drop has an additional amount of $2.9\mu q/k\theta h = 2.8MPa$ if inertial effects were not included as part of the radial flow pressure drop equation.

5.4 OVERALL PERFORMANCE OF THE MODEL AND RECOMMENDATIONS

When considering the results obtained and in the comparisons between them and field data the overall performance of the model could be viewed as encouraging but with room for further improvement. The well profiles produced provided insight into flow pressure, temperature and steam quality changes during geothermal well flow whilst skin values offered a view of how inertial effects impact on radial flow pressure drop. With respect to comparing the model to data from literature the values of wellhead pressure determined by the model were within the tolerance and in the case of HDR-3 RS 5 almost exact. However the tolerance level set for the analysis could be considered too large. The analysis was being performed using crudely constructed spreadsheet in Microsoft Excel® as not enough time was available to implement the model properly. Although Excel® could have been used more effectively, the models implementation in a more power program such as MATLAB® would have allowed for a tighter tolerance to be set. The wellhead temperature estimations were not accurate due to the model not accounting for “short circuiting” resulting in thermal breakthrough whilst reservoir permeability predictions also showed large discrepancies. On the other hand the results of flow impedance and total permeability were in agreement with the literature in that they suggested the fracture zone the region between HDR-1 and HDR-2a handled most of the flow particularly during the latter part of the LTCT.

In hindsight the discrepancies of the results produced by the model could have been due to the method used to implement it. It was realised too late in the research process that the model would have performed better had an alternative method been used to one described in section 3. The method used at step 3 was to estimate fracture aperture to determined reservoir pressure drop and hence production wellbore and wellhead pressure. Rather the well flow model, using wellhead pressures and temperatures given in literature as inputs to the first increment, should have been utilized to provide wellbore pressures and temperatures for the production wells. The next step of this alternative procedure would be to determined reservoir pressure drop simply by subtracting the wellbore pressure on the production side from the wellbore pressure on the injection side determined in step 1 (in the alternative method steps 1 and 2 would have remained the same). Reservoir permeability would then have been determined from the reservoir pressure drop. The model's primary function then should have been to determine reservoir characteristics.

With respect to meeting the project aim the results have proved that the model can provide a basic idea to pressure and temperature modelling of EGS and can provide approximations of reservoir characteristics. Well profiles in pressure, temperature and quality were produced for three out of the seven run segments along with estimations of production wellhead pressure and temperature. Estimations of flow impedance, permeability and skin factors were also acquired. Comparisons were made of the results and the Hijiori field data from the LTCT.

Despite discrepancies in the comparative results and perhaps not the most effective method being adopted to implement it, the model has encouraging amounts of potential and is more sophisticated than it was in its original form. It is recommended that the model be cross checked further with additional case studies and comparison to other geothermal models. The Hijiori analysis could be repeated using the alternative method described above and the model could also be implemented into a more powerful code such as MATLAB®. However of more importance is more testing of the model against other field data and EGS models.

6 CONCLUSIONS

The development of an analytical model for Enhanced Geothermal Systems was continued from work previously undertaken by the author in December 2007 to February 2008 on behalf of the Petroleum and Geothermal Group of PIRSA. The model has provided a basic understanding of pressure and temperature modelling in EGS and is able to gauge reservoir characteristics of EGS. The model has been applied to data from the Hijiori LTCT and the following conclusions have been made.

- The model produced profiles of temperature, pressure and steam quality profiles for wells HDR-1, SKG-2, HDR-2a and HDR-3 in RS 1, 5 and 7 of the LTCT. Pressure gradient was found to be predominately linear in the injection wells where single phase flow dominated. Pressure gradient was found to become less severe in the upper sections of the production wells due to flow regime changes and hence density changes. Temperature gradients were positive parabolic for injection and negative parabolic for production. Discontinuities in production well temperature profiles were caused by averaging techniques whilst higher temperature differences were the result of lower mass flow rates. Steam quality ranged from 0 to 14%.
- Wellhead pressures were estimated for the Hijiori production wells HDR-2a and HDR-3 during RS 1, 5 and 7 and all were within the 0.5MPa tolerance. For RS 1, 5 and 7 the relative differences of the results from literature for HDR-2a were 43.75%, 13.59% and 11.73% respectively and for HDR-3 they were 17.86%, 0.17% and 23.97% respectively.
- Wellhead temperatures were estimated for the Hijiori production wells HDR-2a and HDR-3 during RS 1, 5 and 7. For RS 1, 5 and 7 the relative differences of the results from literature for HDR-2a were 51.86%, 83.33% and 75.57% respectively and for HDR-3 they were 29.78%, 20.08% and 28.40% respectively. Large discrepancies were due to the model's assumption that wellbore temperatures were equal to reservoir temperatures which did not account for thermal breakthrough that occurred at Hijiori.
- Reservoir permeability was estimated and the results were not in total agreement with literature. This was due to assuming even flow between each section of the reservoir and not using directly comparative literature data.
- Reservoir characteristics of flow impedance and total permeability showed the section of the reservoir most accessible to flow was between HDR-1 and HDR-2a which agreed with literature. The skin factors were not totally relevant but demonstrated the impact inertial effects have on radial flow pressure drop.
- The overall performance was viewed as encouraging but further development is required. It was recommended the model be implemented in a more powerful code such as MATLAB® and that using an alternative method to apply the model would produce better results.

7 NOMENCLATURE

Letter	Meaning	Units
A	Area	m^2
c_p	Heat capacity	J/kg.K
D	Distance between wells at fracture depth	m
d_w	Well diameter	m
f	Moody friction factor	
f_l	Louis friction factor	
f(t)	Transient Heat Conduction function	
g	Gravitational acceleration	m/s^2
H	Reservoir Length in vertical direction	m
h	Fracture aperture, enthalpy	m, kJ/kg
k	Permeability	m^2
L	Length of linear flow	M
$L_{b/s}$	Bubble/slug boundary term	
$L_{s/t}$	Slug/transition boundary term	
$L_{t/m}$	Transition/mist boundary term	
δL	Area correction length	m
m	Mass flow rate	kg/s
N_{GV}	Gas velocity number	
N_{LV}	Liquid velocity number	
N_p	Slug stage flow determination parameter	
n	Number of fractures	
P	Pressure	Pa
Q	Heat loss	W
q	Volumetric flow rate	m^3/s
Re	Reynolds Number	
Re_b	Prevailing bubble Reynolds number	
r	Radius	m
S	Skin Factor	
T	Temperature	$^{\circ}C$
t	Time	Days
U_{ci}	Overall heat transfer coefficient	$W/m^2.K$
u_b	Bubble rise number	m/s
v_b	Nicklin bubble rise velocity	m/s
v_s	Superficial velocity	m/s
v_{slip}	Slip velocity	m/s
w	Fracture width	m
x	Vapour mass fraction or quality	
Z	Vertical Displacement	m

Greek Letter	Meaning	Units
α	Thermal diffusivity of the earth	m^2/s
Δ	Change in	
ε	roughness	m
Γ	Liquid distribution coefficient	
γ_a	Acceleration gradient	
η_G	Vapour volume fraction	
λ	Thermal conductivity	W/m.K
μ	Viscosity	Pa.s
ρ	Density	kg/m^3
θ	Angle of radial flow	Radian
τ_f	Friction gradient	Pa/m
ω	Surface tension	N/m
Subscripts	Meaning	
c	Critical	
ci	Inner casing	
co	Inner casing	
e	Effective/external/formation	
G	Vapour	
h	Cement/formation	
i	Injection	
L	Liquid	
lin	Linear	
M	Mixture	
o	Overall	
p	Production	
rad	radial	
T	Total (for well flow model)	
total	Total (for well flow model)	
w	Well	

8 REFERENCES

- Chadha, P.K., Malin, M.R. and Palacio-Perez, A., *“Modelling of Two-Phase Flow Inside Geothermal Wells”*, Applied Mathematical Modelling, 17, 236 – 245, 1993.
- Chierici, G.L., Ciucci, G.M. and Sclocchi, G., *“Two-Phase Vertical Flow in Oil Wells – Prediction of Pressure Drop”*, Journal of Petroleum Technology, AIME, 257, 927 – 938, 1974.
- Cibich, W.H., Malavazos, M., and McDonough, R. *“A Steady-State Pressure Model for Water Flow in a Hydraulically Fractured Geothermal Reservoir”*, in: Gurgenci and Budd (editors), Proceedings of the Sir Mark Oliphant International Frontiers of Science and Technology Australian Geothermal Energy Conference, Geoscience Australia, Record 2008/18, 43 – 50.
- Duns, H. Jr. and Ros, N.C.J., *“Vertical Flow of Gas and Liquid Mixtures in Wells”*, Proceedings of the Sixth World Petroleum Congress in Frankfurt, Section II, Paper 22 PD6, 451 – 465, 1961.
- Goldstein, B. A., Hill, A.J., Budd, A.R., Holgate, F.L., and Malavazos, M., *“The National Outlook – Australia’s Hot Rocks”*, in: Gurgenci and Budd (editors), Proceedings of the Sir Mark Oliphant International Frontiers of Science and Technology Australian Geothermal Energy Conference, Geoscience Australia, Record 2008/18, 9 – 17.
- Gould, T.L., Tek, M.R. and Katz, D.L., *“Two-Phase Flow Through Vertical, Inclined, or Curved Pipe”*, Journal of Petroleum Technology, AIME, 257, 915 – 926, 1974.
- Griffith, P. and Wallis, G.B., *“Two-Phase Slug Flow”*, Journal of Heat Transfer, 307 – 320, August 1961.
- Grove-White, G., *“Geodynamics Ltd: Quarterly Report, period ending 30 June 2008”*, Geodynamics Ltd, 2008.
- Jackson, J.D. and Symmons, G.R., *“An investigation of Laminar Radial Flow Between Two Parallel Discs”*, Applied Science Research, 15, 59 – 75, 1965.
- Jones, T.A., Wooten, S.O. and Kaluza, T.J., *“Single-Phase Flow Through Natural Fractures”*, Society of Petroleum Engineers Annual Technical Conference and Exhibition, Paper Number: 18175-MS, October 2 – 5 1988.
- Livesey, J.L., *“Inertia Effects in Viscous Flows”*, International Journal of Mechanical Science, 1, 84 – 88, 1960.
- Louis, G.M., *“A Study of Groundwater in Jointed Rocks and Its Influence on the Stability of Rock Masses”*, Rock Mechanics Research, Rep. 10, 90pp, Imp. Coll., London, 1969.

Morita, K., Tago, M. and Ehara, S., *“Case Studies on Small-Scale Power Generation with the Downhole Coaxial Heat Exchanger”*, Proceedings World Geothermal Congress, Antalya, Turkey, 24 – 29 April 2005.

Murphy, H.D., Coxon, M., McEligot, D.M., *“Symmetric Sink Flow Between Parallel Plates”*, Journal of Fluids Engineering, 100, 477 – 484, 1979.

Orkiszewski, J., *“Predicting Two-Phase Flow Pressure Drops in Vertical Pipe”*, Journal of Petroleum Technology, AIME, 240, 829 – 838, 1967.

Paivanas, J.A. and Hassan, J.K., *“Attraction Force Characteristics Engendered by Bounded, Radially Diverging Air Flow”*, IBM Journal of Research and Development, 25, No.3, 176 – 186, 1981.

Slider, H.C., *“Worldwide Practical Petroleum Reservoir Engineering Methods”*, Pennwell Publishing Company, 2, 39 – 52, 1983.

Tenma, N., Yamaguchi, T. and Zvoloski, G., *“The Hijiori Hot Dry Rock Test Site, Japan. Evaluation and Optimization of Heat Extraction from a Two-Layered Reservoir”*, Geothermics, 37, 19 – 52, 2008.

Tester, J.W., *“The Future of Geothermal Energy as a Major Global Energy Supplier”*, in: Gurgenci and Budd (editors), Proceedings of the Sir Mark Oliphant International Frontiers of Science and Technology Australian Geothermal Energy Conference, Geoscience Australia, Record 2008/18, 19 – 21.

Tester and 11 others, *“The Future of Geothermal Energy. Impact of Enhanced Geothermal Systems (EGS) on the United States in the 21st Century”*, Massachusetts Institute of Technology, 2006.

Willhite, G.P., *“Over-all Heat Transfer Coefficients in Steam and Hot Water Injection Wells”*, Journal of Petroleum Technology, 607 – 615, May 1967.

Yamaguchi, S., Akibayashi, S., Rokugawa, S., Fujinaga, Y., Tenma, N. and Sato, Y., *“The Numerical Modelling Study of the Hijiori HDR Test Site”*, Proceedings World Geothermal Congress, 3975 - 3980, Kyushu-Tohoku, Japan, May 28 – June 10, 2000.

Yanagisawa, N., Matsunaga, I., Sugita, H., Sato, M. and Okabe, T., *“Temperature-dependent scale precipitation in the Hijiori Hot Dry Rock system, Japan”*, Geothermics, 37, 1 -18, 2008.

9 APPENDICES

9.1 DATA FROM HIJIORI LTCT (TENMA ET AL 2008)

Mass Flow Rates

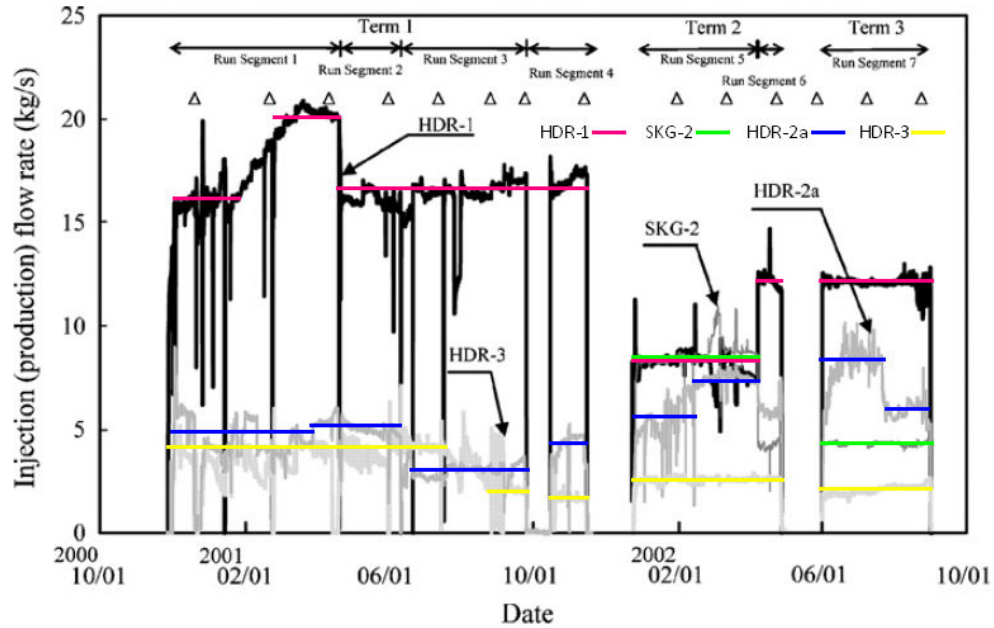


Figure 40 Mass flow rate data for each well during the Hijiori LTCT (Tenma et al 2008).

Wellhead Pressures

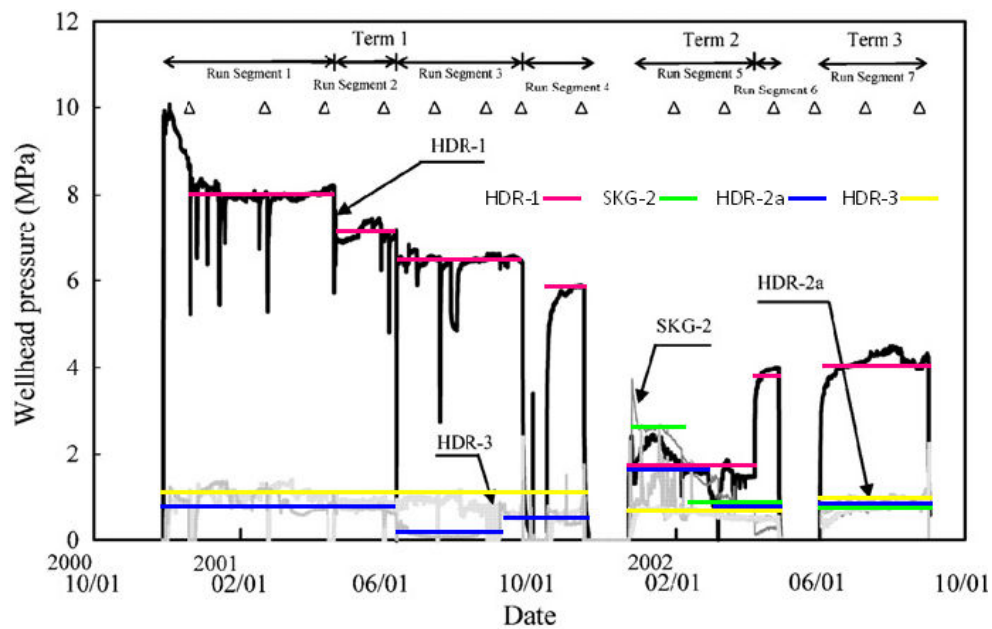


Figure 41 Average wellhead pressure data for each well during the Hijiori LTCT (Tenma et al 2008).

Wellhead Temperatures

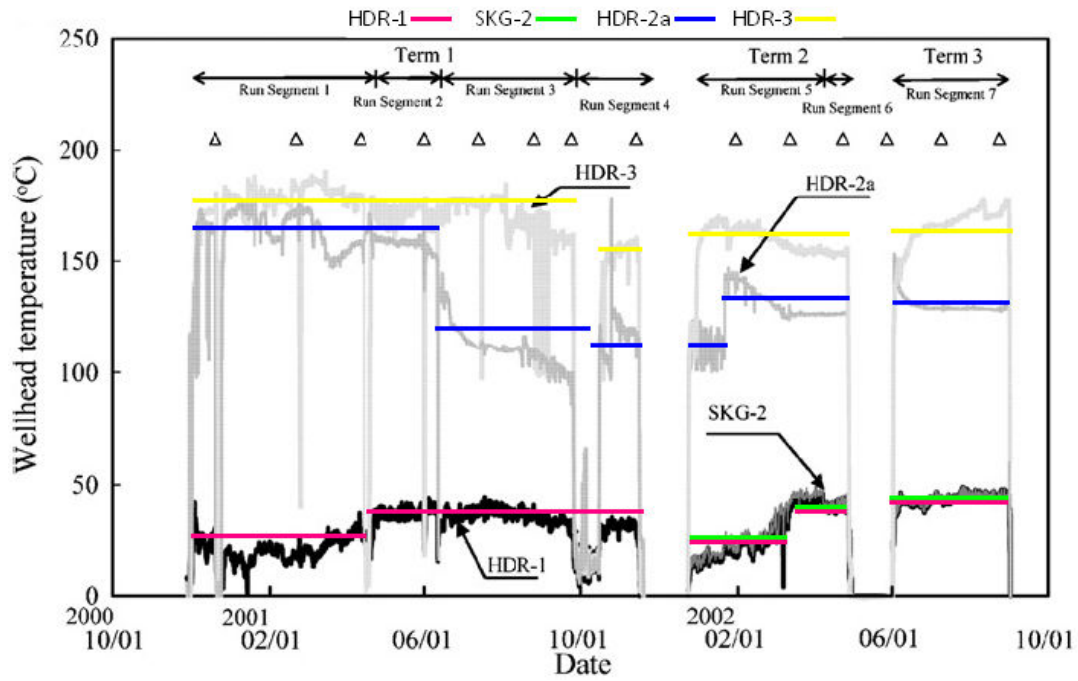


Figure 42 Average wellhead temperature data for each well during the Hijiori LTCT (Tenma et al 2008).

Tenma et al Model Schematic

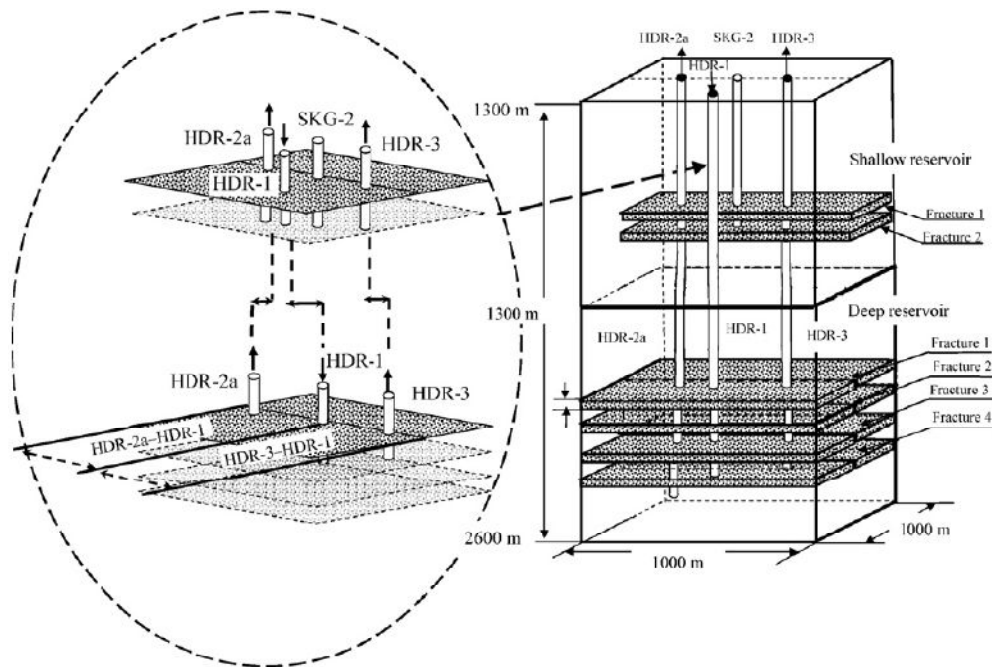


Figure 43 Schematic used to describe the reservoir model developed by Tenma et al (2008) for their Hijiori model FEHM.

9.2 CASING PROFILES

HDR-1

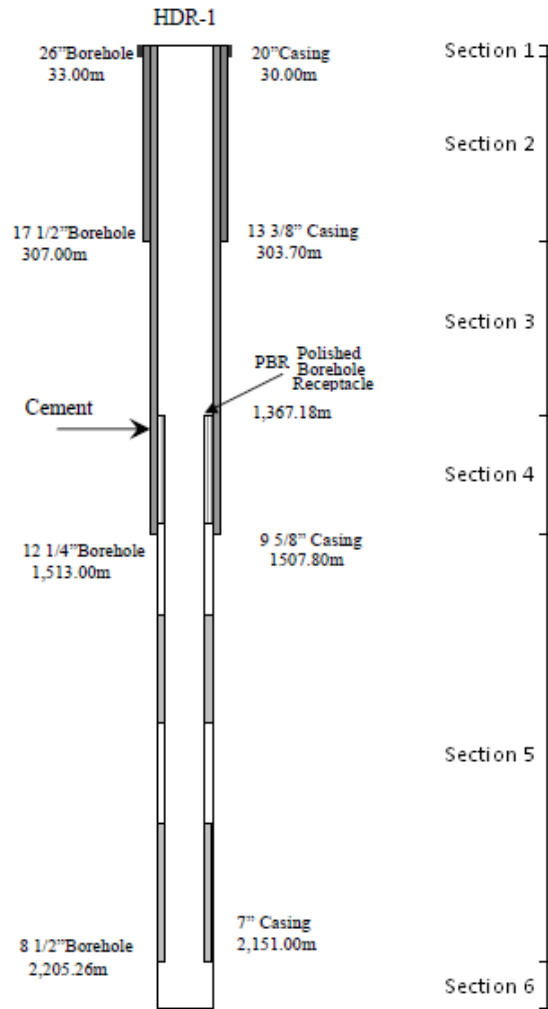


Figure 44 Casing profile for HDR-1 provided by Norio Tenma.

Table VI HDR-1 casing dimensions in SI units.

Radius (m)	Section 1 (0 - 30m)	Section 2 30 - 307m)	Section 3 (307 - 1367m)	Section 4 (1367 - 1513m)	Section 5 (1513 - 2151m)	Section 6 (2151 - 2200m)
Inner Casing 1	0.10795	0.10795	0.10795	0.079705	0.079705	Open Wellbore
Outer Casing 1	0.1222375	0.122238	0.1222375	0.0889	0.0889	
Inner Casing 2	0.155575	0.155575	-	0.10795	-	
Outer Casing 2	0.1698625	0.169863	-	0.122238	-	
Inner Casing 3	0.22225	-	-	-	-	
Outer Casing 3	0.254	-	-	-	-	
Cement/Formation Interface	0.3302	0.22225	0.155575	0.155575	0.10795	

SKG-2

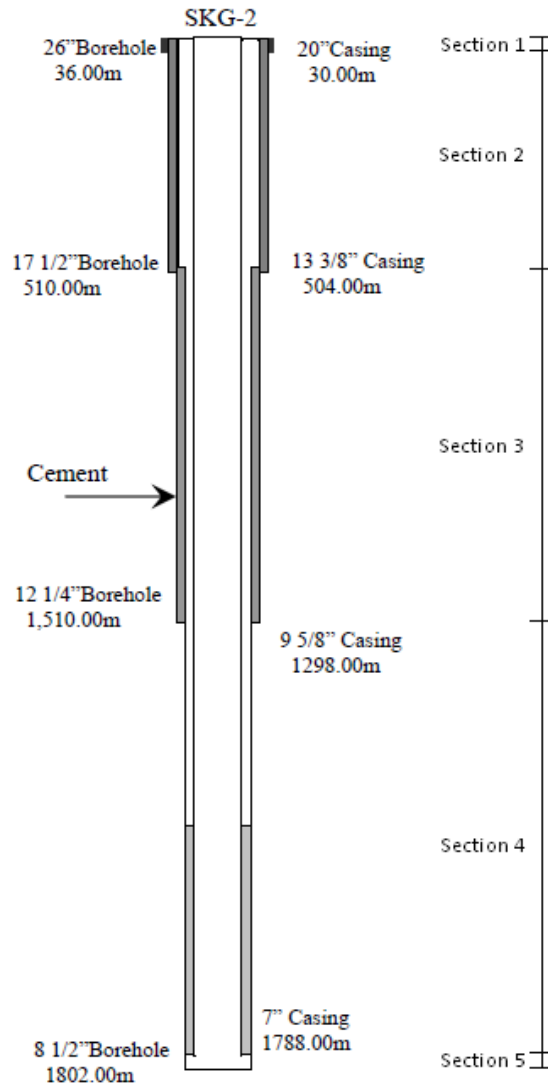


Figure 45 Casing profile for SKG-2 provided by Norio Tenma.

Table VII SKG-2 casing dimensions in SI units.

Radius (m)	Section 1 (0 - 30m)	Section 2 (30 - 510m)	Section 3 (510 - 1510m)	Section 4 (1510 - 1788m)	Section 5 (1788 - 1800m)
Inner Casing 1	0.079705	0.079705	0.079705	0.079705	Open Wellbore
Outer Casing 1	0.0889	0.0889	0.0889	0.0889	
Inner Casing 2	0.155575	0.155575	0.10795	-	
Outer Casing 2	0.1698625	0.169863	0.1222375	-	
Inner Casing 3	0.22225	-	-	-	
Outer Casing 3	0.254	-	-	-	
Cement/Formation Interface	0.3302	0.22225	0.155575	0.10795	

HDR-2a

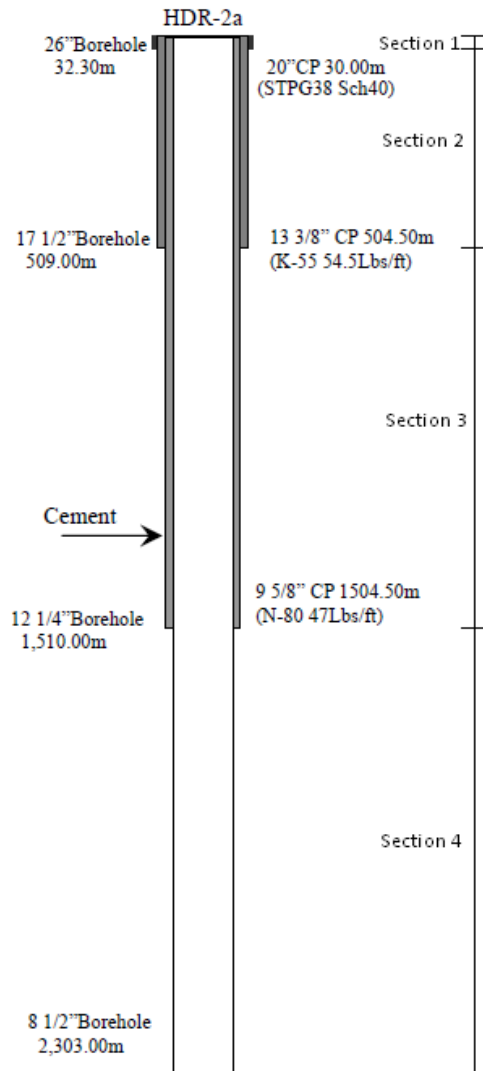


Figure 46 Casing profile for HDR-2a provided by Norio Tenma.

Table VIII HDR-2a casing dimensions in SI units.

Radius (m)	Section 1 (0 - 32.5m)	Section 2 (32.5 - 509m)	Section 3 (509 - 1509m)	Section 4 (1509 - 2303m)
Inner Casing 1	0.10795	0.10795	0.10795	Open Wellbore
Outer Casing 1	0.1222375	0.1222375	0.1222375	
Inner Casing 2	0.155575	0.155575	-	
Outer Casing 2	0.1698625	0.1698625	-	
Inner Casing 3	0.22225	-	-	
Outer Casing 3	0.254	-	-	
Cement/Formation Interface	0.3302	0.22225	0.155575	

HDR-3

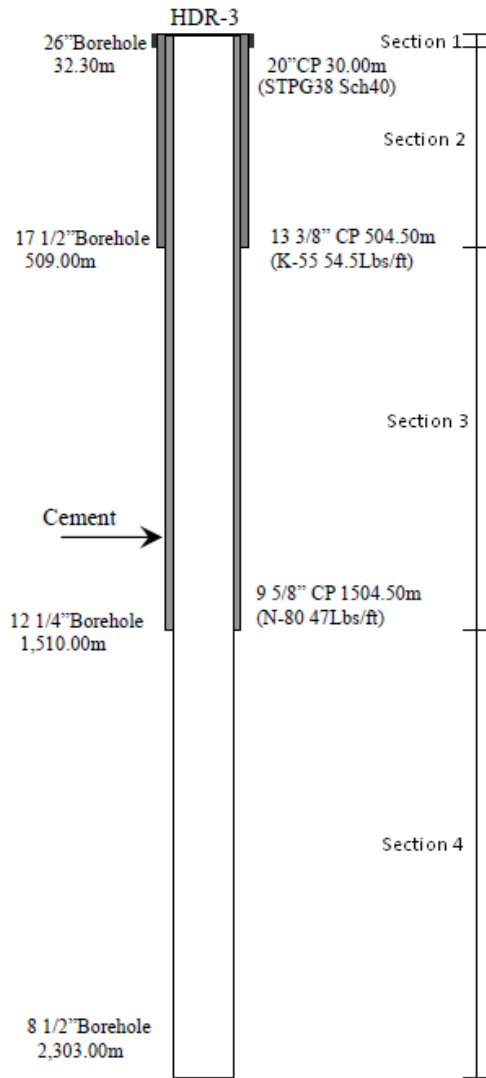


Figure 47 Casing profile for HDR-3 provided by Norio Tenma.

Table IX HDR-3 casing dimensions in SI units.

Radius (m)	Section 1 (0 - 32.5m)	Section 2 (32.5 - 509m)	Section 3 (509 - 1509m)	Section 4 (1510 - 2303m)
Inner Casing 1	0.10795	0.10795	0.10795	Open Wellbore
Outer Casing 1	0.1222375	0.1222375	0.1222375	
Inner Casing 2	0.155575	0.155575	-	
Outer Casing 2	0.1698625	0.1698625	-	
Inner Casing 3	0.22225	-	-	
Outer Casing 3	0.254	-	-	
Cement/Formation Interface	0.3302	0.22225	0.155575	

9.3 RESERVOIR MODEL DATA FOR LTCT

Term 1 – Run Segment 1

Table X Reservoir model data from HDR-1 to HDR-2a for run segment 1 of the Hijiori HDR project.

Reservoir Model (Deep Reservoir HDR-1 to HDR-2a) Run Segment 1			
Parameter	Symbol	Value	Unit
Reservoir Depth	Z	2200	m
Distance between wells	D	90	m
Fracture Width	w	45	m
Angle of radial flow	θ	1.570796327	rad
Aperture	h	0.00017	m
Flow rate through fracture	m	7	kg/s
Reservoir temperature	T_R	270	C
Well radius at HDR-1	r_{wi}	0.10795	m
Well radius at HDR-2a	r_{wp}	0.10795	m
Reservoir Vertical Length	H	200	m
Number of Fractures	n	4	none
External radius at HDR-1	r_{ei}	31.81980515	m
External radius at HDR-2a	r_{ep}	31.81980515	m
Length of Linear Flow	L	26.36038969	m
Roughness	ε	0.000113333	m
Louis Friction Factor	f_l	2.687426267	none
Effective Permeability	k_e	8.96149×10^{-10}	m^2
Effective Permeability (in Darcy's)	k_e	907.0605557	Darcy's
Total reservoir permeability	k_{etotal}	7.17132×10^{-16}	m^2
Converging Skin Factor	S	2.900154701	none
Diverging Skin Factor	S	-2.900154701	none
Area of flow	A	5727.564928	m^2
Area Correction Radius (if no linear flow length)	A_{cr}	35.90480524	m
Area Correction Length	δL	5.796692954	m
Water Density	ρ	797.6081475	kg/m^3
Water Viscosity	μ	0.000104263	Pa.s
Volumetric Flow Rate Through Fracture	q_f	0.00219406	m^3/s
Linear Reynolds	Re	745.9787349	none
Overall Reynolds	Re_o	62855048.7	none
Radial Pressure drop at production	ΔP_{radp}	8207980.672	Pa
Linear Pressure Drop	ΔP_{lin}	1888433.752	Pa
Radial Pressure drop at injection	Δp_{radi}	2663257.437	Pa
Total Pressure Drop	ΔP	12759671.86	Pa
Total Pressure Drop in MPa	ΔP	12.75967186	MPa

Table XI Reservoir model data from HDR-1 to HDR-3 for run segment 1 of the Hijiori HDR project.

Reservoir Model (Deep Reservoir HDR-1 to HDR-3) Run Segment 1			
Parameter	Symbol	Value	Unit
Reservoir Depth	Z	2200	m
Distance between wells	D	130	m
Fracture Width	w	65	m
Angle of radial flow	θ	1.570796327	rad
Aperture	h	0.000186	m
Flow rate through fracture	m	6.8	kg/s
Reservoir temperature	T_R	270	C
Well radius at HDR-1	r_{wi}	0.10795	m
Well radius at HDR-3	r_{wp}	0.10795	m
Reservoir Vertical Length	H	200	m
Number of Fractures	n	3	none
External radius at HDR-1	r_{ei}	45.96194078	m
External radius at HDR-3	r_{ep}	45.96194078	m
Length of Linear Flow	L	38.07611845	m
Roughness	ε	0.000124	m
Louis Friction Factor	f_l	2.687426267	none
Effective Permeability	k_e	1.07277×10^{-9}	m^2
Effective Permeability (in Darcy's)	k_e	1085.836228	Darcy's
Total reservoir permeability	k_{etotal}	6.98482×10^{-16}	m^2
Converging Skin Factor	S	4.10995815	none
Diverging Skin Factor	S	-4.10995815	none
Area of flow	A	11950.1046	m^2
Area Correction Radius (if no linear flow length)	A_{cr}	51.86249645	m
Area Correction Length	δL	8.373000933	m
Water Density	ρ	797.6081475	kg/m^3
Water Viscosity	μ	0.000104263	Pa.s
Volumetric Flow Rate Through Fracture	q_f	0.00284183	m^3/s
Linear Reynolds	Re	668.9215908	none
Overall Reynolds	Re_o	74409048.94	none
Radial Pressure drop at production	ΔP_{radp}	9608263.02	Pa
Linear Pressure Drop	ΔP_{lin}	1867494.342	Pa
Radial Pressure drop at injection	Δp_{radi}	1837679.21	Pa
Total Pressure Drop	ΔP	13313436.57	Pa
Total Pressure Drop in MPa	ΔP	13.31343657	MPa

Term 2 – Run Segment 5

Table XII Reservoir model data from SKG-2 to HDR-2 for run segment 5 of the Hijiori HDR project.

Fracture Model (Shallow Reservoir SKG-2 to HDR-2) Run Segment 5			
Parameter	Symbol	Value	Unit
Reservoir Depth	Z	1800	m
Distance between wells	D	50	m
Fracture Width	w	25	m
Angle of radial flow	θ	1.570796327	rad
Aperture	h	0.00024	m
Flow rate through fracture	m	3.8375	kg/s
Reservoir temperature	T_R	250	C
Well radius at SKG-2	r_{wi}	0.10795	m
Well radius at HDR-2	r_{wp}	0.10795	m
Reservoir Vertical Length	H	200	m
Number of Fractures	n	2	none
External radius at SKG-2	r_{ei}	17.67766953	m
External radius at HDR-2	r_{ep}	17.67766953	m
Length of Linear Flow	L	14.64466094	m
Roughness	ε	0.00016	m
Louis Friction Factor	f_l	2.687426267	none
Effective Permeability	k_e	1.7861×10^{-9}	m^2
Effective Permeability (in Darcy's)	k_e	1807.843876	Darcy's
Total reservoir permeability	k_{etotal}	1.10636×10^{-15}	m^2
Converging Skin Factor	S	4.23344031	none
Diverging Skin Factor	S	-4.23344031	none
Area of flow	A	1767.766953	m^2
Area Correction Radius (if no linear flow length)	A_{cr}	19.94711402	m
Area Correction Length	δL	3.220384974	m
Water Density	ρ	816.7454862	kg/m^3
Water Viscosity	μ	0.000110558	Pa.s
Volumetric Flow Rate Through Fracture	q_f	0.002349263	m^3/s
Linear Reynolds	Re	1388.417583	none
Overall Reynolds	Re_o	46036150.3	none
Radial Pressure drop at production	ΔP_{radp}	3599572.533	Pa
Linear Pressure Drop	ΔP_{lin}	762003.8531	Pa
Radial Pressure drop at injection	Δp_{radi}	333637.3403	Pa
Total Pressure Drop	ΔP	4695213.726	Pa
Total Pressure Drop in MPa	ΔP	4.695213726	MPa

Table XIII Reservoir model data from SKG-2 to HDR-3 for run segment 5 of the Hijiori HDR project.

Fracture Model (Shallow Reservoir SKG-2 to HDR-3) Run Segment 5			
Parameter	Symbol	Value	Unit
Reservoir Depth	Z	1800	m
Distance between wells	D	55	m
Fracture Width	w	27.5	m
Angle of radial flow	θ	1.570796327	rad
Aperture	h	0.00022	m
Flow rate through fracture	m	2.7125	kg/s
Reservoir temperature	T_R	250	C
Well radius at SKG-2	r_{wi}	0.10795	m
Well radius at HDR-3	r_{wp}	0.10795	m
Reservoir Vertical Length	H	200	m
Number of Fractures	n	2	none
External radius at SKG-2	r_{ei}	19.44543648	m
External radius at HDR-3	r_{ep}	19.44543648	m
Length of Linear Flow	L	16.10912703	m
Roughness	ε	0.000146667	m
Louis Friction Factor	f_l	2.687426267	none
Effective Permeability	k_e	1.50082×10^{-9}	m^2
Effective Permeability (in Darcy's)	k_e	1519.091035	Darcy's
Total reservoir permeability	k_{etotal}	8.39038×10^{-16}	m^2
Converging Skin Factor	S	2.795688264	none
Diverging Skin Factor	S	-2.795688264	none
Area of flow	A	2138.998013	m^2
Area Correction Radius (if no linear flow length)	A_{cr}	21.94182542	m
Area Correction Length	δL	3.542423472	m
Water Density	ρ	808.5141692	kg/m^3
Water Viscosity	μ	0.000108475	Pa.s
Volumetric Flow Rate Through Fracture	q_f	0.00167746	m^3/s
Linear Reynolds	Re	909.302683	none
Overall Reynolds	Re_o	36180004.19	none
Radial Pressure drop at production	ΔP_{radp}	2803006.357	Pa
Linear Pressure Drop	ΔP_{lin}	693080.4072	Pa
Radial Pressure drop at injection	Δp_{radi}	841321.1386	Pa
Total Pressure Drop	ΔP	4337407.903	Pa
Total Pressure Drop in MPa	ΔP	4.337407903	MPa

Table XIV Reservoir model data from HDR-1 to HDR-2a for run segment 5 of the Hijiori HDR project.

Fracture Model (Deep Reservoir HDR-1 to HDR-2a) Run Segment 5			
Parameter	Symbol	Value	Unit
Reservoir Depth	Z	2200	m
Distance between wells	D	90	m
Fracture Width	w	45	m
Angle of radial flow	θ	1.570796327	rad
Aperture	h	0.00018	m
Flow rate through fracture	m	3.8375	kg/s
Reservoir temperature	T_R	270	C
Well radius at HDR-1	r_{wi}	0.10795	m
Well radius at HDR-2a	r_{wp}	0.10795	m
Reservoir Vertical Length	H	200	m
Number of Fractures	n	4	none
External radius at HDR-1	r_{ei}	31.81980515	m
External radius at HDR-2a	r_{ep}	31.81980515	m
Length of Linear Flow	L	26.36038969	m
Roughness	ε	0.00012	m
Louis Friction Factor	f_l	2.687426267	none
Effective Permeability	k_e	1.00468×10^{-9}	m^2
Effective Permeability (in Darcy's)	k_e	1016.91218	Darcy's
Total reservoir permeability	k_{etotal}	8.51275×10^{-16}	m^2
Converging Skin Factor	S	1.709866069	none
Diverging Skin Factor	S	-1.709866069	none
Area of flow	A	5727.564928	m^2
Area Correction Radius (if no linear flow length)	A_{cr}	35.90480524	m
Area Correction Length	δL	5.796692954	m
Water Density	ρ	790.6824951	kg/m^3
Water Viscosity	μ	0.000102651	Pa.s
Volumetric Flow Rate Through Fracture	q_f	0.00121335	m^3/s
Linear Reynolds	Re	415.3782891	none
Overall Reynolds	Re_o	33054753.98	none
Radial Pressure drop at production	ΔP_{radp}	3242859.586	Pa
Linear Pressure Drop	ΔP_{lin}	866167.355	Pa
Radial Pressure drop at injection	Δp_{radi}	1743448.008	Pa
Total Pressure Drop	ΔP	5852474.949	Pa
Total Pressure Drop in MPa	ΔP	5.852474949	MPa

Table XV Reservoir data from HDR-1 to HDR-3 for run segment 5 of the Hijiori HDR project.

Fracture Model (Deep Reservoir HDR-1 to HDR-3) Run Segment 5			
Parameter	Symbol	Value	Unit
Reservoir Depth	Z	2200	m
Distance between wells	D	130	m
Fracture Width	w	65	m
Angle of radial flow	θ	1.570796327	rad
Aperture	h	0.0001565	m
Flow rate through fracture	m	2	kg/s
Reservoir temperature	T_R	270	C
Well radius at HDR-1	r_{wi}	0.10795	m
Well radius at HDR-3	r_{wp}	0.10795	m
Reservoir Vertical Length	H	200	m
Number of Fractures	n	3	none
External radius at HDR-1	r_{ei}	45.96194078	m
External radius at HDR-3	r_{ep}	45.96194078	m
Length of Linear Flow	L	38.07611845	m
Roughness	ε	0.000104333	m
Louis Friction Factor	f_l	2.687426267	none
Effective Permeability	k_e	7.5947×10^{-10}	m^2
Effective Permeability (in Darcy's)	k_e	768.7181279	Darcy's
Total reservoir permeability	k_{etotal}	3.97706×10^{-16}	m^2
Converging Skin Factor	S	1.033063167	none
Diverging Skin Factor	S	-1.033063167	none
Area of flow	A	11950.1046	m^2
Area Correction Radius (if no linear flow length)	A_{cr}	51.86249645	m
Area Correction Length	δL	8.373000933	m
Water Density	ρ	790.6824951	kg/m^3
Water Viscosity	μ	0.000102651	Pa.s
Volumetric Flow Rate Through Fracture	q_f	0.000843153	m^3/s
Linear Reynolds	Re	199.831199	none
Overall Reynolds	Re_o	26418760.4	none
Radial Pressure drop at production	ΔP_{radp}	3285366.531	Pa
Linear Pressure Drop	ΔP_{lin}	915791.5775	Pa
Radial Pressure drop at injection	Δp_{radi}	2327554.083	Pa
Total Pressure Drop	ΔP	6528712.192	Pa
Total Pressure Drop in MPa	ΔP	6.528712192	MPa

Term 3 - Run Segment 7

Table XVI Reservoir data from SKG-2 to HDR-2 for run segment 7 of the Hijiori HDR project.

Fracture Model (Shallow Reservoir SKG-2 to HDR-2) Run Segment 7			
Parameter	Symbol	Value	Unit
Reservoir Depth	Z	1800	m
Distance between wells	D	50	m
Fracture Width	w	25	m
Angle of radial flow	θ	1.570796327	rad
Aperture	h	0.0002	m
Flow rate through fracture	m	2	kg/s
Reservoir temperature	T_R	230	C
Well radius at SKG-2	r_{wi}	0.10795	m
Well radius at HDR-2	r_{wp}	0.10795	m
Reservoir Vertical Length	H	200	m
Number of Fractures	n	2	none
External radius at SKG-2	r_{ei}	17.67766953	m
External radius at HDR-2	r_{ep}	17.67766953	m
Length of Linear Flow	L	14.64466094	m
Roughness	ε	0.000133333	m
Louis Friction Factor	f_l	2.687426267	none
Effective Permeability	k_e	1.24034×10^{-9}	m^2
Effective Permeability (in Darcy's)	k_e	1255.447136	Darcy's
Total reservoir permeability	k_{etotal}	6.4025×10^{-16}	m^2
Converging Skin Factor	S	1.691170051	none
Diverging Skin Factor	S	-1.691170051	none
Area of flow	A	1767.766953	m^2
Area Correction Radius (if no linear flow length)	A_{cr}	19.94711402	m
Area Correction Length	δL	3.220384974	m
Water Density	ρ	842.2184461	kg/m^3
Water Viscosity	μ	0.000120197	Pa.s
Volumetric Flow Rate Through Fracture	q_f	0.00118734	m^3/s
Linear Reynolds	Re	665.5722239	none
Overall Reynolds	Re_o	26482277.35	none
Radial Pressure drop at production	ΔP_{radp}	2486678.165	Pa
Linear Pressure Drop	ΔP_{lin}	723520.8145	Pa
Radial Pressure drop at injection	Δp_{radi}	1247895.091	Pa
Total Pressure Drop	ΔP	4458094.07	Pa
Total Pressure Drop in MPa	ΔP	4.45809407	MPa

Table XVII Reservoir data from SKG-2 to HDR-3 for run segment 7 of the Hijiori HDR project.

Fracture Model (Shallow Reservoir SKG-2 to HDR-3) Run Segment 7			
Parameter	Symbol	Value	Unit
Reservoir Depth	Z	1800	m
Distance between wells	D	55	m
Fracture Width	w	27.5	m
Angle of radial flow	θ	1.570796327	rad
Aperture	h	0.000185	m
Flow rate through fracture	m	1.6	kg/s
Reservoir temperature	T_R	230	C
Well radius at SKG-2	r_{wi}	0.10795	m
Well radius at HDR-3	r_{wp}	0.10795	m
Reservoir Vertical Length	H	200	m
Number of Fractures	n	2	none
External radius at SKG-2	r_{ei}	19.44543648	m
External radius at HDR-3	r_{ep}	19.44543648	m
Length of Linear Flow	L	16.10912703	m
Roughness	ε	0.000123333	m
Louis Friction Factor	f_l	2.687426267	none
Effective Permeability	k_e	1.06127×10^{-9}	m^2
Effective Permeability (in Darcy's)	k_e	1074.191956	Darcy's
Total reservoir permeability	k_{etotal}	4.98914×10^{-16}	m^2
Converging Skin Factor	S	1.26954475	none
Diverging Skin Factor	S	-1.26954475	none
Area of flow	A	2138.998013	m^2
Area Correction Radius (if no linear flow length)	A_{cr}	21.94182542	m
Area Correction Length	δL	3.542423472	m
Water Density	ρ	836.2170836	kg/m^3
Water Viscosity	μ	0.000118486	Pa.s
Volumetric Flow Rate Through Fracture	q_f	0.000956689	m^3/s
Linear Reynolds	Re	491.0420627	none
Overall Reynolds	Re_o	23234310.46	none
Radial Pressure drop at production	ΔP_{radp}	2375597.486	Pa
Linear Pressure Drop	ΔP_{lin}	726098.1452	Pa
Radial Pressure drop at injection	Δp_{radi}	1442342.55	Pa
Total Pressure Drop	ΔP	4544038.182	Pa
Total Pressure Drop in MPa	ΔP	4.544038182	MPa

Table XVIII Reservoir data from HDR-1 to HDR-2a for run segment 7 of the Hijiori HDR project.

Fracture Model (Deep Reservoir HDR-1 to HDR-2a) Run Segment 7			
Parameter	Symbol	Value	Unit
Reservoir Depth	Z	2200	m
Distance between wells	D	90	m
Fracture Width	w	45	m
Angle of radial flow	θ	1.570796327	rad
Aperture	h	0.00019	m
Flow rate through fracture	m	6	kg/s
Reservoir temperature	T_R	250	C
Well radius at HDR-1	r_{wi}	0.10795	m
Well radius at HDR-2a	r_{wp}	0.10795	m
Reservoir Vertical Length	H	200	m
Number of Fractures	n	4	none
External radius at HDR-1	r_{ei}	31.81980515	m
External radius at HDR-2a	r_{ep}	31.81980515	m
Length of Linear Flow	L	26.36038969	m
Roughness	ε	0.000126667	m
Louis Friction Factor	f_l	2.687426267	none
Effective Permeability	k_e	1.11941×10^{-9}	m^2
Effective Permeability (in Darcy's)	k_e	1133.04104	Darcy's
Total reservoir permeability	k_{etotal}	1.00118×10^{-15}	m^2
Converging Skin Factor	S	2.592024555	none
Diverging Skin Factor	S	-2.592024555	none
Area of flow	A	5727.564928	m^2
Area Correction Radius (if no linear flow length)	A_{cr}	35.90480524	m
Area Correction Length	δL	5.796692954	m
Water Density	ρ	821.379596	kg/m^3
Water Viscosity	μ	0.000111756	Pa.s
Volumetric Flow Rate Through Fracture	q_f	0.001826196	m^3/s
Linear Reynolds	Re	596.5401986	none
Overall Reynolds	Re_o	44972678.54	none
Radial Pressure drop at production	ΔP_{radp}	5056959.133	Pa
Linear Pressure Drop	ΔP_{lin}	1206775.655	Pa
Radial Pressure drop at injection	Δp_{radi}	1890144.77	Pa
Total Pressure Drop	ΔP	8153879.558	Pa
Total Pressure Drop in MPa	ΔP	8.153879558	MPa

Table XIX Reservoir data from HDR-1 to HDR-3 for run segment 7 of the Hijiori HDR project.

Fracture Model (Deep Reservoir HDR-1 to HDR-3) Run Segment 7			
Parameter	Symbol	Value	Unit
Reservoir Depth	Z	2200	m
Distance between wells	D	130	m
Fracture Width	w	65	m
Angle of radial flow	θ	1.570796327	rad
Aperture	h	0.0001565	m
Flow rate through fracture	m	2.4	kg/s
Reservoir temperature	T_R	250	C
Well radius at HDR-1	r_{wi}	0.10795	m
Well radius at HDR-3	r_{wp}	0.10795	m
Reservoir Vertical Length	H	200	m
Number of Fractures	n	3	none
External radius at HDR-1	r_{ei}	45.96194078	m
External radius at HDR-3	r_{ep}	45.96194078	m
Length of Linear Flow	L	38.07611845	m
Roughness	ε	0.000104333	m
Louis Friction Factor	f_l	2.687426267	none
Effective Permeability	k_e	7.5947×10^{-10}	m^2
Effective Permeability (in Darcy's)	k_e	768.7181279	Darcy's
Total reservoir permeability	k_{etotal}	3.97708×10^{-16}	m^2
Converging Skin Factor	S	1.138678664	none
Diverging Skin Factor	S	-1.138678664	none
Area of flow	A	11950.1046	m^2
Area Correction Radius (if no linear flow length)	A_{cr}	51.86249645	m
Area Correction Length	δL	8.373000933	m
Water Density	ρ	821.379596	kg/m^3
Water Viscosity	μ	0.000111756	Pa.s
Volumetric Flow Rate Through Fracture	q_f	0.000973971	m^3/s
Linear Reynolds	Re	220.2609964	none
Overall Reynolds	Re_o	29119689.62	none
Radial Pressure drop at production	ΔP_{radp}	4193287.823	Pa
Linear Pressure Drop	ΔP_{lin}	1151709.755	Pa
Radial Pressure drop at injection	Δp_{radi}	2865584.07	Pa
Total Pressure Drop	ΔP	8210581.649	Pa
Total Pressure Drop in MPa	ΔP	8.210581649	MPa

9.4 MODEL DETERMINED WELL PROFILE DATA

Term 1 – Run Segment 1

Table XX Well profile data for HDR-1 during run segment 1 determined by the model.

HDR-1 Term 1 (Run Segment 1)			
Depth (m)	Pressure (Pa)	Temp (°C)	Regime
0	8.0000×10^6	25	Single
30	8.2948×10^6	24.99093	Single
120	9.1793×10^6	25.00549	Single
210	1.0064×10^7	25.08542	Single
307	1.1018×10^7	25.25630	Single
519	1.3104×10^7	26.73091	Single
731	1.5191×10^7	28.99624	Single
943	1.7278×10^7	31.85681	Single
1155	1.9365×10^7	35.22090	Single
1367	2.1452×10^7	38.97841	Single
1440	2.2173×10^7	39.99115	Single
1513	2.2894×10^7	39.99115	Single
1640.6	2.4154×10^7	42.25583	Single
1768.2	2.5413×10^7	44.53102	Single
1895.8	2.6672×10^7	46.82483	Single
2023.4	2.7930×10^7	49.11532	Single
2151	2.9188×10^7	51.39161	Single
2200	2.9669×10^7	52.25811	Single

Table XXI Well profile data for HDR-2a and HDR-3 during run segment 1 determined by the model.

HDR-2a Term 1 (Run Segment 1)						HDR-3 Term 1 (Run Segment 1)					
Depth (m)	Pressure (Pa)	Temp (°C)	Regime	Quality		Depth (m)	Pressure (Pa)	Temp (°C)	Regime	Quality	
2200	1.69093×10^7	270	Single	0		2200	1.63555×10^7	270	Single	0	
2100	1.61414×10^7	269.94911	Single	0		2100	1.55883×10^7	269.72928	Single	0	
2000	1.53744×10^7	269.82354	Single	0		2000	1.48195×10^7	269.48536	Single	0	
1900	1.46081×10^7	269.57420	Single	0		1900	1.40534×10^7	268.94269	Single	0	
1800	1.38423×10^7	269.20396	Single	0		1800	1.32870×10^7	267.69291	Single	0	
1700	1.30769×10^7	268.95827	Single	0		1700	1.25193×10^7	266.10104	Single	0	
1600	1.23116×10^7	268.17479	Single	0		1600	1.17500×10^7	264.19386	Single	0	
1505	1.16229×10^7	267.59100	Single	0		1510	1.10557×10^7	262.21055	Single	0	
1400	1.07811×10^7	267.17576	Single	0		1400	1.02651×10^7	261.25722	Single	0	
1300	1.00163×10^7	266.74455	Single	0		1300	9.43127×10^6	260.25846	Single	0	
1200	9.25173×10^6	266.36319	Single	0		1200	8.65676×10^6	259.06478	Single	0	
1100	8.48749×10^6	265.81251	Single	0		1100	7.88127×10^6	257.77730	Single	0	
1000	7.72330×10^6	265.16257	Single	0		1000	7.10459×10^6	256.23693	Single	0	
900	6.95899×10^6	264.40233	Single	0		900	6.32632×10^6	254.41683	Single	0	
800	6.19435×10^6	263.47395	Single	0		800	5.54597×10^6	252.16007	Single	0	
700	5.42911×10^6	262.40167	Single	0		700	4.76291×10^6	249.54024	Single	0	
600	4.66304×10^6	261.19781	Bubble	0.004720		600	3.97663×10^6	246.59663	Single	0	
550	4.29147×10^6	260.30262	Bubble	0.017288		550	3.58215×10^6	244.82993	Bubble	0.002565	
510	4.04636×10^6	259.90924	Bubble	0.025509		509	3.26374×10^6	243.39935	Bubble	0.013006	
400	3.51401×10^6	258.37330	Bubble	0.043317		400	2.66517×10^6	241.85510	Bubble	0.037502	
300	3.16732×10^6	256.73208	1st Slug	0.053884		350	2.48935×10^6	241.00440	1st Slug	0.044209	
250	2.85666×10^6	255.78764	1st Slug	0.065478		300	2.17236×10^6	240.15594	1st Slug	0.058915	
200	2.55711×10^6	254.84397	1st Slug	0.077273		200	1.58351×10^6	238.16913	1st Slug	0.089058	
100	1.98446×10^6	252.75435	1st Slug	0.101670		100	1.03176×10^6	235.94714	2nd Slug	0.124177	
0	1.43751×10^6	250.57392	1st Slug	0.129368		0	8.21363×10^5	233.60293	2nd Slug	0.137674	

Table XXII Well profile data for HDR-1 and SKG-2 during run segment 5 determined by the model.

HDR-1 Term 2 (Run Segment 5)				SKG-2 Term 2 (Run Segment 5)			
Depth (m)	Pressure (Pa)	Temp (°C)	Regime	Depth (m)	Pressure (Pa)	Temp (°C)	Regime
0	2.00000×10^6	25.00	Single	0	3.00000×10^6	25	Single
30	2.29360×10^6	24.98	Single	30	3.29398×10^6	24.98	Single
120	3.17452×10^6	25.00	Single	120	4.17606×10^6	25	Single
210	4.05579×10^6	25.12	Single	210	5.05848×10^6	25.12	Single
307	5.00594×10^6	25.37	Single	310	6.03929×10^6	25.33	Single
519	7.08328×10^6	28.61	Single	410	7.02047×10^6	25.64	Single
731	9.16051×10^6	33.51	Single	510	8.00198×10^6	26.05	Single
943	1.12362×10^7	39.66	Single	610	8.98380×10^6	26.82	Single
1155	1.33090×10^7	46.65	Single	710	9.96582×10^6	27.71	Single
1367	1.53774×10^7	54.40	Single	810	1.09480×10^7	28.72	Single
1440	1.60882×10^7	55.40	Single	910	1.19303×10^7	29.83	Single
1513	1.67989×10^7	56.42	Single	1010	1.29126×10^7	31.04	Single
1640.6	1.80409×10^7	60.94	Single	1110	1.38949×10^7	32.34	Single
1768.2	1.92806×10^7	65.50	Single	1210	1.48773×10^7	33.71	Single
1895.8	2.05179×10^7	70.03	Single	1310	1.58595×10^7	35.15	Single
2023.4	2.17526×10^7	74.50	Single	1410	1.68417×10^7	36.64	Single
2151	2.29848×10^7	78.90	Single	1510	1.78237×10^7	38.18	Single
2200	2.34565×10^7	80.60	Single	1600	1.87073×10^7	41.57	Single
				1690	1.95901×10^7	45.07	Single
				1788	2.05502×10^7	48.86	Single
				1800	2.06675×10^7	49.32	Single

Table XXIII Well profile data for HDR-2a and HDR-3 during run segment 5 determined by the model.

HDR-2a Term 2 (Run Segment 5)					HDR-3 Term 2 (Run Segment 5)				
Depth (m)	Pressure (Pa)	Temp (°C)	Regime	Quality	Depth (m)	Pressure (Pa)	Temp (°C)	Regime	Quality
2200	1.76041×10^7	270	Single	0	2200	1.69278×10^7	270	Single	0
2100	1.68354×10^7	269.69350	Single	0	2100	1.61598×10^7	269.69804	Single	0
2000	1.60671×10^7	269.21346	Single	0	2000	1.53923×10^7	268.27713	Single	0
1900	1.52986×10^7	268.26933	Single	0	1900	1.46232×10^7	265.76244	Single	0
1800	1.52508×10^7	258.45267	Single	0	1800	1.50904×10^7	256.23503	Single	0
1700	1.44670×10^7	257.95390	Single	0	1700	1.43032×10^7	256.03329	Single	0
1600	1.36832×10^7	257.18892	Single	0	1600	1.35154×10^7	255.01083	Single	0
1500	1.28989×10^7	256.22558	Single	0	1510	1.27969×10^7	252.78440	Single	0
1400	1.21145×10^7	255.77428	Single	0	1400	1.19339×10^7	251.74747	Single	0
1300	1.13302×10^7	255.22368	Single	0	1300	1.11415×10^7	250.47638	Single	0
1200	1.05458×10^7	254.54431	Single	0	1200	1.03482×10^7	248.86571	Single	0
1100	9.76130×10^6	253.78402	Single	0	1100	9.44084×10^6	247.10882	Single	0
1000	8.96638×10^6	252.84799	Single	0	1000	8.64472×10^6	244.91738	Single	0
900	8.18082×10^6	251.70937	Single	0	900	7.84637×10^6	242.25242	Single	0
800	7.39422×10^6	250.28053	Single	0	800	7.04513×10^6	238.83671	Single	0
700	6.60619×10^6	248.60528	Single	0	700	6.23997×10^6	235.20769	Single	0
600	5.81638×10^6	246.68817	Single	0	600	5.42913×10^6	230.66074	Single	0
500	5.02433×10^6	244.84140	Single	0	500	4.69318×10^6	225.14032	Single	0
400	4.23088×10^6	243.62667	Single	0	400	3.78587×10^6	222.68437	Single	0
300	3.43681×10^6	242.53288	Bubble	0.002768	300	2.95802×10^6	219.96125	Single	0
290	3.36038×10^6	242.40526	Bubble	0.005889	200	2.12759×10^6	216.74975	Bubble	0.002981
200	2.85890×10^6	241.25639	Bubble	0.026378	150	1.71048×10^6	210.02580	Bubble	0.012803
160	2.67452×10^6	240.68640	1st Slug	0.033970	100	1.40223×10^6	208.02620	Bubble	0.029754
100	2.30270×10^6	239.83115	1st Slug	0.050999	80	1.33655×10^6	207.22880	Bubble	0.032859
0	1.72822×10^6	238.32900	1st Slug	0.080247	60	1.27957×10^6	206.37000	Bubble	0.035296
					32.5	1.21186×10^6	205.193	1st Slug	0.038006
					0	1.00167×10^6	204.1404	1st Slug	0.053667

Table XXIV Well profile data for HDR-1 and SKG-2 during run segment 7 determined by the model.

HDR-1 Term 2 (Run Segment 5)				SKG-2 Term 2 (Run Segment 7)			
Depth (m)	Pressure (Pa)	Temp (°C)	Regime	Depth (m)	Pressure (Pa)	Temp (°C)	Regime
0	4.00000×10^6	35	Single	0	1.00000×10^6	35	Single
30	4.29320×10^6	34.97562	Single	30	1.29275×10^6	34.94504	Single
120	5.17294×10^6	34.95407	Single	120	2.17114×10^6	34.90036	Single
210	6.05302×10^6	35.03006	Single	210	3.04988×10^6	35.05939	Single
307	7.00189×10^6	35.23823	Single	310	4.02659×10^6	35.38307	Single
519	9.07641×10^6	37.20029	Single	410	5.00360×10^6	35.91536	Single
731	1.11513×10^7	40.36379	Single	510	6.98085×10^6	36.64211	Single
943	1.32256×10^7	44.41484	Single	610	7.95868×10^6	38.03866	Single
1155	1.52983×10^7	49.20273	Single	710	8.93643×10^6	39.68289	Single
1367	1.73685×10^7	54.55021	Single	810	9.91398×10^6	41.55238	Single
1440	1.80814×10^7	55.22823	Single	910	1.08912×10^7	43.6235	Single
1513	1.87943×10^7	55.92244	Single	1010	1.18680×10^7	45.87451	Single
1640.6	2.00403×10^7	59.07550	Single	1110	1.28444×10^7	48.284	Single
1768.2	2.12850×10^7	62.17538	Single	1210	1.38200×10^7	50.82928	Single
1895.8	2.25284×10^7	65.38864	Single	1310	1.47950×10^7	53.49111	Single
2023.4	2.37703×10^7	68.58055	Single	1410	1.57691×10^7	56.24591	Single
2151	2.50106×10^7	71.73477	Single	1510	1.67424×10^7	59.07505	Single
2200	2.54855×10^7	72.96645	Single	1600	1.76174×10^7	65.43398	Single
				1690	1.84899×10^7	71.91622	Single
				1788	1.94367×10^7	78.79678	Single
				1800	1.95522×10^7	79.61078	Single

Table XXV Well profile data for HDR-2a and HDR-3 during run segment 7 determined by the model.

HDR-2a Term 2 (Run Segment 7)					HDR-3 Term 2 (Run Segment 7)				
Depth (m)	Pressure (Pa)	Temp (°C)	Regime	Quality	Depth (m)	Pressure (Pa)	Temp (°C)	Regime	Quality
2200	1.73316×10^7	250	Single	0	2200	1.72749×10^7	250	Single	0
2100	1.65336×10^7	251.85109	Single	0	2100	1.65336×10^7	252.13311	Single	0
2000	1.57390×10^7	253.51500	Single	0	2000	1.57395×10^7	253.57085	Single	0
1900	1.49475×10^7	253.65855	Single	0	1900	1.49482×10^7	254.26933	Single	0
1800	1.46256×10^7	241.86168	Single	0	1800	1.46370×10^7	248.42315	Single	0
1700	1.38187×10^7	242.26484	Single	0	1700	1.38395×10^7	248.51197	Single	0
1600	1.30127×10^7	242.31419	Single	0	1600	1.30429×10^7	248.31419	Single	0
1510	1.22961×10^7	241.72835	Single	0	1510	1.23265×10^7	247.89262	Single	0
1400	1.14202×10^7	241.33583	Single	0	1400	1.14510×10^7	247.53995	Single	0
1300	1.06242×10^7	240.84559	Single	0	1300	1.06555×10^7	247.10344	Single	0
1200	9.82843×10^6	240.28407	Single	0	1200	9.86024×10^6	246.50305	Single	0
1100	9.03263×10^6	239.44153	Single	0	1100	9.06490×10^6	245.81711	Single	0
1000	8.23644×10^6	238.52251	Single	0	1000	8.26940×10^6	244.92255	Single	0
900	7.43977×10^6	236.31647	Single	0	900	7.47345×10^6	243.79852	Single	0
800	6.64524×10^6	235.86796	Single	0	800	6.67670×10^6	242.32395	Single	0
700	5.84640×10^6	235.20039	Single	0	700	5.87866×10^6	240.55518	Single	0
600	5.04601×10^6	234.15284	Single	0	600	5.07892×10^6	238.52212	Single	0
509	4.31574×10^6	233.94726	Single	0	509	4.34926×10^6	236.25070	Single	0
400	3.43844×10^6	233.08426	Single	0	400	3.47258×10^6	233.55254	Single	0
300	2.63324×10^6	232.12621	Bubble	0.01383	300	2.66539×10^6	230.58815	Bubble	0.00822
250	2.39811×10^6	231.56126	1st Slug	0.02475	250	2.30100×10^6	228.85803	Bubble	0.02320
200	2.07746×10^6	230.99650	1st Slug	0.04115	200	2.03359×10^6	226.91818	Bubble	0.03356
150	1.77981×10^6	230.36151	1st Slug	0.05739	150	1.83499×10^6	224.98792	Bubble	0.04080
100	1.49622×10^6	229.72549	1st Slug	0.07435	100	1.68100×10^6	222.81658	Bubble	0.04534
50	1.22071×10^6	229.00763	1st Slug	0.09262	50	1.55386×10^6	220.58149	1st Slug	0.04849
32.5	1.18428×10^6	228.73809	2nd Slug	0.09482	32.5	1.44222×10^6	219.77592	1st Slug	0.05438
0	1.11729×10^6	228.23758	2nd Slug	0.09899	0	1.23974×10^6	218.28125	1st Slug	0.06598

9.5 SAMPLE CALCULATION

Fracture Flow

The following sample calculation is taken from run segment 1 of the Hijori analysis for fracture flow between HDR-1 and HDR-2 and well flow in HDR-2a. It should be noted that the answers given were determined by technology and thus all significant figures were account for, whilst the equations shown only show limited significant figures.

In run segment SKG-2 was shut in and therefore only HDR-1 was used for injection. It is assumed then that reservoir flow occurred only in the deep fracture zone at 2200m. Figure 48 shows the assumed dimensions of the flow area in the fracture. It is known that the distance between the wellbores at HDR-1 and HDR-2a is 90m so the width is assumed to be 45m and the angle of radial flow is assumed to be $\pi/2$ radians. Four horizontal fractures allow communication between the wellbores and they are assumed to be identical with an aperture of 0.17mm and relative roughness of 2/3. The injection mass flow rate from HDR-1 is 18.35kg/s is assumed to divide evenly to 9.175kg/s towards both the HDR-2a and HDR-3 sides. The production mass flow rate from HDR-2a is 5kg/s and thus the mass flow between the wellbores is assumed to be 7kg/s as an approximate average which accounts for water loss to the formation. The radius of both wellbores is known to be 0.10795m.

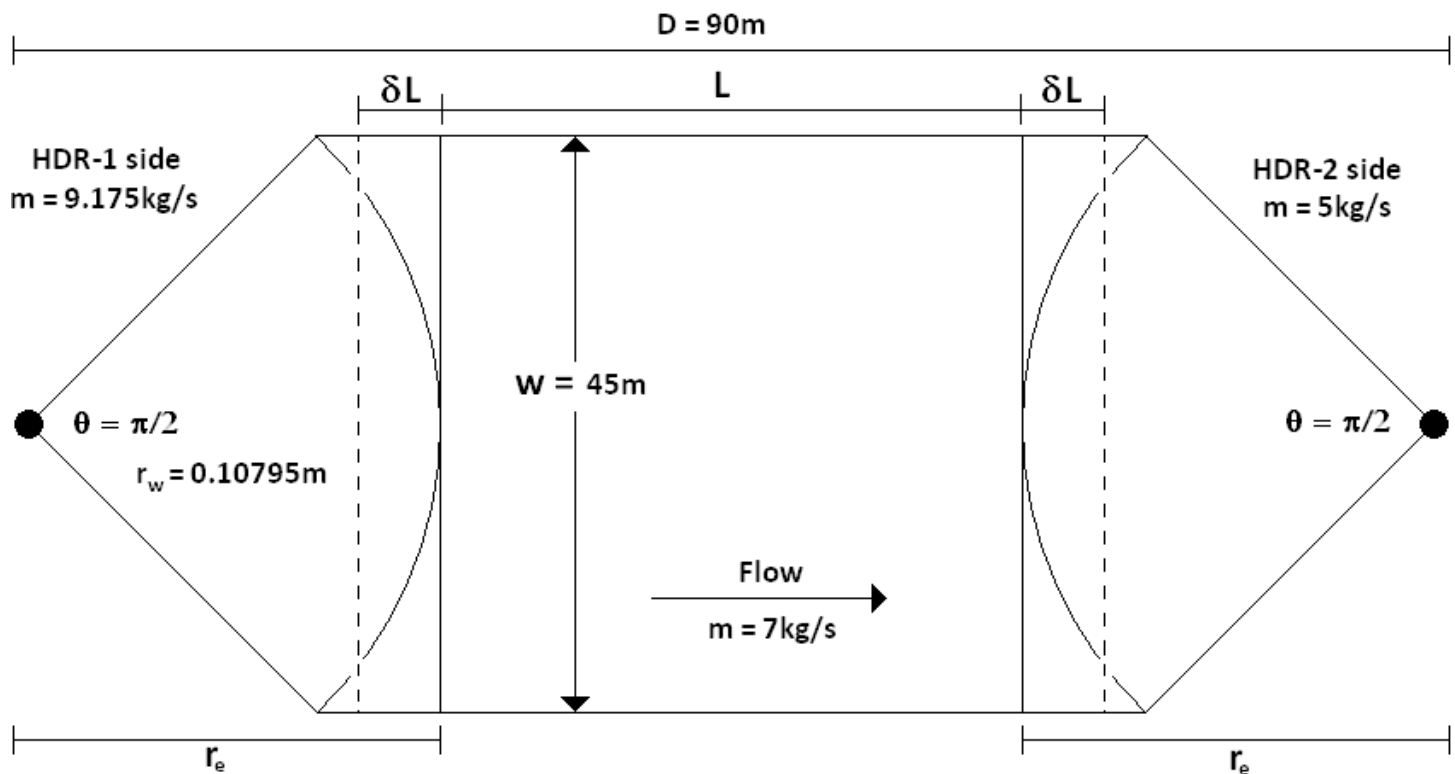


Figure 48 Assumed fracture dimensions.

First, the unknown dimensions need to be determined by geometrical methods. The external radius can be determined using simple trigonometry

$$r_e = \frac{w}{2 \sin\left(\frac{\theta}{2}\right)} = \frac{45}{2 \sin\left(\frac{\pi}{4}\right)} = 31.82m$$

The linear flow length is then

$$L = D - 2r_e = 90 - 2 \times 31.82 = 26.36m$$

The correction length can be determined by equating the area of undefined flow with the extra linear flow area

undefined flow area = extra linear flow area

$$\left(wD - w\sqrt{r_e^2 - w^2}\right) - \left(\frac{1}{2}\pi r_e^2 + wL\right) = w\delta L$$

Rearranging and solving for δL

$$\delta L = 5.80m$$

Second, the viscosity and density of water are determined. It is assumed that water is at reservoir temperature and given flow pressure at the HDR-1 wellbore is approximately 30MPa the water is still in liquid phase. Therefore using steam tables to determine density and viscosity

$$\rho = 797.61kg/m^3$$

$$\mu = 1.04 \times 10^{-4} Pa \cdot s$$

Third, the Reynolds number criterion needs to be satisfied in order for the model to assume laminar flow. Thus for linear flow using equation 4

$$Re_{lin} = \frac{2h\rho u_{lin}}{\mu}$$

But $u_{lin} = q/A = m/n\rho wh$

$$Re_{lin} = \frac{2m}{\mu nw} = \frac{2 \times 7}{1.04 \times 10^{-4} \times 4 \times 45} = 746 \leq 2300 \therefore \text{laminar}$$

And the overall Reynolds number for radial flow using equation 7

$$Re_o = \frac{q\rho}{\theta h\mu} = \frac{m}{\theta n h\mu} = \frac{7}{0.5\pi \times 4 \times 0.00017 \times 1.04 \times 10^{-4}} = 6.3 \times 10^7 \leq 1.0 \times 10^8 \therefore \text{laminar}$$

Therefore laminar flow can be assumed. Fourth, the Louis friction factor is determined by equation 2

$$f_l = 1 + 3.1 \left(\frac{\varepsilon}{h}\right)^{1.5} = 1 + 3.1 \times \left(\frac{2}{3}\right)^{1.5} = 2.69$$

Fifth, effective permeability and skin factors can be calculated using equations x and x

$$k_e = \frac{h^2}{12f_l} = \frac{(0.00017)^2}{12 \times 2.69} = 8.96 \times 10^{-10} m^2$$

And the divergent skin factor is

$$S = -\frac{q\rho h}{20f_l\mu\theta} \left[\frac{1}{r_w^2} - \frac{1}{r_e^2} \right]$$

$$S_d = -\frac{mh}{20n f_l \mu \theta} \left[\frac{1}{r_w^2} - \frac{1}{r_e^2} \right] = -\frac{7 \times 0.00017}{20 \times 4 \times 2.69 \times 1.04 \times 10^{-4} \times 0.5\pi} \left[\frac{1}{(0.10795)^2} - \frac{1}{(31.82)^2} \right] = -2.90$$

Due to symmetry the convergent skin factor is of the same magnitude but of positive sign, that is, $S_c = 2.90$. Sixth, the pressure drop across the fracture zone can be estimated by summing equations 3, 5 and 6

$$\Delta P_{total} = \Delta P_{rad,i} + \Delta P_{lin} + \Delta P_{rad,p}$$

$$\Delta P_{total} = \frac{\mu q [\ln(r_e/r_w) + S_d]}{k_e \theta h} + \frac{q\mu(L + 2\delta L)}{k_e h w} + \frac{\mu q [\ln(r_e/r_w) + S_c]}{k_e \theta h} = 1.28 \times 10^7 Pa$$

Therefore the total pressure drop from the wellbore at HDR-1 to the wellbore at HDR-2a is approximately 13MPa. The pressure at the HDR-2a wellbore is therefore

$$P_{pw} = P_{iw} - \Delta P_{total} = 2.97 \times 10^7 - 1.28 \times 10^7$$

$$P_{pw} = 1.69 \times 10^7$$

The total reservoir permeability can be back-calculated using equation 13 but in this case $L = D$ and $H = 200m$.

$$k_{etotal} = \frac{qD\mu}{\Delta P_w H}$$

$$k_{etotal} = \frac{mD\mu}{n\rho\Delta P_w H} = \frac{7 \times 90 \times 1.04 \times 10^{-4}}{4 \times 797.61 \times 1.28 \times 10^7 \times 45 \times 200} = 7.17 \times 10^{-16} m^2$$

Well Flow

This sample calculation uses the analysis of HDR-2a from run segment 1 as an example of how the model is able to predict pressure and temperature loss across an increment of a well. The flow of hot water is up and the increment is from 600m to 550m deep. From the casing profile (figure 44) it can be seen that casing inner radius is 0.10795m, the casing outer radius is 0.1222375m and the cement/formation radius is 0.155575m. From the temperature gradient (figure 13), the temperature of the formation at 600m is 140°C. The flow rate is 5kg/s and an average flow time of 65 days is assumed.

The pressure of the flow at 600m is

$$P_1 = 4663039.9Pa$$

And the temperature of the flow at 600m is

$$T_1 = 261.2^\circ C$$

The relative enthalpies at these conditions are

$$h = 1140.8kJ/kg, h_L = 1132.9kJ/kg \text{ and } h_G = 2796.9kJ/kg$$

It can be seen that $h > h_L$ so therefore the flow regime is not single and is two-phase. The steam quality is determined by equation 29

$$x = \frac{h_m - h_L}{h_G - h_L} = \frac{1140.8 - 1139.9}{2796.9 - 1139.9} = 0.00472$$

At flow conditions we have $\omega = 0.0234N/m$ from equation 34, $\rho_L = 809.2kg/m^3$ and $\rho_G = 23.12kg/m^3$ which can then be used to determine volumetric flow rates and velocities of each phase

$$q_G = \frac{mx}{\rho_G} = \frac{5 \times 0.00472}{23.12} = 0.00102m^3/s$$

$$v_{SG} = \frac{0.00102}{(0.10795)^2\pi} = 0.028m/s$$

$$q_L = \frac{m(1-x)}{\rho_L} = \frac{5 \times (1 - 0.00472)}{809.2} = 0.00615m^3/s$$

$$v_{SL} = 0.168m/s$$

$$v_{ST} = 0.196m/s$$

The flow detection parameters can now be determined using equations 22, 23,24, 32 and 33

$$L_{b/s} = 1.071 - 0.2218 \frac{v_{ST}^2}{d_w}$$

$$L_{b/s} = 1.071 - 0.2218 \times \frac{(0.196)^2}{2 \times 0.10795} = 1.032$$

$$N_{GV} = v_{SG} \left(\frac{\rho_L}{g\omega} \right)^{0.25} = 0.215$$

$$N_{LV} = v_{SL} \left(\frac{\rho_L}{g\omega} \right)^{0.25} = 1.294$$

$$L_{s/t} = 50 + 36N_{LV} = 96.596$$

$$L_{t/m} = 75 + 84(N_{LV})^{0.75} = 176.932$$

Checking for flow regime criteria: bubble

$$L_{b/s} > v_{SG}/v_{ST}$$

$$L_{b/s} = 1.032 \text{ and } \frac{v_{SG}}{v_{ST}} = \frac{0.028}{0.196} = 0.143$$

Therefore it can be seen that $L_{b/s} > v_{SG}/v_{ST}$ returns a value of true and bubble flow is the flow regime for the increment. Now following the procedure outline in the model description for determining mixture density and friction gradient for bubble flow

$$\eta_G = 0.5 \left[\left(1 + \frac{v_{ST}}{v_{slip}} \right) - \left\{ \left(1 + \frac{v_{ST}}{v_{slip}} \right)^2 - 4 \frac{v_{SG}}{v_{slip}} \right\}^{1/2} \right]$$

$$\eta_G = 0.5 \left[\left(1 + \frac{0.196}{0.2439} \right) - \left\{ \left(1 + \frac{0.196}{0.2439} \right)^2 - 4 \times \frac{0.028}{0.2439} \right\}^{1/2} \right] = 0.066$$

Therefore mixture density

$$\rho_m = \rho_L(1 - \eta_G) + \rho_G\eta_G = 809.2 \times (1 - 0.066) + 23.12 \times 0.066 = 757.4 \text{ kg/m}^3$$

And friction gradient

$$\tau_f = \frac{f \rho_m v_{ST}^2}{2d_w} = \frac{0.0163 \times 757.4 \times (0.196)^2}{2 \times 2 \times 0.10795} = 1.099 Pa/m$$

The acceleration gradient is calculated by equation 16

$$\gamma_a = \frac{mq_G}{A^2 P} = \frac{5 \times 0.028}{(\pi(0.10795)^2)^2 \times 4663039.9} = 8.17 \times 10^{-7}$$

Pressure drop can then be determined by equation 15

$$\Delta P = \left(\frac{\rho_m g + \tau_f}{1 - \gamma_a} \right) \Delta Z = \frac{757.4 \times 9.81 + 1.099}{1 - 8.17 \times 10^{-7}} \times (600 - 550) = 371574.3 Pa$$

The pressure at 550m is therefore

$$P_2 = 4663039.9 - 371574.3 = 4291465.6 Pa$$

Now for the heat transfer calculations. First, determine the transient heat conduction function of 65 days of flow and an earth diffusivity of

$$\alpha = 1.42 \times 10^{-6} m^2/s$$

$$f(t) = \ln \frac{2\sqrt{\alpha t}}{r_h} - 0.29 = \ln \frac{2\sqrt{1.42 \times 10^{-6} \times 65 \times 24 \times 3600}}{0.155575} - 0.29 = 3.303$$

Second, using equation 60, the overall heat transfer coefficient can be calculated

$$U_{ci} = \left(\frac{r_{ci} \ln \left(\frac{r_{co}}{r_{ci}} \right)}{\lambda_{cas}} + \frac{r_{ci} \ln \left(\frac{r_h}{r_{co}} \right)}{\lambda_{cem}} \right)^{-1} = \left(\frac{0.10795 \ln \left(\frac{0.1222375}{0.10795} \right)}{44} + \frac{0.10795 \ln \left(\frac{0.155575}{0.1222375} \right)}{0.29} \right)^{-1} = 11.101 W/m^2 K$$

Third, using equation 61 with $\lambda_e = 3.8 W/mK$, the cement formation interface temperature is determined

$$T_h = \frac{f(t)r_{ci}U_{ci}T + \lambda_e T_e}{f(t)r_{ci}U_{ci} + \lambda k_e} = \frac{3.303 \times 0.10795 \times 11.101 \times 261.2 + 3.8 \times 140}{3.303 \times 0.10795 \times 11.101 + 3.8} = 201.84^\circ C$$

Fourth, equation 62 is used to calculate heat flow between the well and the formation per metre flow.

$$\dot{Q} = 2\pi r_{ci} U_{ci} (T - T_h) = 2\pi \times 0.10795 \times 11.101 \times (261.2 - 201.84) = 446.96 W/m$$

Fifth, with the specific heat capacity of water equal to 4992.9J/kg.K, temperature at the end of the increment can be estimated

$$T_2 = T_1 - \frac{Q\Delta Z}{mc_p} = 261.2 - \frac{446.96 \times 50}{5 \times 4992.9} = 260.3^\circ\text{C}$$

Therefore the temperature and pressure at the end of the increment are

$$T_2 = 260.3^\circ\text{C} \text{ and } P_2 = 4291465.6\text{Pa}$$

The above process can be repeated until wellhead pressure and temperature are obtained.